Development And Characterization Of A Small Scale Methanol Synthesis Reactor Based On Natural Convection

Daniel van Laake

Technische Universiteit Delft

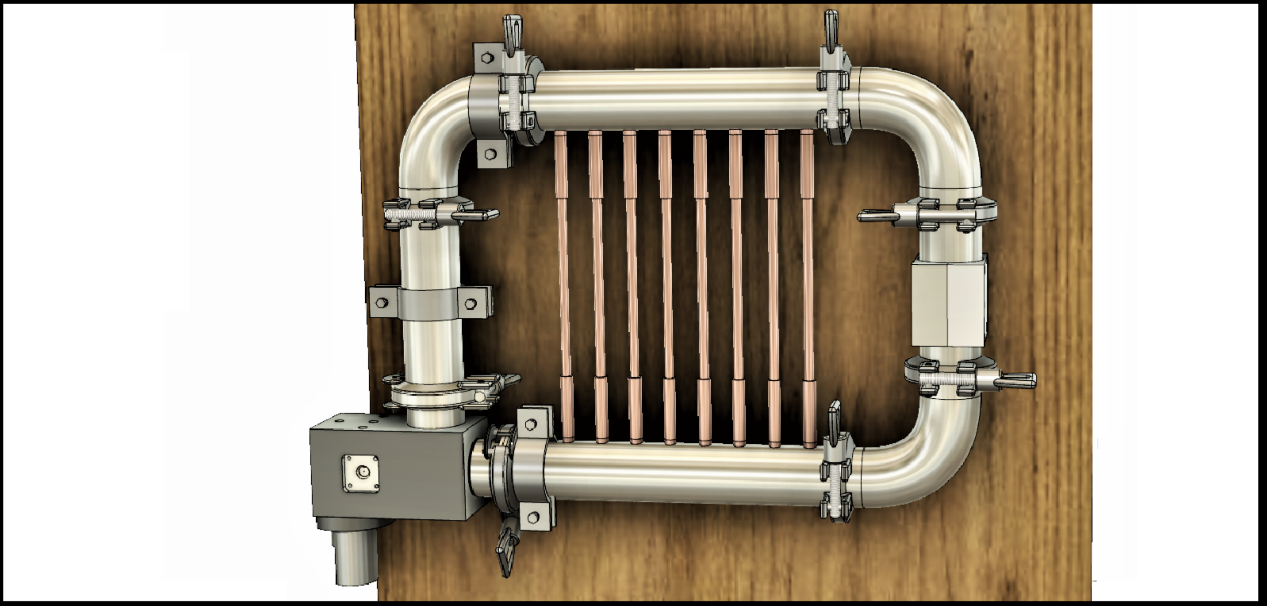

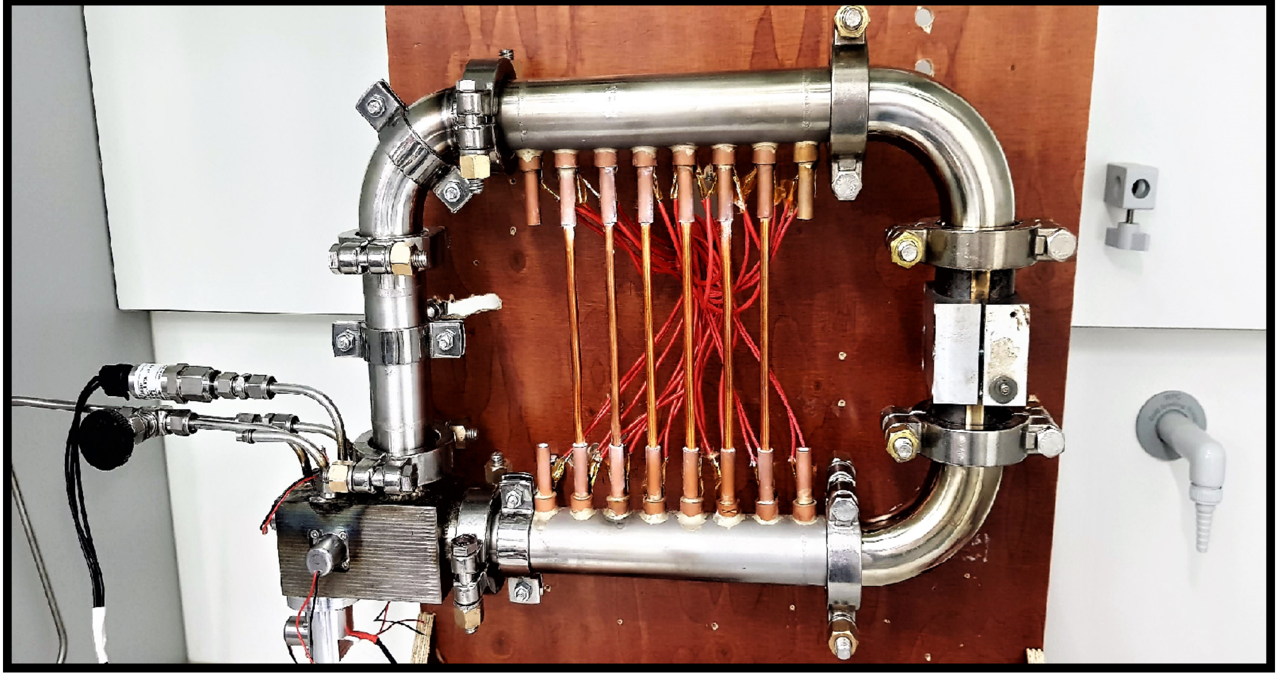

TU Delft Delft University of Technology

Z E F

Challenge the future

Development and characterization of a small scale methanol synthesis reactor based on natural convection

by

Daniel van Laake

in partial fulfillment of the requirements for the degree of

Master of Science
in Mechanical Engineering,
Energy & Process Technology

at Delft University of Technology,
to be defended publicly on Wednesday April 3, 2019 at 13:30 PM.

Student number:	4297334	
Project duration:	July 2018 – March 2019	
Daily supervisor:	Ir. J. Van Kranendonk,	ZEF B.V.
Thesis Comittee:	Prof. dr. ir. W. De Jong,	TU Delft (Chair)
	Prof. dr. ir. E. Goetheer,	TU Delft
	Dr. H. B. Eral	TU Delft

This thesis is confidential and may not be made public until December 31, 2021

Abstract

Increasing renewable electricity production calls for innovative methods to store electricity as well as a desire for electrification of processes that currently rely on fossil fuels. Zero Emission Fuels is a company that is developing a system to convert carbon dioxide and water from the air into methanol, a liquid hydrocarbon fuel, using photovoltaic energy. The scale of the system is fit for a single solar PV panel. The desired methanol output is 25 grams per hour.

In this work, a new design for the methanol synthesis reactor of the system is developed, built and experimentally characterized. Knowledge from work by Basarkar and Gutierrez on a previous prototype is used as the starting point. The focus of the new design is placed on the heat integration network, the natural circulation effects, and tilting of the reactor. The heat exchanger makes use of heat pipes to transfer heat. Natural circulation is increased by increasing the channel dimensions of the system. This led to an increase in mass flow rate of over 3000%, making the mass flow rate the limiting factor for reactor performance. The mass flow rate is roughly 800% higher than assumed in the design phase; the resulting energy flows are too high for the heat exchanger to work effectively. Nevertheless, the heat exchanger heating duty relative to total heating is 230% higher than Basarkar. Tilting the reactor 20^o reduced the mass flow rate by 46% to 0.41 g/s, improving almost all aspects of reactor performance. Productivity increased by 58% to 15.7 g/h; 182% higher than Basarkar, though the space time yield is lower (4.1 vs 6.8 mmol/gcat/h). The energy efficiency of the system is close to Basarkar at 36.5% (vs. 37.5%). It is clear from experimental correlations that reducing mass flow rate will increase productivity, energy efficiency and heat exchanger performance.

By simulating the requirements for an autothermal reactor it is found that the catalyst bed dimensions should be increased in terms of diameter and length to increase to residence time in the catalyst bed. The results agree with the experimental conclusion that the mass flow rate should be reduced. Furthermore, it is recommended to heat the fluid by convection instead of conduction to ensure a more homogeneous temperature profile in the catalyst bed. Also, the heat exchanger should be expanded by adding more heat pipes and increasing the heat transfer surface area.

Acknowledgements

There are many people who helped this project come in to fruition to whom I am grateful. I feel incredibly lucky to be have been able to conclude my studies at ZEF. It provided me with a stimulating, academic atmosphere, as well as many useful facilities, of which the knowledge and guidance of Ulrich, Hessel, and Jan were no doubt the most invaluable. I do not think that a project of this magnitude would have been possible without them.

In particular, I would like to thank Jan for his endless energy, knowledge, and enthusiasm for doing science. He has brought out the best in me in a way that was unimaginable to me at the start of this journey.

I also had the good fortune of having Earl and Wiebren as my supervisors. Earl actually took initiative to plan many of our meetings, his contagious enthusiasm always gave me energy when the going was tough. My meetings with Wiebren often left me with new directions to follow, and always added more scientific depth.

A special thanks to Alain and the people at the faculty of Mechanical Engineering who helped me build the reactor.

Of course, I am the most grateful to my parents Anneke and Patrick for making my life so comfortable and facilitating my progress as an academic and as a person. I always felt that my studies were a personal path, and by no means pressured. I think this is or will be reflected in the way I live my life.

Contents

1 Introduction **3**
- 1.1 Renewable energy advancements 4
- 1.2 Zero Emission Fuels 6
- 1.3 Power to Methanol 7
- 1.4 Research focus 8
- 1.5 Research questions 8
- 1.6 Report structure 9

2 Background **11**
- 2.1 A brief history of methanol synthesis 11
- 2.2 Reaction kinetics 12
- 2.3 Methanol synthesis catalyst 13
- 2.4 Methanol synthesis processes with CO_2 as feedstock 15
- 2.5 Development of the ZEF methanol reactor 15
  - 2.5.1 Brilman reactor 16
  - 2.5.2 First ZEF prototype: MBR 17
  - 2.5.3 Further reactor design at ZEF 18
- 2.6 Reactor design parameters 19
  - 2.6.1 Catalyst bed sizing 19
  - 2.6.2 Heat pipe technology 19
  - 2.6.3 Methanol Corrosion 25

3 Reactor development **27**
- 3.1 General reactor design 27
- 3.2 Heat pipe validation and design 29
  - 3.2.1 Heat pipe limitations 29
  - 3.2.2 Heat pipe experimental validation 30
- 3.3 Heat pipe support and fin design 32
  - 3.3.1 Heat transfer surface area 32
  - 3.3.2 Fin structure design 34
  - 3.3.3 Capillary blockage in the fins 36
- 3.4 Level sensor design 38
- 3.5 Design summary 38
- 3.6 Experimental setup description 39
  - 3.6.1 Sensors 39
  - 3.6.2 Reactor section 40
  - 3.6.3 Electronics 41
  - 3.6.4 Gaskets 41
  - 3.6.5 Gas bottles 42
  - 3.6.6 Experiment operational procedure 42
- 3.7 Experimental data analysis methods 43
  - 3.7.1 Reaction heat 43
  - 3.7.2 Mass flow rate and heat flows 43
  - 3.7.3 Energy efficiency 44
  - 3.7.4 Variable reactor conditions 44

4 Experimental reactor design validation 45
4.1 Comparing reactor orientations 45
4.1.1 Base case 46
4.1.2 Tilting of the reactor 46
4.1.3 Pressure drop with Ergun's equation 48
4.2 Mass balances 48
4.2.1 Total mass balance and carbon conversion 48
4.2.2 Conversion per pass 49
4.3 Energy balance 50
4.3.1 Insulation losses by convection 50
4.3.2 Comparison to mass flow rate based calculations 50
4.3.3 Total energy balance and discussion 51
4.4 Heat exchanger performance 52
4.4.1 Relative heat transfer evaluation 53
4.4.2 Heat exchanger heating and cooling 54
4.4.3 Heat pipe temperatures and performance 54
4.4.4 Heat exchanger performance discussion 56
4.5 Reactor flow homogeneity 56
4.5.1 Modelling of the equivalent reacting flow 57
4.5.2 Center temperature and simulation results 58
4.6 Performance comparison with previous work 59

5 Design of an optimal reactor 61
5.1 Autothermal calculations based on an industrial space time yield 61
5.2 Reaction kinetics and catalyst bed length simulation 62
5.3 Idealized autothermal reactor design 63
5.3.1 Assumptions and boundary conditions 63
5.3.2 Autothermal operation point 63
5.3.3 Discussion 64

6 Conclusions & Recommendations 67
6.1 Conclusions 67
6.2 Recommendations 69

A Heat pipe limitation constants 73

B Reactor parts and sizing 75
B.1 Main reactor parts 75
B.2 Heat pipe support with fins 76
B.3 Cornerpiece 77

C NTC Calibration 79

D Heat pipe heat transfer correlation 81

E Mass flow rate determination comparison 83
E.1 HEX heat transfer determination method comparison 84

F Additional experimental results 85
F.1 Convective fluid heating 85
F.2 Active condenser cooling 85
F.3 Heater temperature increase 86

G Previous work extra calculations 87

List of Figures

1.1 Global land-ocean mean temperature index of the period 1880-2016. The 0-line is the mean temperature of said period. Data from [1]. 3
1.2 Atmospheric CO2 concentrations of (a) the last 40 years in Mauna Loa, Hawaii [2], and of (b) the last two millennia, determined with ice-core samples [3]. 4
1.3 Global temperature anomaly in comparison to the present (top) and atmospheric CO_2 concentration (bottom) of the past 800,000 years, determined by Luthi *et al.* using Antarctic ice core samples. The left of the "Age" axis is the present age. The dashed lines represent the mean values over time frames of two glacial cycles. Figure taken from [4]. 4
1.4 Development of solar PV costs versus the total installed capacity globally for the period 1976-2016 (a), and 2006-2016 (b). Every point on the graph represents one year. Data from [7]. 5
1.5 World energy consumption by fuel in 2015 [5]. 6
1.6 Simplified block scheme of the ZEF system. All the subsystems are powered by a solar panel, and should be able to operate fully off the grid. 7

2.1 Transmission Electron Microscope image of a conventional $Cu/ZnO/Al_2O_3$ catalyst, from [26]. 13
2.2 Schematic of the Brilman methanol synthesis reactor with in-situ condensation, figure from [13]. 16
2.3 Schematic of the Modified Brilman Reactor, figure from [13]. 17
2.4 3D drawing of the first ZEF reactor concept with heat pipes, along with a schematic view showing the dimensions in millimeters. 18
2.5 The working principle of a heat pipe [40]. 20
2.6 Heat pipe heat exchanger concept. Figure from [41]. 22
2.7 Design limitations for a heat pipe, relative to the axial heat flux and temperature of the heat pipe. The heat pipe can only operate under the curves. For example, when working close to the maximum temperature of a heat pipe, the axial flux cannot be high due to the boiling limit. 22

3.1 3D model of the new reactor design, and a schematic with the dimensions. The catalyst bed is highlighted in orange. More dimensions are shown in Appendix B. . . 28
3.2 Capillary heat transfer limitation 30
3.3 Heat pipe test setup. Top left (with plate heater) is the setup itself. Bottom left is the test in horizontal operation, right is the test in vertical operation. 30
3.4 Evaporator and condenser temperature of 300mm heat pipes in three different orientations. The angle Ψ is against the horizontal, where positive means evaporator above condenser. Heat input is constant at 9.5W. Irregularities in the curves caused by adjusting insulation which was coming loose. 31
3.5 Evaporator and condenser temperature of 200mm heat pipes in two different orientations. The angle Ψ is against the horizontal, where positive means evaporator above condenser. Heat input is constant at 9.5W. Irregularities in the curves caused by adjusting insulation which was coming loose. 31
3.6 Capillary limit heat transfer for three different values of porosity. The values are based on calculations with values from table A.1. 31

3.7 Heat transfer required per heat pipe against the amount of heat pipes. 33
3.8 Fin area required per heat pipe against the amount of heat pipes. 34
3.9 Copper fin and conical support design. See figure B.2 in the Appendix for the sizing. 35
3.10 Photograph of the four conical support preparations. From top to bottom: Smooth, Sandblasted, Grooved, Grooved and Sandblasted. 35
3.11 Heat profile of the fins and four different supports after 5 minutes of 15 W heating from the inside. 36
3.12 Droplets attached to fins due to capillary forces. (a) and (b) are tested in a methanol/water mixture (0.8/0.2, room temperature), with a fin spacing of 3 mm and 5 mm, respectively. (c) has a fin spacing of 5 mm and is tested in pure water at room temperature. 37
3.13 Thermal stress simulation of materials for the level sensor pill, executed in Fusion 360. The pills are designed for a total density of 750 kg/m^3, a height of 18 mm and a diameter of 7.75 mm. The coloration represents the safety factor (SF), a scale based on a stress analysis. A value lower than three indicates possible material failure. . . 38
3.14 Schematic of the positions of all the sensors in the reactor. 39
3.15 Schematic of the reactor with the location of the fluid sensors shaded in red. Note the absence of heat pipes. How they are named is given as these sensors will be referenced often in the results. 40

4.1 Schematic representation of the three tilt orientations. 46
4.2 Correlations between the mass flow rate and the STY (a), energy efficiency (b), heater duty (c) and reactor outlet temperature (d) for multiple experiments. 47
4.3 Mass balance diagram for the 20^o tilt reactor orientation. 49
4.4 Energy balance diagram for the 20^o tilt reactor orientation. 52
4.5 Mass flow rate and heat (HEX heating) flow per unit of mass correlated for several experiments. 54
4.6 Heat pipe performance displayed by the temperature difference per heat pipe and the top temperature per heat pipe for each individual heat pipe for the three reactor orientations. 55
4.7 Temperature difference per heat pipe with its position in the system for the three different reactor orientations. 55
4.8 Flow chart of the COCO model used for the simulations. Note the splitter at the right side of the model before the reactor. 57
4.9 Diagram representing a non-homogeneous temperature profile in a flow (left), and the method of splitting this profile into a equivalent reacting flow and a non-reacting flow (right). This approach is used in the COCO simulation. 58
4.10 Heat transfer resistance model, where r_1, r_2 and r_3 denote the radii of copper tube that the heaters are attached to, and the inner and outer radii of the stainless steel reactor tube, respectively. k_1 and k_2 are the thermal conductivities of copper and stainless steel, k_{eff} is the effective thermal conductivity of the catalyst, determined with [71] and [72]. The values are given in table 4.14. 58

5.1 Reactor kinetics vs. catalyst bed length simulations for approximate experimental values of productivity and mass flow rate, respectively. 62
5.2 Reactor kinetics vs. catalyst bed length simulations for approximate experimental values of productivity and mass flow rate, respectively. The catalyst bed diameter is increased from 35 to 70 mm. 63
5.3 Reactor kinetics vs. catalyst bed length for an autothermal reactor simulation defined by the parameters in table 5.2. 64
5.4 Visual representation of how the chosen catalyst bed dimensions could look like in practice. 65

6.1 Representation of how the reactor height can be decreased by making the hot side from one piece. Left is the current reactor, right is a shortened reactor concept. The catalyst bed is highlighted, it does not have to decrease in size by the shortening. Note that the heaters are omitted, the shortened reactor concept would require a new heater design. 70

6.2 Visualization of how a convective heater with a meshed heat transfer surface could look like. 71

B.1 Schematic of the reactor, the sizing of individual parts are given in table B.1. 76

B.2 Sizing of the conical heat pipe support, with fin structure. 76

B.3 Cornerpiece schematic, complete with liquid collection section, without solenoid valves or connection tubes. Several dimensions are given in mm. The width of the cornerpiece is 55 mm. 77

B.4 Inlet design for a solenoid valve, where (a) is the inlet of 2 mm, (b) is the position of the solenoid valve and (c) is the inside of the reactor, connected by a 0.6 mm hole. The inlet valves are submitted to 50 bar pressure on both sides of the valve. 77

B.5 Outlet design for a solenoid valve, in this case at the liquid outlet. (a) is the liquid collection chamber, which also contains a floating magnetic 'pill'. Its magnetic field is detected by a hall effect sensor located at (b). The solenoid valve is located at (c), with a 0.6 mm hole leading towared the outlet at (d), which is designed for a luer-lock outlet, a system which allows different kinds of syringes to be attached. 77

C.1 100 $k\Omega$ NTC voltage with 100 $k\Omega$ resistor plotted against the temperature reading of an F252 High Precision Thermometer. Heating and cooling are shown separately, as this indicates the possible measurement error. A rational polynomial function is used to fit the curve. The most accurate Steinhart-Hart Equation fit is also shown. 80

C.2 100 $k\Omega$ NTC voltage with 5 $k\Omega$ resistor plotted against the temperature reading of a F252 High Precision Thermometer. Heating and cooling are shown separately, as this indicates the possible measurement error. A polynomial function is used to fit the curve. The most accurate Steinhart-Hart Equation fit is also shown. 80

D.1 Drawings and photograph of the test setup used to determine the heat pipe heat transfer correlation. The location of temperature sensors and heater are shown. 81

D.2 Experimentally determined correlation between the temperature difference over a heat pipe and a fixed supply of heat. The heat pipe is oriented vertically, with the condenser below the evaporator. 82

List of Tables

2.1 Influence of several different methanol synthesis catalysts on the copper surface area and the activity. The activity was measured with 1 g of catalyst, SN = 2 (eq. 2.2), T = 523K, p = 5 MPa. Data from Saito *et al.* [22]. 14
2.2 Common working fluids and vessel materials with an indication of their operating temperature range. The temperature ranges are just an indication as they can vary with different boundary conditions, given in section 2.6.2. Data from [39, 41]. 20

3.1 Design principles used to design a new methanol synthesis reactor. Several principles are discussed in the previous chapter, the sections are given. 27
3.2 Overview of the application of the recommendations from the first ZEF prototype, the MBR, on the new reactor designs. 29
3.3 Results of the heat pipe limitation test, as seen in figures 3.4 and 3.5. 32
3.4 Additional results of the heat pipe limitation test. 32
3.5 Temperatures measured with the infrared camera for the four different supports at two different points, in the center and on the middle fin. Sm = Smooth, SB = Sandblasted, G = Grooved, GSB = Grooved and sandblasted 36
3.6 Data, calculations and results of the capillary blockage test. Fluid mixtures are given in mass fractions. Surface tension values from [66]. Capillary length calculated with equation 3.5. Blockage can be seen in figure 3.12. 37
3.7 Gasket material properites for materials available for the Tri-Clamp system. Maximum temperatures from [67]. Chemical compatibility from [68]. Prices from various companies. 42

4.1 Experimental liquid removal data for the three reactor orientations. Liquid volume is measured every 30 minutes, and run through a density analysis machine. This is converted to mass and mol fractions. Mass is used to determine the production of methanol, which is converted to space time yield. 45
4.2 Data from the base case (242^{o}C, 120g catalyst, 50 bar) compared with operation at 10^o and 20^o tilt. 47
4.3 The results of Ergun's equation for the first reactor run using Basarkar's conditions and the three productive reactor orientations. Note that Ergun's equation only gives the pressure drop over the catalyst bed. 48
4.4 Mass balance of the system in 20^o tilt orientation. CO is not included in the mass balance as it could not be measured at the time. However, the solubility of CO_2 is an order of magnitude higher than CO, and CO is therefore neglected in this analysis. 49
4.5 Molar flow rates in the reactor and the liquid output and the resulting conversion per pass. Reactor molar flow rate based on assumption that the gases in the system are dominantly 0.75/0.25 H_2/CO_2. 49
4.6 Variables used to calculate the heat losses through the insulation and the resulting losses. The temperatures are determined during steady state operation of the reactor in the base case orientation. The dimensions are labelled as 'estimated', as the actual shape is irregular and not rectangular. 50
4.7 Values used to determine the latent heat of condensation with equation 4.4. * Latent heat assumed to be equal. 51

4.8 Heat flows determined with the convective insulation losses and an energy balance. *Insulation temperature not measured, assumed insulation losses to be equal to base case. . . . 51
4.9 Heat flows determined with the mass flow rate, eq. 3.8 and an energy balance. The latent heat is part of the condenser heat transfer.. . . . 51
4.10 Energy balance data and calculations for the three reactor orientations. The energy flows are shown graphically in figure 4.4. The insulation losses are divided with the ratios of the logarithmic mean temperature difference, found in appendix E. A positive value indicates heat added to the subsystem, a negative value is heat leaving the subsystem. . . . 52
4.11 Heater input, HEX heat transfer and a ratio of the two for the three reactor orientations. 53
4.12 Cooling and heating duties of the heat exchanger for the three different reaction orientations and the associated losses, along with the temperature gradients. The heating duty divided by the mass flow rate is given as an extra useful comparison. . 54
4.13 Experimental steady state temperature sensor data for the heat pipes in ^{o}C. . . . 56
4.14 Values used to find the catalyst bed center temperature with equation 4.7. . . . 58
4.15 Simulation and calculation results for a representation of the fraction of the flow not hot enough to react, visually shown in figure 4.9. The difference with the experimental data is shown in brackets. . . . 59
4.16 Comparison of reactor performance characteristics of Basarkar, Brilman and the current reactor. ^{*1} Catalyst bed outlet temperature. ^{*2} The mass flow rate of Basarkar is an estimate and not experimentally validated. ^{*3} Condenser outlet temperature. . 59

5.1 Three highly optimized scenarios for autothermal operation with different mass flow rates. The assumptions are: no losses in the heat exchanger, 160^{o}C temperature drop over the heat exchanger, 20^{o}C temperature drop over the condenser, 50W insulation losses and STY of 20 mmol MeOH/gcat/h. . . . 61
5.2 Parameters and results of a simulation of a highly idealized autothermal reactor. . . 64

A.1 Constants used in the heat pipe limitation calculations in section 3.2.1. . . . 73

B.1 Sizing of the reactor parts given in figure B.1. All sizes are in mm. . . . 75

E.1 Logarithmic mean temperature difference data and calculations over the three insulated sections, with temperature difference between the in- and outlets of the sections with the ambient temperature, measured to be 21.6^{o}C. The numbering of the temperature is from figure 3.15. The numbering of the experiments is explained in table E.2. . . . 83
E.2 Experimental values and results for two methods of determining the mass flow rate. One uses the heat inputs in the reactor, the other uses the heat transfer through the heat exchanger, determined with the correlation from figure D.2. The insulation losses are taken into account and are assumed to be 60W. . . . 84
E.3 Heat exchanger cooling duty determined with the correlation from appendix D and with the mass flow rate over the reactor. . . . 84

F.1 Data from the base case (242^{o}C, 120g catalyst, 50 bar) compared to the base case with one heater directly heating the flow through a heat pipe support with fins. . . . 85
F.2 Data from the base case (242^{o}C, 120g catalyst, 50 bar) compared to the base case with a 0.6W in front of the condenser. . . . 85
F.3 Data from the 20^o tilt experiment (242^{o}C, 120g catalyst, 50 bar) compared to the same case but with 247^{o}C heater temperature. . . . 86

G.1 Values used to calculate η_{energy} and ξ_{HEX} for the reactors of Basarkar, Brilman and the current reactor. *Characteristics indirectly calculated from Brilman's results. . . 87

Nomenclature

Roman Symbols

A	Area	m^2
c_p	Isobaric specific heat coefficient	$Jkg^{-1}K^{-1}$
d	Diameter	m
g	Gravitational constant	ms^{-2}
$gcat$	Gram catalyst	g
h_c	Convective heat transfer coefficient	$Wm^{-2}K^{-1}$
K	Permeability	m^2
k	Thermal conductivity	$Wm^{-1}K^{-1}$
l	Length	m
m	Mass ($\dot{m}$ is mass per second)	kg
P	Pressure	Pa
Q	Heat	W
r	Radius	m
T	Temperature	K
U	Velocity	ms^{-1}
Wp	Watt-peak	W

Greek Symbols

Δ	Gradient	-
ϵ	Porosity	-
λ	Latent heat of vaporization	Jkg^{-1}
μ	Viscosity	$kgm^{-1}s^{-1}$
Ψ	Heat pipe angle against horizontal	rad
σ	Surface tension	Nm
θ	Liquid contact angle	rad
ξ	Fraction of heat input coming from the heat exchanger	

Subscripts

b	Body forces

c	Convection
cap	Capillary
g	Gravity
h	Hydraulic
i	Inner wall
l	Liquid phase
max	Maximum value
p	particle
ph	Phase transition
s	Sound
t	Tube
tot	Total
v	Vapour phase
w	Wick
eff	Effective value

Abbreviations

COCO	CAPE-OPEN to CAPE-OPEN simulation software	
EPDM	Ethylene propylene diene methylene, synthetic rubber	
FFKM	A form of FKM with a higher fluoride content	
FKM	A family of fluoroelastomers	
HDPE	High density polyethylene, plastic	
HEX	Heat exchanger	
HHV	Higher Heating Value	
MBR	Modified Brilman Reactor	
MeOH	Methanol	
PEEK	Polyether ether ketone, thermoplastic resin	
POM	Polyoxymethylene, plastic	
ppm	Parts per million	
PTC	Power-to-chemicals	
PTFE	Polytetrafluoroethylene	
PV	Photovoltaic	
RWGS	Reverse water gas shift	
STY	Space Time Yield	$mmolgcat^{-1}h^{-1}$
ZEF	Zero Emission Fuels	

Chapter 1

Introduction

One of the largest concerns for humankind in the 21st century is rapid climate change. It is nowadays the general consensus that the rate at which our climate is changing is primarily due to increase of greenhouse gases in the atmosphere. For the most part, this increase is the result of human consumption of fossil fuels. When greenhouse gases are mentioned, the focus is most often on the most abundant greenhouse gas, carbon dioxide. Carbon dioxide is the product of practically any form of combustion and makes up for around 0.04% or 400 ppm of our atmosphere. Carbon dioxide is an essential element of life on our planet as it is consumed by vegetation and is the basis for the formation of more complex carbon molecules. In turn, the vegetation releases oxygen into the air, enabling practically all other forms of life. The greenhouse effect of, among other gases, carbon dioxide is also essential to life on earth. It ensures that temperature on earth stays relatively constant, protecting the planet by absorbing intense heat and radiation during the day while emitting heat and preventing heat to dissipate into space at night.

However, due to human activity, the amount of carbon dioxide and other greenhouse gases has increased at such an unnaturally high rate that our climate is rapidly changing. Seventeen of the eighteen warmest years on record (since 1880) have all taken place in the 21st century. An alarming trend can be seen when looking at the annual global mean temperatures since measurement started in 1880, see figure 1.1.

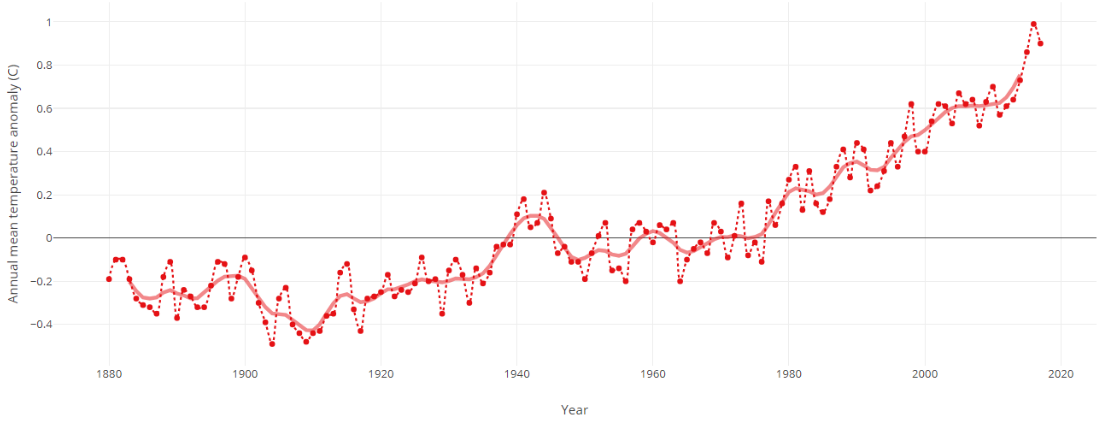

Figure 1.1: Global land-ocean mean temperature index of the period 1880-2016. The 0-line is the mean temperature of said period. Data from [1].

The rise of the carbon dioxide concentration in the atmosphere follows a similar trend. The current trend, as measured in Mauna Loa, Hawaii, can be seen in figure 1.2a. To put this into perspective, the carbon dioxide concentration in our atmosphere has been fluctuating between 180 and 300 ppm in the last 800,000 years, yet it now already exceeds 400 ppm, and is rapidly increasing [4]. The

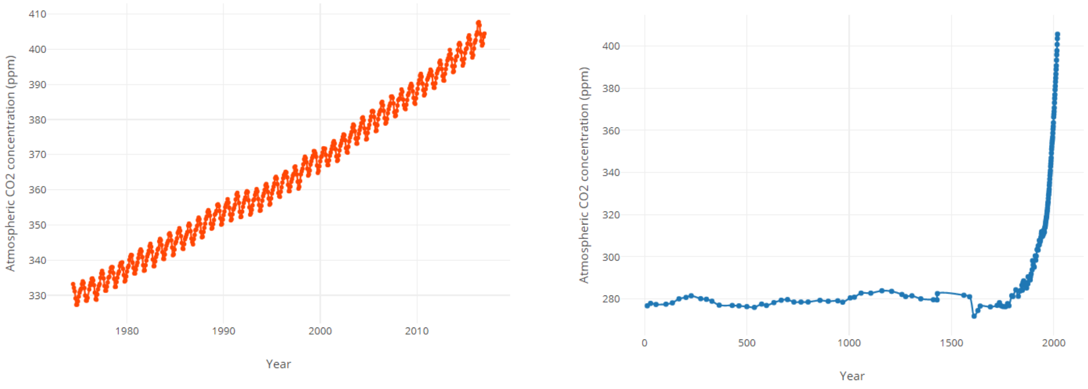

(a) (b)

Figure 1.2: Atmospheric CO2 concentrations of (a) the last 40 years in Mauna Loa, Hawaii [2], and of (b) the last two millennia, determined with ice-core samples [3].

correlation with the fluctuating temperature on Earth is easy to recognize when viewing the historical data, see figure 1.3. The last 40 years have seen an increase of 80 ppm carbon dioxide concentration in our atmosphere, a process which normally takes tens of thousands of years if nature runs its course. The major impact of the industrial revolution and modern society is clearly visible in figure 1.2b.

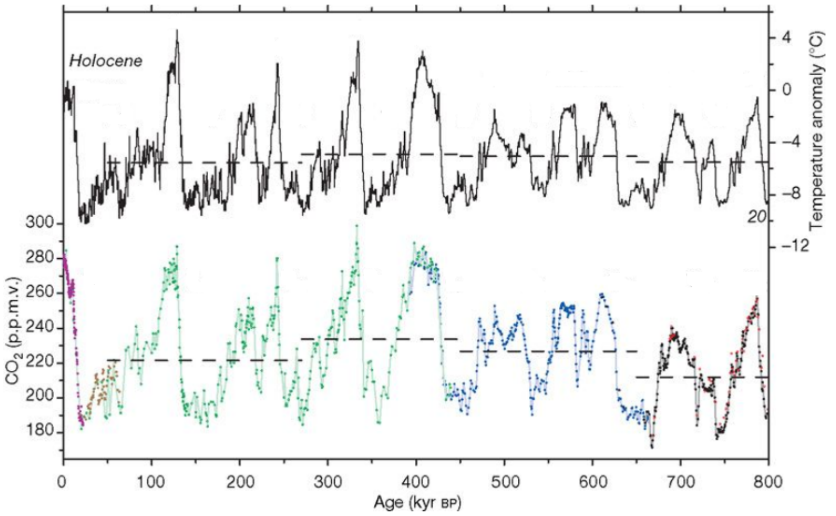

Figure 1.3: Global temperature anomaly in comparison to the present (top) and atmospheric CO_2 concentration (bottom) of the past 800,000 years, determined by Luthi *et al.* using Antarctic ice core samples. The left of the "Age" axis is the present age. The dashed lines represent the mean values over time frames of two glacial cycles. Figure taken from [4].

1.1 Renewable energy advancements

Thankfully, society is increasingly concerned and eager to bring about change. One of the most important steps to be taken is the transition from fossil fuels to cleaner alternatives, such as wind, solar, hydroelectric power, among others. Technological advancements, legislation, and consumer interest are driving a steady increase in the share of power generated by these alternatives to fossil fuels, especially in wind and photovoltaic power. The total global wind energy generation has increased over 800% in the period 2005-2015, and solar generation has increased over 6000% in the same period, though their combined share in the global energy consumption is still only a little over 1% [5, 6]. With the major increase in investments and installation, the price of solar PV energy is decreasing. Since 2012 the cost of solar PV energy is under 1$/Wp (Watt peak), whereas in the late '80s it was well over 10$/Wp [7]. The development of the price for solar PV power and the installed capacity can be seen in figure 1.4. Though the price might seem to be stabilizing, this is not the case. In 2016, the price reached 0.62 $/Wp; as of the time of writing in September 2018, the average price is already 0.15 $/Wp [8]. Despite all these positive advancements in the field of clean, renewable energy, there are some major challenges to be addressed.

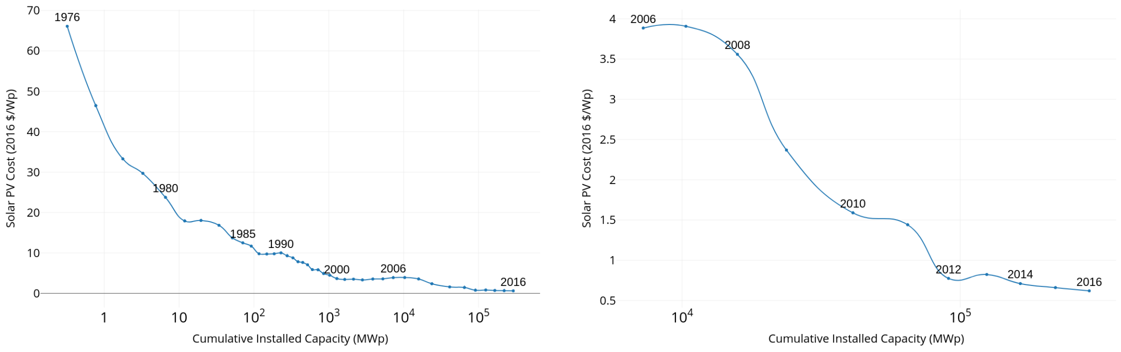

(a) (b)

Figure 1.4: Development of solar PV costs versus the total installed capacity globally for the period 1976-2016 (a), and 2006-2016 (b). Every point on the graph represents one year. Data from [7].

Reducing atmospheric carbon dioxide

First of all, the amount of carbon dioxide in the atmosphere will not decrease in the short term, even if all fossil fuels could be abandoned in a single instance. We need to reduce the amount of carbon dioxide in the air, and that can only be accomplished in two ways. One is increasing the amount of vegetation in the world, which is highly unlikely to happen with the current rate of population increase. The other is carbon capture and storage (CCS). This is a process of capturing carbon dioxide from industrial flue gases and storing it underground in old gas fields or other suitable cavities. However interesting, CCS is not the subject of this thesis.

Fluctuating energy generation

Another major challenge that accompanies the energy transition to cleaner energy sources is related to the nature of how wind and solar PV delivers energy. Wind and the sun are a fluctuating source of energy, making it near impossible to balance our energy demand with the generation of energy. Energy production can be minimal at moments that there is much demand, and vice versa. There is a need for energy storage, on a major scale. An efficient method of energy storage would enable us to flatten out the fluctuations of energy production by wind and solar PV, allowing more of these sources to make up our total energy production without causing problems. Large scale energy storage is an emerging field and much of the technology is still in the development phase, especially systems which can quickly switch on and off accordingly with the peaks of production while maintaining high efficiency. Between these competing technologies there are many differences, strengths, and weaknesses.

Electricity as an energy carrier

Another issue of wind and solar PV energy is that the energy generated is all in the form of electricity. Electricity makes up for less than 20% of the world's energy consumption [5], as many processes require other forms of energy, primarily high energy density fossil fuels, see figure 1.5. These allow for high amounts of energy in peak moments and are necessary for example in heavy industrial processes and transportation. This means that a large part of global energy consumption can not directly be powered by electricity generated by clean renewable sources. This challenge is a major driver in the development of so-called ”Power-to-Chemicals” (PTC) technology. This technology, with many different possible approaches and products, uses electricity and a base molecule containing carbon or nitrogen to produce a wide variety of chemicals, which can be used to substitute almost any kind of fossil hydrocarbon. When using carbon dioxide as the base molecule, such a chemical can be seen as ”carbon neutral”, as it releases the same amount of carbon dioxide when it is consumed. Therefore, PTC technology can tackle the challenge of storing electricity while also allowing wind and solar PV energy to power processes which normally could not be powered by electricity.

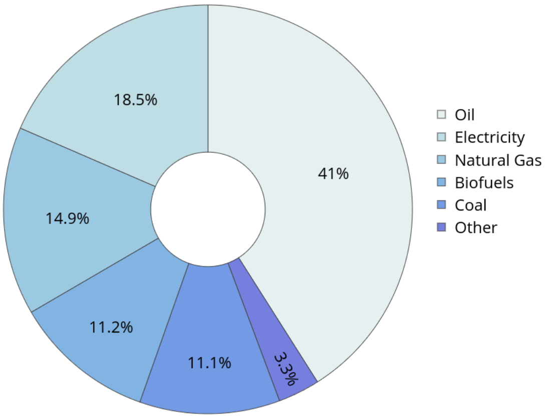

Figure 1.5: World energy consumption by fuel in 2015 [5].

1.2 Zero Emission Fuels

Zero Emission Fuels (ZEF, http://www.zeroemissionfuels.com) is a technology startup from Delft, the Netherlands, which aims to produce methanol as a carbon neutral fuel from sunlight and air.

ZEF sets itself apart from other PTC initiatives in its goal to create a small add-on system for a solar PV panel, whereas most other PTC processes are on a large scale with tonnes of fuel produced per year. Though the ZEF system is sized roughly like a large backpack and produces only 200 grams of methanol per day, it still falls into the process engineering classification ”macro scale”. The relatively small scale allows for rapid prototyping, development and eventually in a low production cost per unit in mass production. The small scale also allows the system to be more flexible towards the fluctuating energy input. The fluctuating energy input is perhaps the most important difference between the ZEF system and a conventional system, as it creates many challenges that can only be solved by novel concepts and designs, as well as certain considerations about the scaling of system parts.

The aim is not to make a consumer product, but rather use the system in large solar PV plants with tens of thousands of units. Such solar PV fields are a cheap source of renewable electricity, which will allow ZEF to produce carbon neutral methanol at competitive prices in an existing market. The system should be able to operate completely off the grid, which means it will capture CO_2 and water from the air and not require any form of feedstock.

Choice of output chemical
Methanol was chosen as a product for the system for a number of reasons. Primarily because it is the simplest liquid hydrocarbon, which allows for a relatively high conversion efficiency at the required scale. Since it is a liquid at atmospheric conditions, storage and transport are relatively simple, and existing infrastructure can be used, albeit with some adjustments. More on the advantages and disadvantages of methanol as a fuel in section 1.3.

The ZEF system can be split into four main subsystems. A schematic of the ZEF system can be seen in figure 1.6.

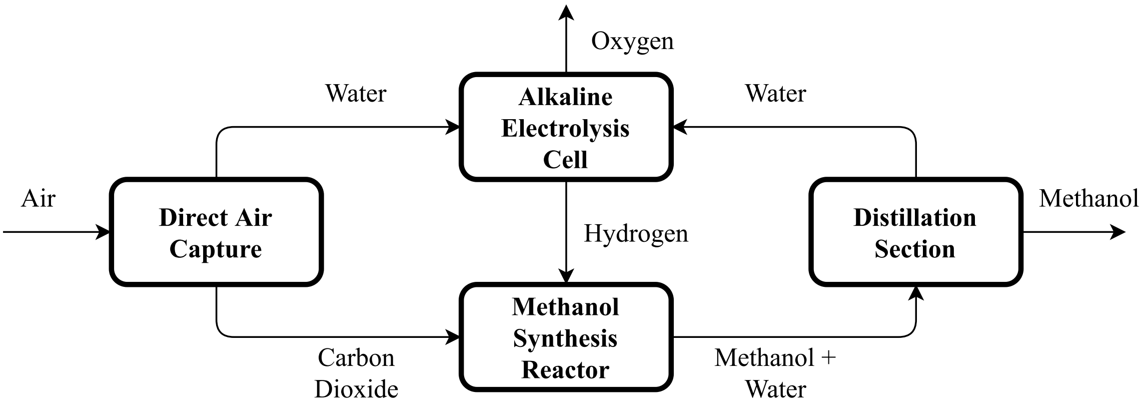

Figure 1.6: Simplified block scheme of the ZEF system. All the subsystems are powered by a solar panel, and should be able to operate fully off the grid.

Direct Air Capture
The first main subsystem is the direct air capture unit. The direct air capture unit will adsorb carbon dioxide and water from the air, the base molecules needed to produce methanol. Direct air capture systems are still in the development phase; it is therefore one of the major challenges to realize the system. Water and CO_2 are separated and compressed to elevated pressure.

Alkaline Electrolysis Cell
The water is routed to another subsystem, the alkaline electrolysis unit. Here, water is split into hydrogen and oxygen. This is the actual part of the system where electricity can be seen as stored into a chemical. However, hydrogen is not the product that ZEF wishes to produce. The hydrogen will be used as a building block to produce a liquid chemical, methanol.

Methanol Synthesis Reactor
The next essential subsystem is the methanol synthesis reactor. The carbon dioxide and hydrogen are brought together under elevated pressure and temperature. In the right conditions, in the presence of a specific catalyst, methanol and water are formed.

Distillation Section
The methanol and water from the methanol synthesis reactor are condensed and removed, after which they are split by a micro-distillation process at atmospheric pressure. The water is recycled to the electrolysis unit and the methanol is stored.

1.3 Power to Methanol

There are many fuels as a possible product for PTC processes, ranging from the simple hydrogen and ammonia to complex hydrocarbons such as synthesis diesel and gasoline. Every product has its own advantages and disadvantages, whether it be in the production process, storage or safety. Several of the main advantages of methanol are:

- Methanol is a liquid at atmospheric conditions, which makes it easy to store and distribute, without any major changes to existing infrastructure.
- The process for methanol synthesis is well known and requires little development apart from situational optimization, though innovation is always welcome.

- Methanol can be used as a fuel for many processes including vehicles. There are already many vehicles in China which use methanol as a fuel [9]. Another example of methanol as a fuel is drag racing and monster trucks in the United States of America.
- Methanol burns with a clean, clear flame. In terms of safety this has the advantage that in case of a fire, there will be no smoke from the flame, however, a disadvantage is that the clear flame can make it difficult to assess the severity of a fire.
- Methanol flames burn much slower and release less heat than other liquid fuels such as gasoline, diesel, and kerosene, which is beneficial in terms of safety.
- Methanol has little to no environmental impact in case of a leakage [10]. This is partly due to the fact that methanol dissolves well into water, which also means that methanol will not burn on top of water such as is the case with for example gasoline. This also means that a methanol fire can easily be extinguished with water.
- Methanol is commonly used in the chemical industry, which means there is an existing market.
- Methanol can be used to produce olefins, a form of hydrocarbons which have many uses, perhaps most notably the production of plastics [11]. This implies that it could be possible to convert CO_2 into plastics.

There are also a few disadvantages to using methanol as an energy carrier:

- Methanol has a lower energy density than other liquid hydrocarbon fuels such as gasoline (15.6 vs. 33 MJ/L).
- Methanol is highly toxic when ingested. As little as 10 mL can cause blindness, and 100 mL can be lethal. This leads to restrictions in terms of consumer usage.
- Methanol is less volatile than for example gasoline, which means that a methanol powered vehicle will be more difficult to start in humid or cold conditions.
- Methanol is corrosive to several metals, most notably copper and aluminum [12]. This means that certain systems will need to be modified to accommodate methanol, such as most vehicle engines, which are made from aluminum.
- The production of methanol from electricity has a lower energy efficiency than that of hydrogen. Also, carbon dioxide is needed, an extra complication which is not the case in hydrogen production.

All in all, methanol seems to be a serious contender in the field of large scale energy storage, though there is much to be said about other fuels and processes. It is an exciting time for scientists, engineers and everyone else working in the field of large scale energy storage as any process and product can still come out on top.

1.4 Research focus

The topic of this thesis is the development of the methanol synthesis reactor of the ZEF. After the first working prototype was developed, many problems and possible improvements became clear [13]. These are integrated into a new reactor design, which is built and tested in the course of this thesis. The most important design principles are the improvement of the heat integration, the driving forces of the flow and the overall productivity per gram catalyst.

1.5 Research questions

As there are endless options of parameters to experimentally optimize and/or validate, a set of research questions is formulated which is the core of the research.

1. How close can optimized heat integration and insulation bring the methanol synthesis reactor to autothermal operation?
    (a) How much can the heat integration be improved as compared to the first ZEF prototype by using heat pipes?
    (b) What are the main sources of heat loss and how can these be minimized?
2. How can the natural circulation in the reactor be improved?
3. What is the influence of tilting the reactor?
4. What is the influence of increasing the catalyst volume on absolute productivity (methanol production per hour) and on the space time yield (methanol production per gram catalyst per hour)?

1.6 Report structure

Chapter 2 contains a review of the necessary background from literature to fully understand the concepts relevant to the research questions and design choices. The design process of the reactor is shown in Chapter 3, with several simulations and experiments to validate certain design choices. It also contains a detailed description of the experimental setup, the experimental plan and several calculation methods used in the results. Chapter 4 contains the results and the following discussion. Several simulations and calculations for varying (future) scenarios are laid out in Chapter 5. The following conclusions and recommendations are found in Chapter 6.

Additional information related to various subjects can be found in the Appendices in the back of the report.

Chapter 2

Background

2.1 A brief history of methanol synthesis

1661-1923: From discovery to a commercial process

Richard Boyle discovered how to extract methanol from wood as early as 1661. This process was very inefficient and methanol, or wood alcohol as it was known then, was not a common fuel until technological advancements in the twentieth century. Sabatier proposed the production of hydrocarbons from synthesis gas (or syngas: a mixture of CO, CO_2 and H_2) in 1897 when he discovered the chemical process of hydrogenation. It was found that syngas can produce more complex hydrocarbons by increasing the temperature and pressure in the presence of certain catalysts. This led to much research into catalysts, resulting in the first commercial methanol synthesis process from BASF (Badische Anilin und Soda Fabrik) in 1923 [14]. The process operated at 300-400^oC and 300 atm, using a Cr_2O_3-ZnO catalyst. The reactions were favourable at low temperature and high pressure. However, it was necessary to increase the temperature to increase reaction speed. This resulted in a trade-off between reaction speed and efficiency. Due to low conversion rates, recycle streams were necessary, as well,as purging of unwanted byproducts. Advancements in reactor design related to those sections greatly improved production rates in the following years [15].

1924-1962: Development of catalyst and feedstock

Although it was quickly recognized that copper-containing catalysts were beneficial for methanol synthesis, it was not until 1947 that the first copper-, zinc-, and alumina-containing catalyst was patented [16]. The main reason this development took such a long time was due to the catalyst poisoning on copper catalysts caused by sulfur, which in that time was a common byproduct of syngas production. Therefore, the switch from coal reforming to methane reforming as a source of syngas was an important advancement in methanol synthesis, as methane reforming produced a more pure syngas [10, 15, 17, 18].

1960s: First low pressure methanol synthesis

A major shift in methanol synthesis technology came in 1963, when ICI (Imperial Chemical Industries) filed a patent for a ”low pressure” methanol synthesis technology, operating at 30-120 atm [10, 15, 17, 18]. The new synthesis route required a lower operating temperature, 200-300^oC, resulting in the reduction of the amount of byproducts, allowing high purity methanol production. The catalyst used was based on copper, zinc and chromium [15, 18]. This process paved the way for modern catalytic methanol synthesis technology. More on the different forms of methanol synthesis can be found in section 2.4.

1970s - 2000s: Search for alternative fuels

The oil crisis in the 1970s led to a major boost in research towards synthetic fuels, as countries searched for alternative fuels to become more independent of oil producing nations [18]. Not only did it push the development of methanol synthesis technology, but it also led to an increased focus into energy efficiency, as the price for energy was increasing. As oil prices dropped later, the interest into methanol as a fuel diminished as well. The search for alternative fuels returned in the 21st century, this time for other reasons. A strong proponent of methanol as an alternative, clean fuel is Nobel laureate George Olah. In 2005, Olah proposed a methanol economy, where methanol can become the prime chemical to store energy and to be used as a fuel and as a feedstock for all sorts of hydrocarbon products [19]. He proposed using hydrogen produced from renewable energy and captured CO_2 as feedstock for methanol synthesis, thus producing methanol in a renewable, carbon neutral manner.

Methanol from CO_2

The first commercial plant based on this principle is the aptly named George Olah Plant from CRI (Carbon Recycling International) in Iceland, which makes use of abundant geothermal energy and CO_2 from the flue gases of the geothermal plant to produce 5 million tonnes of methanol per year [20]. The plant demonstrates that it is feasible to produce carbon neutral methanol from renewable energy. Driven by the same philosophy, though a different approach, Zero Emission Fuels was founded in 2016.

2.2 Reaction kinetics

Methanol is synthesized from a mixture of H_2, CO_2, and CO, which is called synthesis gas or syngas. The exact ratio of the molecules in the syngas can differ. The ratio between the components of the syngas feed is evaluated in the *Stoichiometric Number*,

$$SN = \frac{[\mathrm{H_2}] - [\mathrm{CO_2}]}{[\mathrm{CO}] + [\mathrm{CO_2}]} \tag{2.1}$$

which is optimally slightly higher than 2 for methanol synthesis [10].

The synthesis gas is converted to methanol and water through three equilibrium reactions: the highly exothermic hydrogenation reactions of CO and CO_2,

$$\mathrm{CO} + 2\,\mathrm{H_2} \rightleftarrows \mathrm{CH_3OH} \qquad \Delta H_{298K} = -90.8kJ/mol \tag{2.2}$$

$$\mathrm{CO_2} + 3\,\mathrm{H_2} \rightleftarrows \mathrm{CH_3OH} + \mathrm{H_2O} \qquad \Delta H_{298K} = -49.2kJ/mol \tag{2.3}$$

and the reverse water gas shift.

$$\mathrm{CO_2} + \mathrm{H_2} \rightleftarrows \mathrm{CO} + \mathrm{H_2O} \qquad \Delta H_{298K} = 41.6kJ/mol \tag{2.4}$$

The hydrogenation reactions are favoured by low temperatures, however, CO_2 requires high temperatures of above 200^oC to react due to its chemically inert properties [21]. Also, water formation has an inhibiting effect on methanol formation [22]. Therefore the conversion rate of methanol synthesis is low and requires a recycle stream where the products, water and methanol, are removed [23]. This can be achieved with a selective membrane, adsorption in a zeolite or with condensation, depending on the process.

2.3 Methanol synthesis catalyst

ZnO in methanol synthesis catalysts

As mentioned in section 2.1, methanol synthesis requires a copper catalyst, though pure copper has severe limitations. This is due to two processes that decrease the activity and lifetime of a catalyst: catalyst poisoning and thermal sintering. Both processes are effectively reduced by the addition of ZnO, which is so effective that all commercial methanol synthesis catalysts contain ZnO [24]. Fujitani *et al.* found that the presence of 50 wt% of ZnO increases catalyst activity almost 90 times compared to pure copper [25].

Catalyst poisoning

Catalyst poisoning is in most cases due to the presence of sulfur or chlorine in the feedstock. The content of H_2S should be lower than 0.05 ppm, and chlorine should be untraceable [26]. Historically, this was an issue since the syngas feedstock was produced through coal gasification, and contained sulfur. ZnO reacts with the sulfur, preventing it to poison the copper [24, 26]. However, it causes loss of the ZnO, reducing the other beneficial effects. Therefore, the use of sulfur-free feedstock was an important step in the development of methanol synthesis technology [10, 15, 17, 18].

Other causes of methanol catalyst poisoning include oxygen, dust, and high water content [26]. Oxygen causes the catalyst to oxidize, which reduces activity. Dust can physically block the pores of the catalyst. High water content, which is especially prevalent with CO_2 rich feedstocks, causes copper crystal growth which leads to sintering. Water should therefore always be removed as quickly as possible.

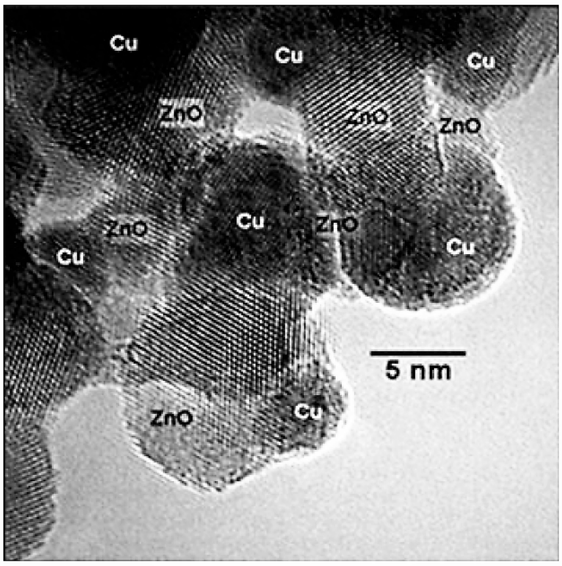

Figure 2.1: Transmission Electron Microscope image of a conventional $Cu/ZnO/Al_2O_3$ catalyst, from [26].

Thermal sintering

The temperature at which surface atoms of metals become mobile is called the Huttig temperature, which is roughly one third of the melting point [27]. Though the actual sintering temperature of metals is much higher than the Huttig temperature, the effect of mobility of the surface atoms is equivalent to sintering for very small particles [24]. The copper based catalysts used in methanol synthesis consist of many very small particles. This means that copper sintering occurs at the Huttig temperature of 453 K, which is under the reaction temperature for methanol synthesis [27]. The addition of ZnO markedly hinders the sintering process. It is suggested that ZnO bonds to copper crystallites, preventing the onset of the sintering process [24]. See figure 2.1 for a microscopic image of this phenomenon.

Since the ZnO ensures small copper crystallites, it leads to a high copper surface area. Fujitani *et al.* found a ninefold increase of copper surface area with 50 wt% ZnO [25].

Further catalyst composition

There are many other metal oxides that can be added to the catalyst, with varying properties. The main reason that an additional metal oxide is added is to increase the stability of the ZnO in the catalyst, which can otherwise deteriorate at methanol synthesis operating conditions [24]. Saito *et al.* conducted an extensive study of methanol synthesis catalysts, the results can be seen in table 2.1.

Table 2.1: Influence of several different methanol synthesis catalysts on the copper surface area and the activity. The activity was measured with 1 g of catalyst, SN = 2 (eq. 2.2), T = 523K, p = 5 MPa. Data from Saito *et al.* [22].

Catalyst	Composition (wt.-%)	Cu Surface area (m^2/gcat)	Space time yield (mmol MeOH/gcat/h)	Specific activity (mmol MeOH/m^2/h)
Cu/ZnO	50/50	36.5	16.1	0.44
Cu/ZnO/Al_2O_3	50/45/5	47.1	22.5	0.48
Cu/ZnO/ZrO_2	50/40/10	46.0	20.8	0.45
Cu/ZnO/Ga_2O_3	50/25/25	37.6	23.0	0.61
Cu/ZnO/Cr_2O_3	50/45/5	32.8	18.8	0.57
Cu/ZnO/Al_2O_3 /ZrO_2 /Ga_2O_3	*Unspecified*	44.5	24.5	0.55

This data gives a clear picture of the effect of these ternary catalyst structures. The presence of Al_2O_3 or ZrO_2 leads to an increase of the copper surface area, without a significant effect on the specific activity (the synthesis activity divided by the copper surface area). On the other hand, Ga_2O_3 and Cr_2O_3 do not affect the copper surface area as much, though they do have a significant effect on the specific activity of the catalyst. It was found that a combination (Cu/ZnO/Al_2O_3 /ZrO_2 /Ga_2O_3) gave an even higher activity, as well as less decrease of activity after pretreatment with hydrogen at 723 K due to thermal sintering. The decrease was around 15%, whereas the binary and ternary catalysts showed an activity decrease of 80% and 30%, respectively [22].

Commonly used catalysts

The most common commercial catalyst used today is Cu/ZnO/Al_2O_3. This is primarily due to the fact that alumina is by far the cheapest of the mentioned metals, while its activity is only surpassed by Cu/ZnO/Ga_2O_3 and more complex combinations containing expensive gallium. The ratio between the three components of the Cu/ZnO/Al_2O_3 catalyst varies per manufacturer, with different purposes. Different feedstocks, operating conditions or reactor types call for different catalysts. For example, when the feedstock contains contaminants such as sulfur, a catalyst with a higher ZnO content should be chosen [10, 24, 26].

Catalysts specifically for CO_2

Another interesting development in methanol synthesis catalyst research is towards catalyst stability in reactors with high water content, which is the case when CO_2 is used as carbon feedstock. It is found that the addition of SiO_2 to the catalyst can improve catalyst life and performance over time, as the silica inhibits crystallization of the catalyst due to contact with water [28, 29]. Wu *et al.* found an optimum of 0.6 wt% of SiO_2 [29]. The activity of the catalyst decreased around 15%

after 500 hours, where it remained stable, whereas the catalyst without SiO_2 showed a decrease of activity of over 22%, and further decreasing. A higher content of SiO_2 was better at preventing degradation of surface area, though it showed much lower activity [29].

2.4 Methanol synthesis processes with CO_2 as feedstock

Since BASF invented the first commercial methanol synthesis reactor in 1923, there have been many new designs for the process, most of them including the production of syngas. Almost all processes are designed for large scale operation of several thousands of tonnes per day, most using natural gas as a feedstock, including a steam reforming step, which is often included into the total heat integration. Since the ZEF methanol synthesis reactor will use pure CO_2 and H_2 as feedstock, it is more interesting to look at the reactor concepts based on the same feedstock, as this has other implications for the total process.

Lurgi process

The company Lurgi (now Air Liquide), a big player in the methanol synthesis market, was the first to design a process to produce methanol from CO_2 in 1994, which was previously assumed not to be feasible or even possible [30]. However, Lurgi achieved a viable process by using highly stable catalysts and a clever reactor design. The process consists of two reactors. Water is removed in between, therefore improving the catalyst stability and lifetime.

The first pilot plant showed that conversion rates were lower than from pure CO, and water production was a factor of 3 higher. However, the byproduct formation decreased significantly, from around 2000 ppm to 400 ppm, which implies that methanol selectivity increased [26]. This showed that, though methanol synthesis from CO_2 is relatively slow, it has some advantages which make it an interesting process for parties with access to CO_2 and H_2.

The process was aimed at chemical facilities with a surplus of H_2 and access to high purity CO_2. It was also marketed as a means to produce methanol with H_2 produced by electrolysis, which could be powered by renewable energy sources [30].

CAMERE process

Shortly after the Lurgi pilot plant, the Korea Electric Power Research Institute has designed a process, named CAMERE, to produce methanol from CO_2 and H_2, which has many similarities to the Lurgi design. There are also two reactors in series, though the first reactor in the CAMERE process is operated at conditions such that only the RWGS reaction takes place, where a large part of the CO_2 is converted to water and CO, after which the water is removed. The second reactor is the methanol synthesis reactor.

A pilot plant was built in 2004, which operated at a production of 100 kg/day. The system operating with both reactors was compared to operating with only the methanol synthesis reactor. The methanol yield was found to be roughly twice as high [31]. The space time yield was lower than that of a conventional large scale methanol synthesis reactor, 10.5 mmol MeOH/gcat/h (vs. roughly 20) [32].

2.5 Development of the ZEF methanol reactor

Due to the scale of the system which ZEF is trying to build, there is a need for a novel methanol synthesis reactor, as current systems are mostly built for much larger scales and a different energy demand. Over the past two years, the methanol synthesis reactor at ZEF has gone through a few prototype stages. The concept for the reactor was inspired by work on a similar scale by researchers at the University of Twente, which is based on the Lurgi process [33].

2.5.1 Brilman reactor

At the University of Twente, Bos and Brilman developed a novel idea for a methanol reactor. The reactor consists of a hot reaction zone and a cooler, in situ, condensation zone. There is thus no need for an external recycle stream. The reactants flow through the reactor due to natural convection. They coined the concept *LOGIC*, 'Liquid-Out Gas-In Concept'.

They proved that such a concept could produce methanol in continuous operation with a space time yield of approximately 6.4 mmol/gcat/h of methanol. A schematic of the reactor can be seen in figure 2.2.

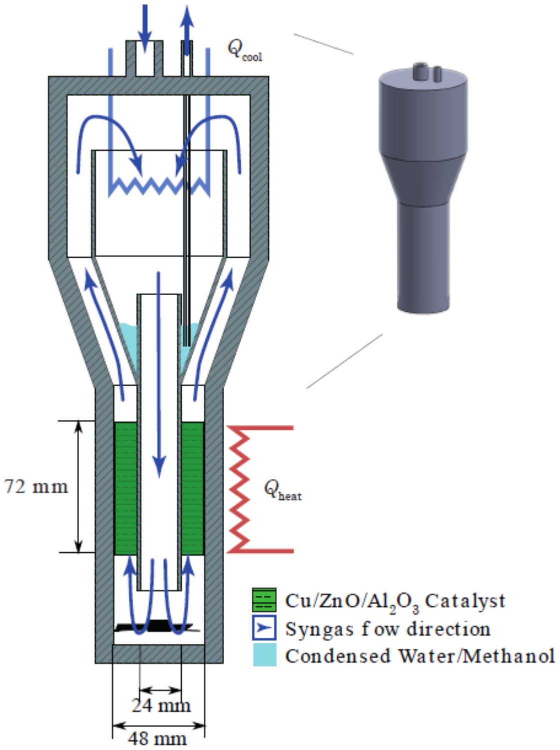

Figure 2.2: Schematic of the Brilman methanol synthesis reactor with in-situ condensation, figure from [13].

The concept of using natural convection as a driving force for the flow means that a temperature gradient is needed between the reaction and condensation zones. The temperature of the condensation zone is related to the dew point temperature of the products, which is in turn related to the pressure. An increased pressure would normally benefit reaction kinetics, though a higher pressure means a higher temperature of condensation and thus a lower temperature gradient between reaction and condensation. The researchers hypothesized that a temperature gradient of 70 K is necessary for the natural convection concept to be viable. This led them to operate at a pressure of 50 bar and a reaction temperature of 473-483 K.

As the pressure is lower than in most industrial applications, the space time yield is lower than found in the industry. For a 90.000 tonne/year Lurgi reactor, the methanol production is approximately 20 mmol/gcat/h [34].

The energy efficiency, given by the lower heating value of the methanol output, the higher heating value of the methanol input and the heater input, is roughly 20%. This is far off from the theoretical maximum of 76%. The theoretical maximum energy efficiency is derived by dividing the lower heating value of the methanol by the higher heating value of the hydrogen required to make it,

$$\eta_{\max} = \frac{[\text{Moles of } CH_3OH] \cdot [\text{LHV of } CH_3OH]}{[\text{Moles of } H_2] \cdot [\text{HHV of } H_2]} = 76\% \tag{2.5}$$

It was therefore proposed to introduce a form of heat exchange into the concept, where heat from the product flow leaving the reactor is transferred to the reactants moving towards the reactor. Through simulation, it was found that internal heat transfer mechanisms such as fin and plate or tube and plate heat exchangers would decrease the mass flux due to a local decrease in the average temperature gradient. By introducing an external heat transfer mechanism, the two flows (cooling and heating) can be separated, therefore not influencing the mass flux.

2.5.2 First ZEF prototype: MBR

The design of the methanol synthesis reactor at ZEF followed from the work at the University of Twente and aimed to implement the recommendations for heat integration. The first prototype, made and tested by Basarkar, was therefore named the Modified Brilman Reactor (MBR) [13]. To create an economically viable product, efficiency throughout the system must be as high as possible, and thus also in the methanol synthesis section. Since methanol synthesis is a process which requires heating of a reactor bed and cooling of a condensate, it follows that there is great potential for efficiency increase in the form of heat integration. The MBR was completely made from aluminum, to aid heat transfer from the heaters to the reaction zone and in the heat exchange network, and to increase cooling in the condenser zone. See figure 2.3 for a schematic.

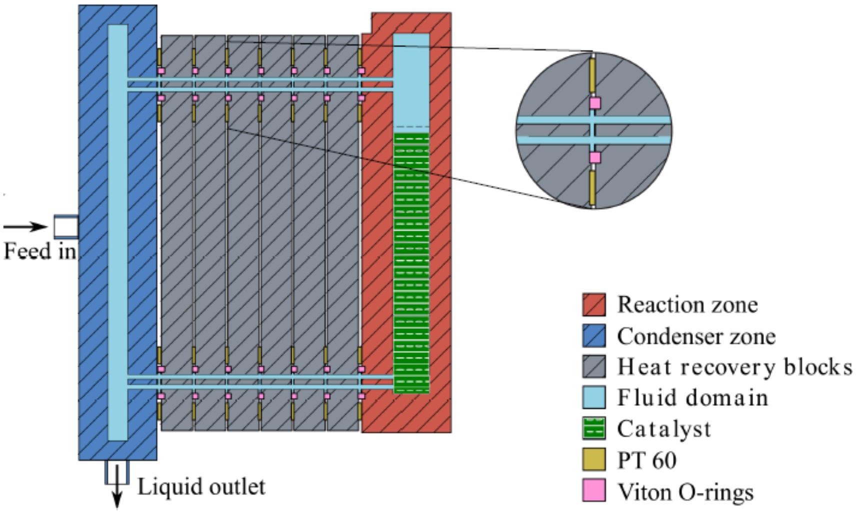

Figure 2.3: Schematic of the Modified Brilman Reactor, figure from [13].

The main findings of Basarkar's research are the following:

- A methanol production was obtained of 6.76 mmol/gcat/h at a reactor temperature of 501K.
- A lower condenser temperature increases the methanol yield due to more condensation and a larger driving force of the flow due to the temperature gradient.
- 2 mm channels cause flow blockage due to capillary forces.
- Aluminum is susceptible to corrosion in the presence of methanol, there should be no aluminum in contact with methanol in the reactor.
- The mass of the reactor is related to the startup time of the reactor. The final reactor should be as lightweight as possible.
- Insulation losses make up for over half of the total heat losses.
- Insulation between the heat exchanger parts (blocks) is recommended as this was not possible in this reactor configuration. Also, there was heat loss through steel bolts, which should be mitigated.

- Removing the liquid by hand causes faulty measurements. This should be done with a level sensor and preferably an automated valve.
- Crushing the catalyst pellets leads to a pressure drop too high for the natural convection to overcome. Installing a differential pressure sensor over the catalyst bed will generate useful data in this area.

2.5.3 Further reactor design at ZEF

During Basarkar's research, new conceptual changes were being developed and designed at ZEF. These changes were especially focused on improving the heat exchanger network and reducing the total mass of the reactor. Also, a system for automatically removing the liquids with a solenoid operated valve was designed. Especially this last feature greatly increased the difficulty of production, as the solenoid valve needs to able to resist the forces from the high pressure in the reactor. However, the most radical change of the reactor design is the use of heat pipes in the heat exchanger section instead of aluminum blocks. Heat pipes are an efficient heat transfer mechanism with low heat losses if used correctly. There were no calculations or tests to check if the heat pipes would operate correctly during the design process. A 3D model and schematic of the reactor can be seen in figure 2.4.

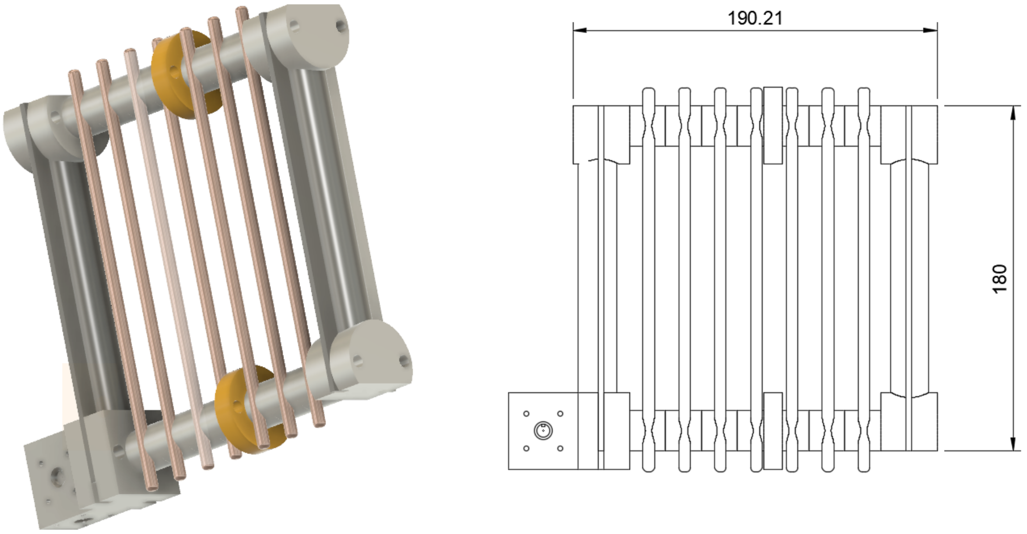

Figure 2.4: 3D drawing of the first ZEF reactor concept with heat pipes, along with a schematic view showing the dimensions in millimeters.

The reactor was designed with a 'spine' concept, which means that there are many small parts. The reason for this was that the heat pipes are attached to aluminum to conduct heat effectively, while in between heat pipes the material is stainless steel to prevent axial heat conduction through the flow channels of the heat exchanger section. This design meant that many individual parts need to be made, and between each part there is a need for an O-ring seal, and it is difficult to disassemble and assemble the reactor. Also, a large part of the reactor is still made from aluminum, which corrodes in the presence of methanol. Another flaw is that the catalyst bed diameter not larger than the MBR, something which proved to be an important recommendation, and a point of interest in this research.

In short, the new reactor design has some interesting and promising improvements, such as the heat pipe heat exchange network, the automated liquid removal, and lightweight design. However, there are many downsides to the design, with difficult implications for experimental testing. Therefore, a new design must be made, making use of the improvements, as well as incorporating more of Basarkar's recommendations. The new reactor design is shown in section 3.1.

2.6 Reactor design parameters

This section contains the theoretical background for several relevant design parameters: effects of catalyst bed sizing, the principles of heat pipes and methanol corrosion.

2.6.1 Catalyst bed sizing

The catalyst bed in the reactor is what is called a fixed bed, as the catalyst pellets are in a fixed position and in a solid state. Fixed beds are often cylindrically shaped, with axial flow. Considerations that are made when designing a fixed bed are related to the pressure drop over the bed, as well as heat and mass transfer coefficients between the fluid and the catalyst.

Most commercially available methanol synthesis catalysts have the same dimensions, a cylinder with a diameter of 5 mm and a height of 4 mm. As a rule of thumb, the ratio between the catalyst particle diameter and the tubular bed diameter (d_t/d_p) is usually 5-10 in tubular fixed bed reactors, though values of up to 20 are not uncommon [35, 36]. A lower value for d_t/d_p is unwanted as it results in a less uniform flow distribution over the catalyst [36].

There can be large velocity differences throughout the cross-section of the flow, as the flow velocity is at its highest one particle diameter from the wall, where it can be 100 % higher than the centerline velocity for a d_t/d_p of 12 [37]. However, the effects of this uneven velocity distribution are countered by radial mixing, which is high for small diameter tubular reactors [35, 38]. When $L/d_p > 10$, where L is the catalyst bed length, the conversion for a small diameter fixed bed reactor approaches that of an ideal plug flow, despite the non-uniform flow velocity [35], assuming a uniform temperature distribution.

In larger diameter reactors, it is more difficult to achieve a uniform temperature distribution due to reduced radial heat transfer. The flow distribution can also be poor when the feed enters the reactor through a single channel [35]. It is therefore not uncommon for large scale reactors to use many separate tubes with a d_t/d_p of 5-10. A relevant example is the Lurgi methanol synthesis reactor [30].

2.6.2 Heat pipe technology

A heat pipe is an extremely effective heat transfer device, with a conductivity of 100 to thousands of times higher than that of copper [39]. Like ordinary conduction, heat pipes transfer heat passively. However, the heat pipe does not owe its high conductivity to the conductivity of the material itself, but rather to the inner workings of the heat pipe. It is essentially a hollow rod, the inside is near vacuum and lined with a wick: sintered metal, grooves or another capillary structure. It is filled with a working fluid, which is chosen based on the temperature range in which heat is transferred. Heat pipes can be designed for extremely low temperatures (30 K), up to high temperatures of 2000 K [39].

Working principle

Heat is applied to the heat pipe at the evaporator, where the heat is absorbed by the evaporating vapour due to the latent heat of vaporization. Natural convection causes the vapour to travel through the hollow core (also called the vapour core) to the condenser, where the latent heat is released again to the surroundings by the condensing liquid. The liquid is transported back to the evaporator by capillary forces in the wick. The working principle is shown graphically in figure 2.5.

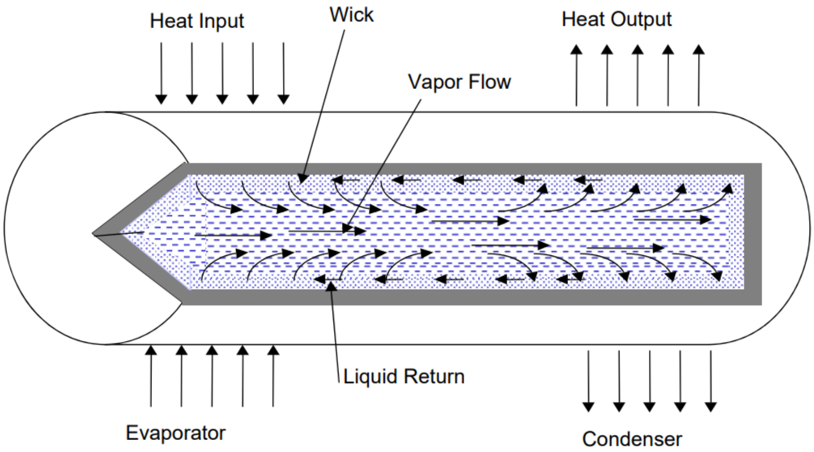

Figure 2.5: The working principle of a heat pipe [40].

The operating temperature range is determined by the material properties of the working fluid and the vessel. The operating temperature must be between the freezing point and the critical point of the working fluid for the liquid/vapour transition to be possible. There are also other boundaries and limitations, more on those in section 2.6.2. Several common working fluids and possible vessel materials can be found in table 2.2.

Table 2.2: Common working fluids and vessel materials with an indication of their operating temperature range. The temperature ranges are just an indication as they can vary with different boundary conditions, given in section 2.6.2. Data from [39, 41].

Temperature Range (^{o}C)	Working Fluid	Vessel Material
-200 to -80	Nitrogen	Stainless Steel
-70 to 60	Ammonia	Nickel, Aluminum, Stainless Steel
-45 to 125	Methanol	Copper, Nickel, Stainless Steel
5 to 230	Water	Copper, Nickel
190 to 650	Mercury	Stainless Steel
400 to 1000	Potassium	Nickel, Stainless Steel
500 to 1200	Sodium	Nickel, Stainless Steel
900 to 1500	Lithium	Niobium/Zirconium Alloy
1500 to 2300	Silver	Tantalum/Tungsten Alloy

Heat pipe applications

The applications for heat pipes extend to many fields and practises where there is a need for heat transfer, especially when high heat fluxes are required or a large distance must be covered between heat source and sink. A list of possible applications is given:

Electronics

One of the most notable and growing heat pipe applications is the cooling of electronics. With ever increasing capabilities of computer chips and other (micro-)electronic devices, there is a growing need for high heat flux dissipation methods. Heat pipes and sinks are an integral part of cooling these devices, as thermal management is becoming the limiting factor for the development of high power electronic systems [41].

Space technology

One of the earliest adopters of heat pipe technology, the space industry has been using heat pipes since the '60s. There are two main applications for heat pipes on spacecraft. The first is the dissipation of heat from electronics and other heat sources. The second, more specific for spacecraft, is the equalization of temperature on the hull of the spacecraft. When the sun is shining on one side of a spacecraft, large temperature differences can occur in the hull, which is detrimental to the materials. Heat pipes offer a method to flatten these temperature gradients [42, 43]. The inner working of the heat pipe is not affected by the vacuum of space and can be designed for the specific operating temperature range.

Nuclear power sources

Heat pipes are sometimes used to cool nuclear reactors, especially in space applications, as there is a need for high heat flux heat dissipation [44, 45]. Another application of heat pipes in nuclear facilities is the dissipation of heat from radioactive waste, as this can pose significant problems if not correctly cooled [41]. Heat pipes also offer flexibility in designing CHP nuclear power plants, sometimes completely integrated into novel reactor concepts [46].

Thermal energy storage

The most common type of thermal energy storage using heat pipes is the solar collector, which uses heat pipes to transfer heat from the sun to water [47]. Just as with the nuclear waste and CHP technologies, heat pipes are used in many different applications to transfer heat from a source, such as the sun or the ground, to a store, such as water or dry brick or sand [48]. Heat pipes are well suited for these applications due to high conductivity and low losses, along with other situational advantages such as heat pipe length.

Permafrost preservation

Oil pipelines in arctic areas often run over permafrost ground, and can potentially disrupt the natural freezing and thawing cycle of the permafrost, which can, in turn, weaken the stability of the ground and thus compromise the structure. To avoid this, the poles on which the pipelines are supported are outfitted with heat pipes, to dissipate heat from the ground to the atmosphere [49]. This application can also be found in railroads and highways over permafrost in China [50].

Heat exchangers

Heat pipes are well suited for heat exchanger systems, and can often be found in heat recovery systems with hot gas or fluid streams [39]. Hot and cold streams are often separated by a wall in standard heat pipe heat exchangers, so that heat transfer only occurs through the heat pipe itself, which is highly efficient. See figure 2.6 for an example. Such systems can be designed in many shapes and sizes and are fully reversible. Common applications are air conditioning systems, flue gas heat recovery and combustion air preheating.

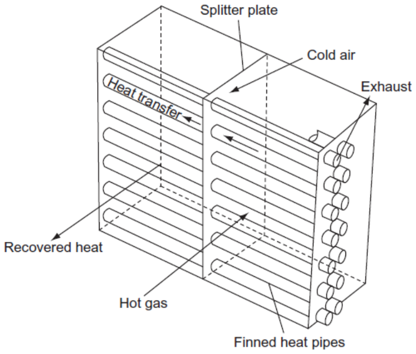

Figure 2.6: Heat pipe heat exchanger concept. Figure from [41].

Design limitations

There is more to designing heat pipes than only choosing the correct working fluid for the required temperature range. There are several limitations which are the boundaries between which the heat pipe can operate. Though there are more parameters involved, the operating temperature and required heat flux are a good indication of which limitations will be relevant. The limitations are called the viscous, sonic, entrainment, capillary and boiling limit. How they are related to the axial heat flux and temperature can be seen in figure 2.7. Every limit can be assessed when designing a heat pipe. The limitations are discussed in order of increasing temperature:

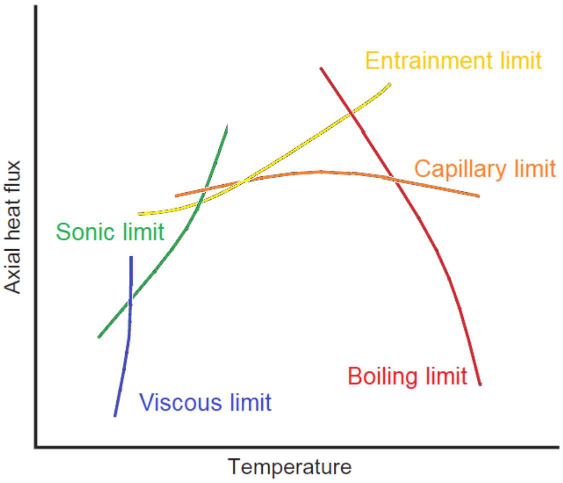

Figure 2.7: Design limitations for a heat pipe, relative to the axial heat flux and temperature of the heat pipe. The heat pipe can only operate under the curves. For example, when working close to the maximum temperature of a heat pipe, the axial flux cannot be high due to the boiling limit.

Viscous limit

The viscous limit occurs when the heat pipe reaches the lower boundary of the operating temperature range, near the triple point of the working fluid. This results in a decreasing vapour pressure gradient between the condenser and evaporator, which can eventually be too low to overcome the viscous forces in the condenser. This prevents the vapour to flow through the heat pipe, and the heat pipe will not work anymore. This limit is also often named the 'vapour pressure limit'. The viscous limit is especially important for working fluids with a low vapour density near the triple point. This can be seen from the Clausius-Clapeyron equation, (2.6).

$$dP_v = \frac{\rho_v \lambda}{T_v} dT_v \tag{2.6}$$

When the vapour density ρ_v is low, the temperature gradient leads to a low pressure gradient. At risk of reaching this limit are heat pipes with liquid metal working fluids, such as lithium or mercury, heat pipes with a long condenser section, cryogenic heat pipes and heat pipes starting up from a frozen state [39, 51]. When designing a heat pipe close to the viscous limit, equation 2.7 can be used to calculate the maximum possible heat transfer [52, 53].

$$Q_{vapour,max} = \frac{\pi r_v^4 \lambda \rho_v P_v}{12 \mu_v l_{eff}} \tag{2.7}$$

Where

- r_v is the vapour core radius (m),
- λ is the latent heat of vaporization (J/kg),
- ρ_v is the vapour density in the evaporator (kg/m^3),
- P_v is the vapour pressure in the evaporator (Pa),
- μ_v is the viscosity in the evaporator (Pa s),
- l_{eff} is the effective length of the heat pipe, which is calculated by

$$l_{eff} = \frac{l_{\text{condenser}} + l_{\text{evaporator}}}{2} + l_{\text{adiabatic}} \tag{2.8}$$

Sonic limit

The sonic limit also occurs near the triple point, at slightly higher temperatures than the viscous limit. The sonic limit is likewise related to the vapour density, as it occurs when the vapour reaches the speed of sound in the core, creating a shock wave, blocking the flow. This can only occur if the vapour density is extremely low, which is the case with liquid metals near the triple point [51]. A formula to calculate the maximum heat transfer due to the sonic limit is given in equation 2.9 [39, 41].

$$Q_{sonic,max} = \rho_v U_s \pi r_v^2 \lambda \tag{2.9}$$

Where U_s is the speed of sound for the given medium and conditions (m/s).

Entrainment limit

The entrainment limit can occur at relatively high heat flux, when the vapour velocity is sufficiently high to create a shear stress at the vapour-liquid interface which can overcome the surface tension in the liquid, causing the liquid to be carried back to the condenser with the vapour. This leads to dry-out of the liquid flow and the evaporator, crippling the performance of the heat pipe [54]. The maximum heat transfer due to the entrainment limit can be calculated with equation 2.10 [39, 41].

$$Q_{ent,max} = \pi r_v^2 \lambda \left(\frac{\sigma \rho_v}{2 r_{h,s}} \right)^{\frac{1}{2}} \tag{2.10}$$

Where σ is the surface tension coefficient (N/m) and $r_{h,s}$ is the hydraulic radius of the wick pores (m). The inclusion of the hydraulic radius in the calculation shows how the wick structure can influence the entrainment limit.

Capillary limit

The capillary limit is related to the capillary pressure forces in the wick of the heat pipe between the condenser and evaporator. If the capillary pressure is too low to return the liquid to the evaporator the heat pipe will not work. The capillary pressure must overcome the total pressure drop which consists of several factors, see equations 2.11, 2.12 [39, 41].

$$\Delta P_{cap} \geq \Delta P_{tot} \tag{2.11}$$

$$\Delta P_{tot} = \Delta P_v + \Delta P_l + \Delta P_b + \Delta P_{ph} \tag{2.12}$$

ΔP_{cap} is the capillary pressure in Pa, determined with equation 2.13.

$$\Delta P_{cap} = \frac{2\sigma}{r_{\mathit{eff}}} \cdot cos\theta \tag{2.13}$$

Where θ is the contact angle of the fluid on the wick and r_{eff} is the effective pore radius in the wick. For perfect wetting θ is 0^o. For water on a flat copper surface Shirazy *et al.* found θ to be 47^o. This value decreases with increasing porosity [55]. The capillary pressure is strongly influenced by the temperature due to the surface tension term σ. Higher temperatures result in lower surface tension and thus capillary pressure.

ΔP_v is the pressure required to displace the vapour from evaporator to condenser, determined with equation 2.14 [39, 41].

$$\Delta P_v = \frac{8\mu_v \dot{m} l_{\mathit{eff}}}{\rho_v \pi r_v^4} \tag{2.14}$$

Where $\dot{m}$ is the mass flow rate of the vapour in the heat pipe (kg/s), which can be determined by dividing the heat input by the latent heat of vaporization.

ΔP_l is the pressure required to displace the liquid from condenser to evaporator, determined with equation 2.15 [39, 41].

$$\Delta P_l = \frac{\mu_l \dot{m} l_{\mathit{eff}}}{\rho_l K A_w} \tag{2.15}$$

Where μ_l and ρ_l are the viscosity and density of the liquid in the heat pipe, in Pas and kg/m^3, respectively. A_w is the cross-sectional area of the wick (m^2), and K is the permeability of the wick (m^2). The permeability can be approximated with many different formulae, depending on the wick type. One possible approximation for the permeability in sintered copper wicks can be seen in equation 2.16 [39].

$$K = \frac{d^2 \epsilon^2}{150(1-\epsilon)^2} \tag{2.16}$$

Where d is the copper powder diameter used in the sintering process (m), and ϵ is the average porosity of the wick. While characterizing sintered copper heat pipes Leong *et al.* found these values to be 63μm and 0.45, respectively [56].

ΔP_b is the pressure drop due to body forces such as gravity, centrifugal or electromagnetic forces. Gravity is the most common and often significant factor in this term, and is given by equation 2.17 [39, 41].

$$\Delta P_g = \rho_l g l_{tot} sin\Psi \tag{2.17}$$

Where g is the gravitational constant (m/s^2), l_t is the total pipe length (m) and Ψ is the angle of the heat pipe with respect to the horizontal, being positive if the evaporator is above the condenser.

ΔP_{ph} is the pressure drop due to a phase transition, which occurs when the kinetic energy switch between vapour and liquid phase causes a pressure drop. This is generally only significant in conditions with high evaporation rates such as in liquid metal heat pipes [52].

By combining the equations 2.11 - 2.17 it is possible to derive an expression for the maximum heat transfer due to capillary limitations. A possible derivation can be found in equation 2.18. This derivation neglects phase change pressure drop and assumes no body forces other than gravity.

$$Q_{cap,max} = (\Delta P_{cap} - \Delta P_g) \cdot \left(\frac{\mu_l l_{eff}}{\lambda \rho_l K A_w} + \frac{8 \mu_v l_{eff}}{\lambda \rho_v \pi r_v^4} \right)^{-1} \tag{2.18}$$

Boiling limit

At the top boundary of the heat pipe operating temperature range, there is a risk of nucleate boiling in the wick. Vapour is trapped in the wick structure and the liquid flow is obstructed, which can lead to evaporator dry-out. This limitation is called the boiling limit, and it is the only limit related to radial heat flux. The limit is governed by two processes: the formation of bubbles and the subsequent growth or collapse of the bubbles. These factors are taken into account in the expression for the maximum heat transfer due to the boiling limit, equation 2.19 [39, 41].

$$Q_{boiling,max} = \frac{2\pi l_{eff} k_{eff} T_v}{\lambda \rho_v \ln \frac{r_i}{r_v}} \cdot \left(\frac{2\sigma}{r_n} - P_c \right) \tag{2.19}$$

Where

- T_v is the temperature of the vapour (K),
- r_i is the radius of the inner wall of the vessel (m),
- r_n is the nucleation radius (m), given by literature to be in the range 0.25 - 25 μm [39, 41, 52]. First approximations can be made with an assumed value from this range.
- P_c is the capillary pressure (Pa), determined by equation 2.13.
- k_{eff} is the effective conductivity of the wall, wick and vapour core combination (W/m K). There are many different approximations for this value for different types of wick. One expression for a sintered heat pipe is given in equation 2.20, from Ferrandi *et al.* [57].

$$k_{eff} = \frac{k_w[2 + (k_l/k_w) - 2\epsilon(1 - (k_l/k_w))]}{[2(k_l/k_w) + \epsilon(1 - (k_l/k_w))]} \tag{2.20}$$

Where k_l and k_w are the thermal conductivities of the liquid and the wick, respectively.

2.6.3 Methanol Corrosion

Corrosion on metals can be defined as the "*undesirable deterioration of a metal or alloy*" [58]. This is always something to take into account when designing chemical processes, especially for long term use. The methanol and water in the methanol synthesis reactor are called organic chemicals, a class of chemicals which are often investigated separately, as different organic chemicals often have similar effects [59].

Aluminium

A specific metal of interest is aluminium. Aluminium is relatively cheap, light and has high thermal conductivity compared to stainless steel, making it a desirable building material for many different parts of the methanol synthesis reactor. However, it is one of the conclusions of previous ZEF research that a new methanol synthesis reactor should not contain aluminium due to corrosion effects [13]. On the other hand, the conclusion is an observation and not backed by literature. Upon further investigation, corrosion is not entirely visible in the dismantled reactor channels. It is reasonable to believe that the observed corrosion was actually powdered residue from the catalyst.

Literature

There is not much literature that specifically mentions aluminium corrosion due to the presence of methanol. It is in each case written that aluminium is in most cases suitable for use with methanol, especially in the presence of water [12, 59, 60]. However, in Vargel's book, it is quantitatively shown that a 50% methanol-water mixture at 60^{o}C corrodes aluminium (3033) with a rate of 0.77 mm per year [60]. This would be disastrous for many systems, including the ZEF methanol synthesis reactor.

Conclusion

Though the data seems conclusive, it is just one very short passage without a traceable source. It is also not clear what the effect of oxygen is on corrosion behaviour. The methanol synthesis reactor is an oxygen-free, aqueous environment, an environment that seems to be not yet studied in the field of methanol or ethanol corrosion. For the time being, it is assumed it is better to avoid aluminium in the methanol synthesis reactor, though further research is necessary.

An alternative to aluminium in the reactor is stainless steel. Stainless steel is much less susceptible to chemical corrosion, notably in the presence of aqueous methanol [61]. Stainless steel will be used as much as possible in the place of aluminium, at least until more quantitative knowledge is gathered on the corrosion behaviour of aluminium in the required conditions.

Chapter 3

Reactor development

3.1 General reactor design

As mentioned in section 2.5, the methanol synthesis reactor at ZEF has undergone two development stages in the past year. The first working prototype proved that the concept of a small scale natural convection methanol synthesis reactor with heat integration works, and provided many useful recommendations. Meanwhile, a second design was developed for a reactor with a heat exchanger network based on the principle of heat pipes, with a potential for more efficient heat transfer and less losses. However, there were many faults in the design, and a new design must be made.

Principles of design

Table 3.1: Design principles used to design a new methanol synthesis reactor. Several principles are discussed in the previous chapter, the sections are given.

Design Principe	Comments	Background section
Can withstand process conditions	50 bar pressure and 230^{o}C temperature	2.5
Suitable for natural convection	Temperature gradient; circulation loop	2.5
Low corrosion	No aluminium in contact with methanol	2.6.3
Modular system	Easy (dis)assembly	
Efficient heat exchanger section	Using heat pipes if possible	2.6.2
Low heat losses	Better energy efficiency	
Low pressure drop	Higher flow rate and productivity	
Automated liquid removal	No loss of gases and pressure	
Ratio d_t/d_p between 5-10		2.6.1

Tri-Clamp and catalyst bed

The reactor is designed based on Tri-Clamp parts, which are stainless steel, modular and guaranteed leak tight and reliable. Tri-Clamp is commonly used in the food and medical industry for piping and connections. It is possible to switch out different parts with different dimensions with relative ease.

The catalyst bed diameter was chosen to be 35 mm, roughly twice that of the MBR. The catalyst used by Basarkar in the MBR was not available, and a different catalyst is used with a diameter of 6 mm instead of 5 mm. The catalyst pellet to bed ratio $d_t/d_p = 5.8$, in the optimum range of 5-10 (see section 2.6.1), whereas in the MBR $d_t/d_p = 3.6$. The length of the catalyst bed tube is 100 mm, which means $L/d_p = 20$. This ensures a near plug flow conversion rate, as it is greater than 10 (assuming a uniform temperature distribution) [35]. The rest of the system was chosen at the same diameter for a uniform flow distribution and to minimize pressure drop. The clamps used

(Tri-Clamp SH Safety Clamp®) are certified to up to 50 bar at 250^{o}C, with a failure pressure of 100 bars. More information on the dimensions of the parts can found in Appendix B. See figure 3.1 for a model of the reactor with basic dimensions.

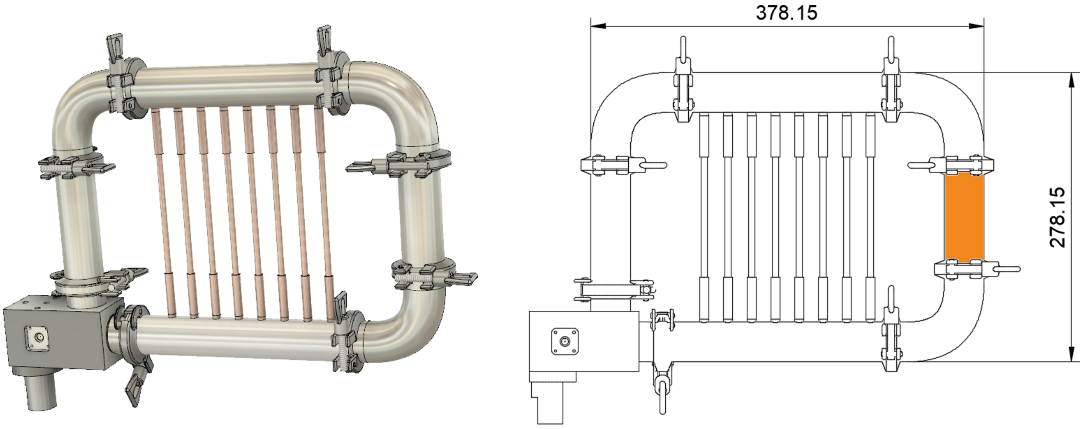

Figure 3.1: 3D model of the new reactor design, and a schematic with the dimensions. The catalyst bed is highlighted in orange. More dimensions are shown in Appendix B.

Inputs and outputs

All the inputs and outputs are placed in the same block, in the lowest point of the reactor. This 'Cornerpiece' contains two inputs and two outputs for gases, and one output for the liquids. One input is connected to pure H_2 for the start-up phase of the reactor, the other input is connected to a 0.75/0.25 H_2/CO_2 mixture for the operational phase of the reactor. One gas output is for extracting gas samples to analyze the gas composition, as well as to remove pressure if necessary. The other gas output is not a literal output, but rather a connection to the pressure sensor. The liquid output is actually a separate part, with a collection chamber and a level sensor. The level sensor is based on a floating magnet and a Hall effect sensor. This, with the solenoid valve, will allow precise removal of liquids without losing any gases. The liquid output goes through a luer-lock system into a syringe, after which it is possible to measure mass, purity and the dissolved gases. The 'Cornerpiece' can be seen in the bottom left of figure 3.1. Also, more detail on the dimensions and the inlet and outlet valve design, see Appendix B.3.

Heat exchange section

The use of the Tri-Clamp parts and their dimensions have implications for the heat exchange section. The height of the reactor is roughly 280 mm from outer wall to outer wall and 200 mm from inner wall to inner wall (empty space between top and bottom of the loop). This means the heat pipes need to be longer than 280 mm if they are to be placed all the way through the system, or shorter than 200 mm if not. Therefore, heat transfer performance will be tested for a 300 and a 200 mm heat pipe.

Also, the large channel dimensions mean there is a relatively low contact area for heat transfer. There is a need for an internal structure to increase this area. All considerations and calculations associated with the heat exchange section design are discussed in detail in section 3.3.

Sensors

The reactor contains 20 temperature sensors (100$k\Omega$ NTC), one on each end of every heat pipe and four at the corners. A pressure sensor is attached to the cornerpiece. A Hall effect sensor is used to measure the fluid level in the fluid container, which contains a floating, magnetic 'pill'.

Summary

The new reactor design incorporates many recommendations of Basarkar, while also including extra considerations for a reliable experimental setup [13]. The recommendations and considerations can be found in table 3.2.

Table 3.2: Overview of the application of the recommendations from the first ZEF prototype, the MBR, on the new reactor designs.

MBR Recommendations	Achieved	Reason achieved/not achieved
Improved heat integration	x	Heat pipes
Larger catalyst bed ($d_t/d_p = 7$)	x	Reactor sizing
Larger channels	x	Reactor sizing
Aluminium free	x	Stainless steel parts
Lightweight		Sizing & Stainless steel
Less heat losses	x	Stainless steel, heat pipes, no bolts on hot side
Automated liquid removal	x	Level sensor & Solenoid valve
Possibility for dP sensor	x	Reactor sizing

Other considerations		
Ease of production		Stainless steel cornerpiece
Modularity	x	Tri-Clamp
Reliable leak tightness	x	Tri-Clamp seals

3.2 Heat pipe validation and design

To use heat pipes in the reactor design the limitations mentioned in section 2.6.2 must be checked. Since the heat pipe is using water as the working fluid and operating high in the temperature range, it can be assumed that the viscous and sonic limits are not significant. This leaves the entrainment, capillary, and boiling limits.

3.2.1 Heat pipe limitations

The values used in the calculations can be seen in table A.1 in Appendix A. Many variables are based on assumptions, similar examples in literature or approximations. This is assumed as the calculations are simply to give an idea if the heat pipe is operating near its limitations. The values are therefore chosen for properties at the most difficult operating point, the highest temperature.

These selected values give the following heat transfer limitations:

- Entrainment limit $Q_{ent,max} = 544W$ (eq. 2.10)
- Capillary limit $Q_{cap,max} = 8.92W$ (eq. 2.18)
- Boiling limit $Q_{boiling,max} = 563kW$ (eq. 2.19)

From these values, it can be seen that the entrainment and boiling limit are much higher than the capillary limit. Therefore, it is reasonable to assume that the capillary limit will be limiting for the heat pipe performance in the reactor. This is largely due to the low surface tension of the liquid in the wick at high temperatures, and the orientation of the reactor against gravity. Figure 3.2 shows the influence of temperature on the capillary limit. As mentioned, the value for the capillary heat transfer limitation is simply an indication and will require experimental validation.

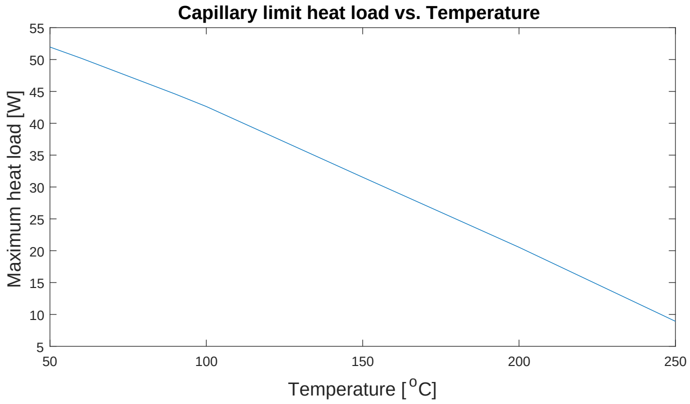

Figure 3.2: Capillary heat transfer limitation

3.2.2 Heat pipe experimental validation

A test setup was designed to test the performance of the 200 and 300 mm heat pipes. The setup consisted of two aluminum blocks with entries for the heat pipe, simulating the evaporator and condenser zones (35 mm). The blocks have a threaded opening for thermocouples. One of the blocks was heated by a heater with a power range of 0-60W. The design was initially made for usage with a plate heater, though a cylindrical (6mm) heater gave a more constant heat input. The whole setup is wrapped in glass wool insulation material and heated at a constant heat input until steady state is reached. The temperature difference between evaporator and condenser gives a clear indication of the heat transfer performance of the heat pipe. The setup can be seen in figure 3.3.

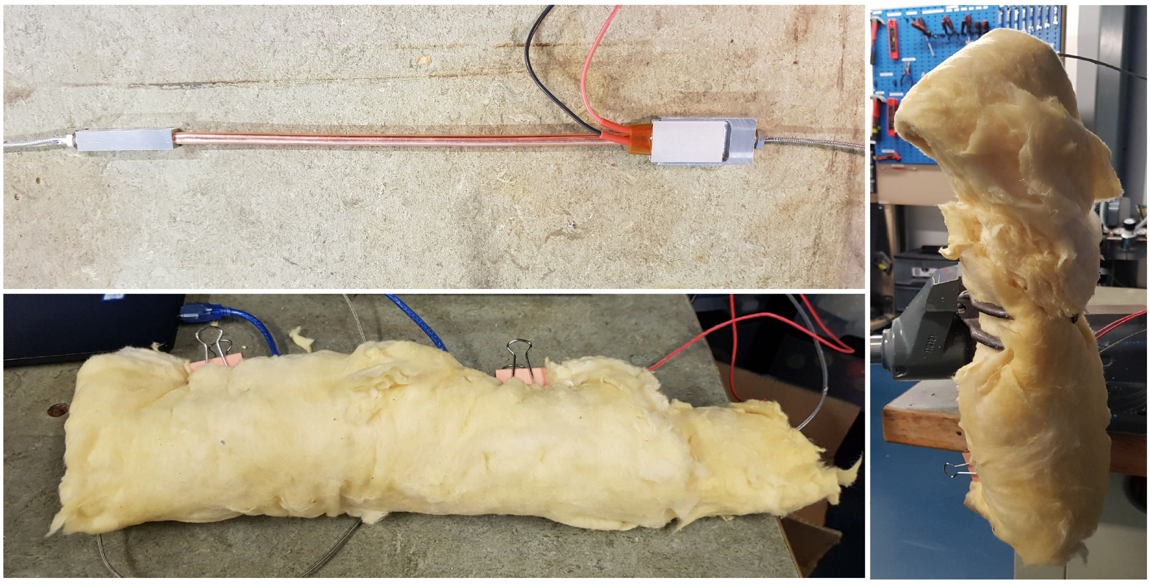

Figure 3.3: Heat pipe test setup. Top left (with plate heater) is the setup itself. Bottom left is the test in horizontal operation, right is the test in vertical operation.

The results of the 300 mm heat pipe test can be found in figure 3.4. It is clear that the heat pipe is only working correctly when the evaporator is below the condenser, which is an extra indication that it is the capillary limitation that is obstructing heat pipe operation. Nevertheless, one would expect the heat pipe to work in horizontal operation at temperatures well under the maximum, which is not the case in this test. This can indicate that the porosity of the wick is lower than assumed. Porosity is a major factor for capillary limitation, see figure 3.6. Two different sources from literature give a large difference in performance. Also, if the heat pipe is poorly manufactured the porosity might even be lower.

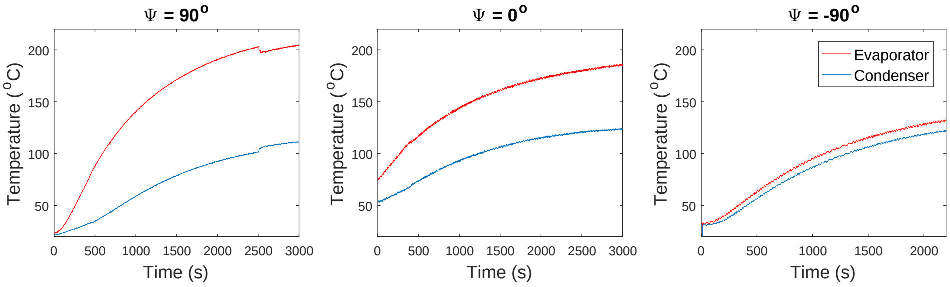

Figure 3.4: Evaporator and condenser temperature of 300mm heat pipes in three different orientations. The angle Ψ is against the horizontal, where positive means evaporator above condenser. Heat input is constant at 9.5W. Irregularities in the curves caused by adjusting insulation which was coming loose.

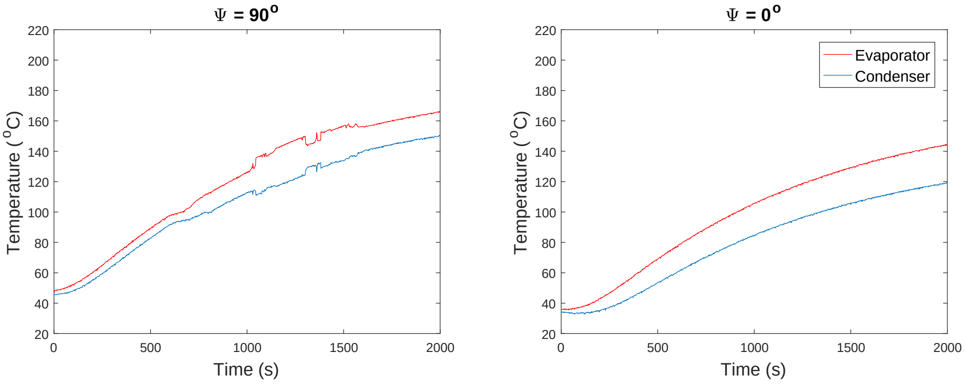

Figure 3.5: Evaporator and condenser temperature of 200mm heat pipes in two different orientations. The angle Ψ is against the horizontal, where positive means evaporator above condenser. Heat input is constant at 9.5W. Irregularities in the curves caused by adjusting insulation which was coming loose.

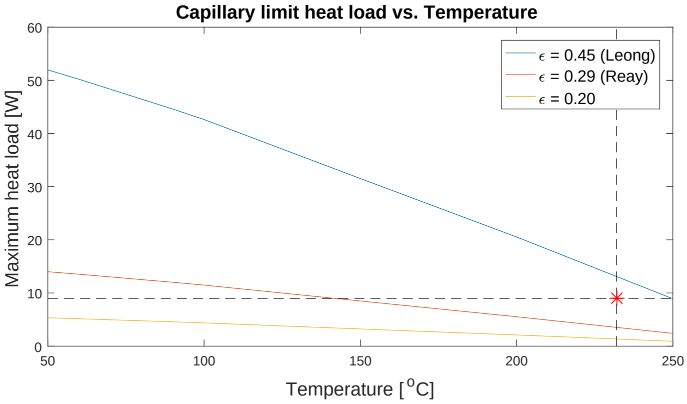

Figure 3.6: Capillary limit heat transfer for three different values of porosity. The values are based on calculations with values from table A.1.

The tests were repeated with a 200 mm heat pipe, see figure 3.5 for the results. This heat pipe is obviously operating much better than the 300 mm heat pipe. Since the operation is stable and the temperature difference is relatively small, it is assumed that this heat pipe is operating within the limitations. The results of all the tests can also be seen in table 3.3.

Table 3.3: Results of the heat pipe limitation test, as seen in figures 3.4 and 3.5.

L (mm)	Ψ	T$_e$ (^oC)	T$_c$ (^oC)	ΔT	Q (W)
300	90	208	113.75	94.25	9.5
300	0	184.5	122.75	61.75	9.5
300	-90	131.25	122.75	8.5	9.5
200	90	169.75	152	17.75	9.5
200	0	147.25	122.25	25	9.5

Once proven that the 200 mm heat pipes operate in the desired orientation to at least 170^{o}C, several tests were performed to observe the impact of higher heat input and temperature. In the horizontal orientation, the heat pipe was able to transfer 25W of heat at above 230^{o}C with the same ΔT as at 9.5W and 150^{o}C. In the vertical orientation of $\Psi = 90^o$, the ΔT had increased to 41^{o}C, which is an indication that the heat pipe is not operating correctly, though not as poor as the 300 mm heat pipe, and still better than one could expect from pure copper conduction, which can be derived from Fourier's law of heat conduction,

$$Q = k_{\text{eff}} A \frac{dT}{dx} \tag{3.1}$$

where k_{eff} is the effective combined conductive heat transfer coefficient of the copper vessel and wick, A is the cross-sectional area of the same, dT is the temperature difference over the length of the heat pipe dx. Using the values in Appendix A, a heat transfer of just over 0.9 W is found, much less than the applied 25 W.

This means that the heat pipe is still working and there is not a case of complete dry-out at the applied conditions. Nevertheless, this result means the heat transfer of the first and perhaps second heat pipe of the reactor might be less optimal, though the real heat input will be much lower than the 25 W applied in the experiment. When the heat input was lowered to 9.5W, the heat pipe reached a steady state around 200^{o}C, again with the same ΔT as before. These results can be seen in table 3.4.

Table 3.4: Additional results of the heat pipe limitation test.

L (mm)	Ψ	T$_e$ (^oC)	T$_c$ (^oC)	ΔT	Q (W)
200	0	231.5	206.5	25	25
200	90	235	194	41	25
200	90	197.5	172	25.5	9.5

3.3 Heat pipe support and fin design

As the empty space between the reactor channels is roughly 200 mm, the 200 mm heat pipes require an extended structure to transfer the heat to and from the flow. There is also a need for a relatively high contact area to transfer heat from the flow to the pipe. A design is made for a copper fin structure on a cylindrical rod which is attached to the heat pipe. The required area for the fins is calculated. One design criterion is to minimize the number of operations needed on the steel tube. Also important is to minimize capillary forces of the fin structure on the condensate, as this can cause flow blockage. This can be estimated through calculations and tested experimentally.

3.3.1 Heat transfer surface area

The surface area required to transfer the heat from the flow to the pipe is estimated with several assumptions. First of all, the temperature gradient between the two sides of the heat exchanger network should be high. As suggested by Brilman *et al.*, the minimum temperature gradient to achieve natural convection is 70 K. A higher temperature gradient and thus lower condenser temperature has several consequences:

- The driving force of the flow is greater
- More condensation, thus higher yield
- More condensation also increases energy efficiency as less water and methanol vapours return to the catalyst bed
- Higher surface tension and thus more capillary force in the fins, potentially blocking the flow
- Higher required heat transfer per heat pipe
- More heat losses due to larger heat exchanger network surface area

The advantages of a large temperature gradient seem to outweigh the disadvantages, as the fins and heat exchanger network can be designed to fit the criteria, whereas a higher driving force, purity, and yield are more difficult to obtain. Therefore, it is the aim to create a larger temperature gradient. For the calculations, this temperature gradient is set at 150 K. This means the flow will leave the top of the heat exchanger at 350 K, and enter the bottom at 325 K due to an assumed heat pipe temperature drop of 25 K.

The second major variable which must be estimated is the mass flow rate. Since the reactor diameter is approximately double that of the MBR, the volume of the catalyst bed is four times higher and the amount of catalyst in the reactor can be up to four times more. It is assumed that the reaction rate increases by a similar amount, and therefore also the mass flow rate. The MBR had a mass flow rate of 2.50e-5 kg/s when operating with a condenser temperature of 350 K. It is assumed in further calculations that the flow rate will be 10e-5 kg/s.

The isobaric specific heat, c_p, is determined via the Peng-Robinson EOS using the open source simulation software COCO. The value varies through the reactor due to the temperature and vapor-liquid fractions, though the variations are small as the c_p of hydrogen is predominant and relatively constant. The value for c_p is 2994 $Jkg^{-1}K^{-1}$ in following calculations.

The total heat flow, which is ideally all transferred through the heat exchanger network, is calculated by equation 3.2.

$$Q = \dot{m} c_p \Delta T \tag{3.2}$$

This results in a total heat flow of 40.5 W. The average heat transfer flow per heat pipe as a function of the amount of heat pipes is shown in figure 3.7.

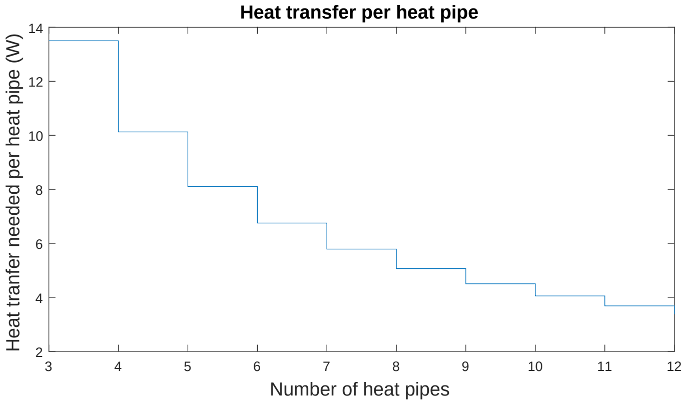

Figure 3.7: Heat transfer required per heat pipe against the amount of heat pipes.

The convective heat transfer coefficient is calculated using the vapour properties at the dew point temperature of 378 K (derived from COCO), and correlations given by Mills [62]. See equation 3.3 for the used correlations.

$$\mathrm{Ra}_L = \frac{\beta \Delta T g L^3}{\nu^2}, \qquad \overline{\mathrm{Nu}}_L = 0.82\mathrm{Ra}_L^{0.2} \quad [63], \qquad h_c = \frac{k}{L}\overline{\mathrm{Nu}}_L \tag{3.3}$$

These correlations give a convective heat transfer coefficient of roughly 105 W/m^2K, which is in the same range as previous simulations by ZEF [64]. The convective heat transfer equation, equation 3.4, will now give the required heat transfer surface area, where ΔT is the estimated average temperature difference between the flow and the fins.

$$\dot{Q}_c = h_c A \Delta T \tag{3.4}$$

The fin surface area is dependent on the number of fins, this can be seen in figure 3.8.

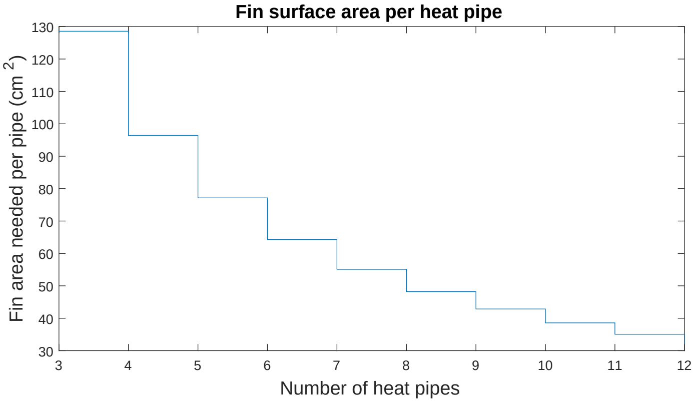

Figure 3.8: Fin area required per heat pipe against the amount of heat pipes.

It is chosen to design the heat exchanger for 8 heat pipes for the following reasons:

- Less heat transfer per heat pipe guarantees better heat pipe performance
- Less fin area required per pipe means easier fin construction and a lower chance of capillary flow blockage due to fin spacing
- More than 8 heat pipes increases the difficulty of production
- The fin structure surface can be designed to allow up to 2 heat pipes to be removed if desired

3.3.2 Fin structure design

The structure of the fins is determined by the required area and the ease of production of the complete unit, which consists of the fins on a copper tube in which the heat pipe is placed, see figure 3.9.

With 8 heat pipe supports and the reactor sizing, the spacing between the heat pipes is roughly 23 mm. The fins are designed to be 18 mm in width, as the 5 mm spacing ensures that they are not in contact with one another, which would have a negative effect on the heat exchanger performance. A spacing between the fins of 3 mm gives 9 fins and a total area of roughly 80 cm^2 (derived from the 3D drawing software Fusion 360). This is a factor 1.5 higher than the requirement for 8 heat pipes, and should still be effective if it is desired to operate with 6 or 7 heat pipes. (see figure 3.8). To neatly achieve this spacing, the copper tube on which the fins are placed is shaped conically, in such a way that varying a diameter hole in each fin is equally placed on the support. The holes are designed with teeth to improve the contact between the fins and the tube. The fins are constructed by bending a laser cut copper strip with the aid of 3D printed supports.

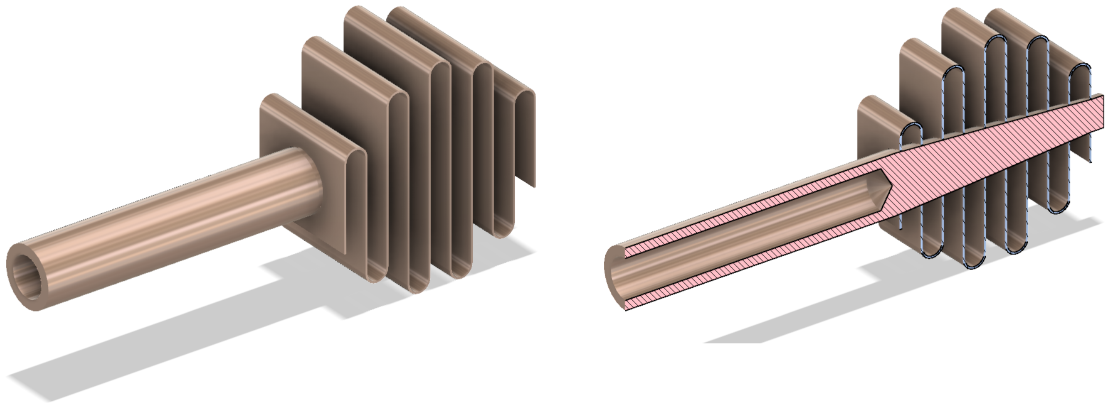

Figure 3.9: Copper fin and conical support design. See figure B.2 in the Appendix for the sizing.

Heat conduction between fins and conical support

It is crucial to have good heat transfer between the different elements of the heat exchanger section to approach heat transfer performance derived from ideal calculations. Perhaps the most critical part of this challenge is the conduction between the fins and the conical support. This due to the fact that a solid, soldered connection is not possible due to the assembly method. The fins are designed with bent 'teeth' to increase contact. However, the connection between the teeth and the smooth support is not ideal, especially after heating the supports (and fins) in the process of soldering the supports to the reactor. It is therefore desired to have a more firm connection between fins and support.

To achieve this, conical supports were prepared in four different ways:

1. Smooth (Sm): Produced by ordinary lathing.
2. Sandblasted (SB): Produced by sandblasting a smooth (Sm) support, resulting in a finely grained layer.
3. Grooved (G): Produced by lathing the last layer of material quickly.
4. Grooved and sandblasted (GSB): Same as the previous, but then with a grooved (G) support.

The four preparations are shown in figure 3.10

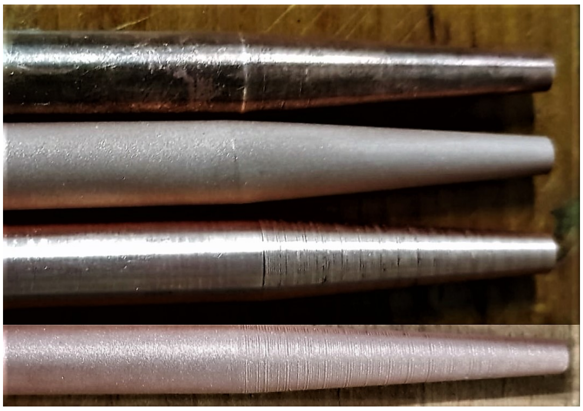

Figure 3.10: Photograph of the four conical support preparations. From top to bottom: Smooth, Sandblasted, Grooved, Grooved and Sandblasted.

A cylindrical heater, with the same diameter as the heat pipes, is placed in the support, see figure

3.9 for reference. After heating for 5 minutes at 15 W, infrared images are taken at two locations (FLIR ONE camera). The results of the test can be seen in table 3.5 and figure 3.11. It can be seen that the GSB support performs best, most importantly in the uniform distribution of heat through the whole assembly.

Table 3.5: Temperatures measured with the infrared camera for the four different supports at two different points, in the center and on the middle fin. Sm = Smooth, SB = Sandblasted, G = Grooved, GSB = Grooved and sandblasted

Preparation	T_A (center) (^oC)	T_B (fin) (^oC)
Sm	39.7	65.0
SB	54.3	68.9
G	50.2	68.6
GSB	54.7	79.9

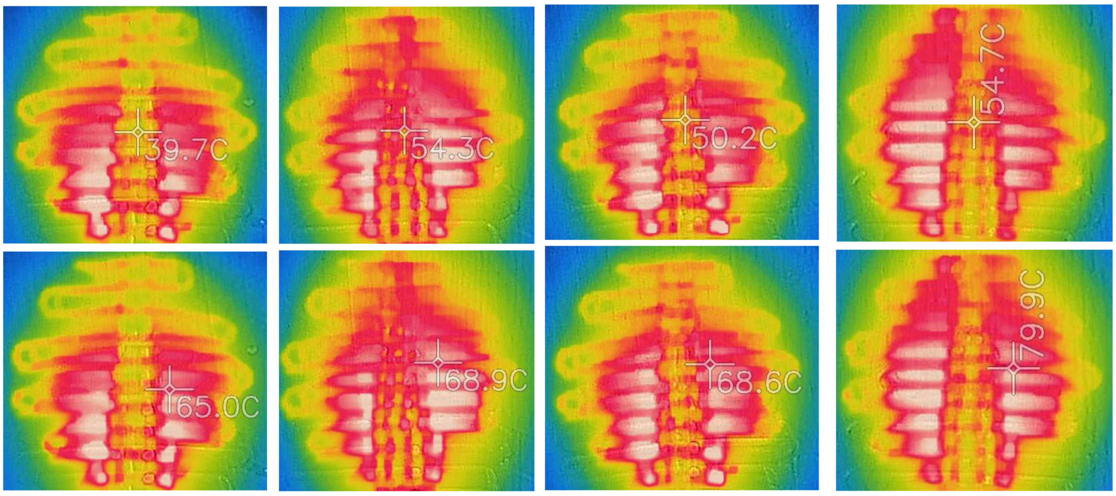

(a) Smooth support (b) Sandblasted support (c) Grooved support (d) GSB support

Figure 3.11: Heat profile of the fins and four different supports after 5 minutes of 15 W heating from the inside.

3.3.3 Capillary blockage in the fins

One of the major problems encountered in the MBR was capillary flow blockage due to condensation in the 2 mm flow channels [13]. The problem was solved enlarging the channels to 6 mm. This was done on intuition, without calculations. In this reactor, the fins are designed to be 3 mm apart, which might again cause blockage. Therefore, it is necessary to make a preliminary estimate followed by an experiment.

Capillary length equation

A way to estimate a scaling for droplets formed in the fins due to surface tension forces is with the capillary length equation,

$$L_c = \sqrt{\frac{\sigma}{\rho g sin(\theta)}} \tag{3.5}$$

where σ is the surface tension of the fluid, ρ its density, g the gravitational constant and θ the tilt angle of the reactor [65]. The natural convection driving force is neglected as it is very low due to the low velocity of the gas. The surface tension of the mixture of 0.026 N/m is taken from experimental data at 50^{o}C [66]. The density of a water/methanol mixture at 50 ^oC is 862 kg/m^3. θ is set at 15^o, as this tilt was recommended by previous work at ZEF [64]. This results in a capillary length of 3.4 mm, implying that flow blockage can occur when fins are placed 3 mm apart.

Capillary length validation

Two fin structures are designed, one with 3 mm spacing between the fins and one with 5 mm spacing. To test the difference in performance, the two fin structures are dipped into a fluid and held at an angle of roughly 15^o. Such an orientation is expected to be applied to the reactor. The formation of blocked droplets can then be observed. The fluid in which the fin structures are placed should have the same surface tension as the fluid in the reactor, which is 26.74 mN/m for a 50/50 molar methanol/water mixture at 50^oC [66]. Therefore, the test is executed with a methanol/water mixture; with a methanol mass fraction of 0.8, which has a surface tension of roughly 26 mN/m. The capillary length equation (equation 3.5) is compared to a real situation. Therefore, as an extra validation of the use of the equation the test is also executed in water, which has a higher surface tension. The results of the test are shown in figure 3.12 and table 3.6.

Table 3.6: Data, calculations and results of the capillary blockage test. Fluid mixtures are given in mass fractions. Surface tension values from [66]. Capillary length calculated with equation 3.5. Blockage can be seen in figure 3.12.

Test	Fluid	Surface tension ($10^{-3}N/m$)	Capillary length (mm)	Fin spacing (mm)	Blockage
(a)	Methanol/Water (0.8/0.2)	26	3.4	3	Yes
(b)	Methanol/Water (0.8/0.2)	26	3.4	5	No
(c)	Water	72.75	5.3	5	Yes

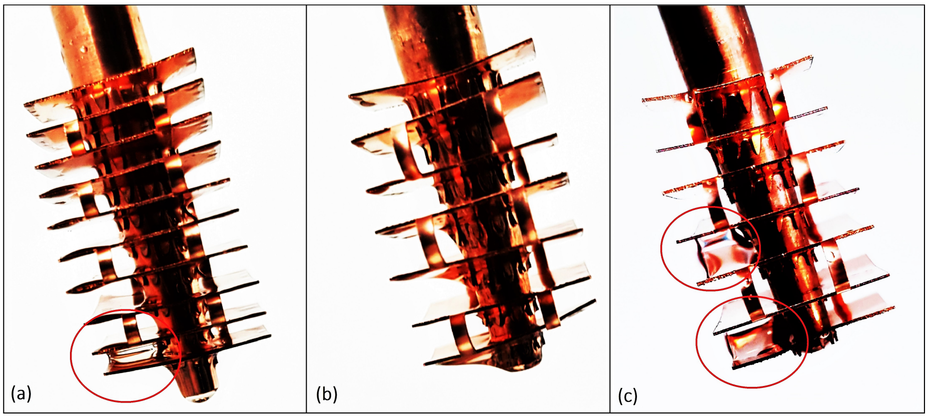

Figure 3.12: Droplets attached to fins due to capillary forces. (a) and (b) are tested in a methanol/water mixture (0.8/0.2, room temperature), with a fin spacing of 3 mm and 5 mm, respectively. (c) has a fin spacing of 5 mm and is tested in pure water at room temperature.

It can be observed ((a) and (b) in figure 3.12) that there is blockage occurring in the 3 mm spaced fins, whereas there is none in the 5 mm spaced fins for the methanol mixture, which agrees with the calculations for the capillary length (see table 3.6). The test with pure water (c) also agrees with the capillary length equation. The capillary length is calculated to be 5.3 mm; in the experiment, the 5 mm spaced fins are blocked. This is an extra validation of the use of the capillary length equation for the orientation of the setup.

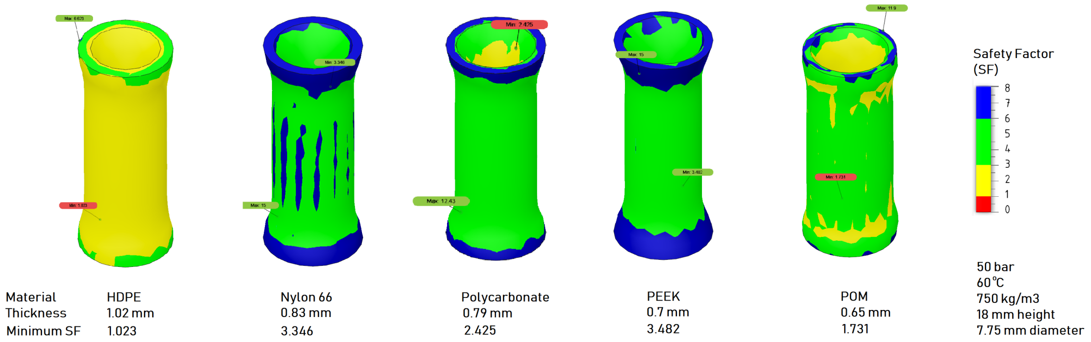

Figure 3.13: Thermal stress simulation of materials for the level sensor pill, executed in Fusion 360. The pills are designed for a total density of 750 kg/m^3, a height of 18 mm and a diameter of 7.75 mm. The coloration represents the safety factor (SF), a scale based on a stress analysis. A value lower than three indicates possible material failure.

3.4 Level sensor design

The level sensor consists of a Hall effect sensor and a floating pill with an enclosed magnet. The Hall effect sensor measures the magnetic field, and thus, after calibration, the distance of the floating pill to the bottom of the liquid collection vessel. Since the pill has to float on a light water/methanol mixture, it must be hollow. The density of the fluid is roughly 800 kg/m^3, the pill is designed to have a density of 750 kg/m^3. The pill must also withstand 50 bar pressure and temperatures in the range of 50-70 ^{o}. Five plastics were chosen as a potential material to produce the pill, with varying material properties. A thermal stress simulation was executed in Fusion 360 to compare the different materials, see figure 3.13.

PEEK, or polyetheretherketon, performed best in the simulation and is therefore chosen as material to produce the level sensor pill.

3.5 Design summary

The heat integration network is designed for 8 heat pipes, as the resulting required heat transfer is achievable, and a system with more heat pipes is more difficult to produce, whereas a system with less heat pipes will require a higher heat exchange duty per heat pipe, which is likely less efficient. The heat pipes are 200 mm in length, 6 mm in diameter and consist of a copper shell with a sintered wick and water as working fluid.

The heat pipes are connected via a copper conical tube to a fin structure. The copper support is necessary for the system to span the total height of the reactor. It is also possible to design it in such a way that the fin structure can be attached more efficiently in terms of the production method as well as the resulting heat transfer performance. To achieve this optimal attachment, the conical tubes are grooved and sandblasted. This increases the contact strength with the fin structure, which is placed on the tube with bent 'teeth' to ensure contact.

The fins are designed to be bent from one piece, with a gap of varying diameter designed to ensure constant spacing in combination with the conical tube. With the spacing at 3 mm, and a width of 18 mm, the total surface area is roughly 80 mm^2.

The 3 mm spaced fins can be (partially) blocked by capillary forces at the condensation conditions, which will negatively impact the reactor performance. However, the larger surface area is desired for heat transfer with the gaseous flow. Therefore, 5 mm spaced fins will be placed in the heat exchange network only at the point where condensation is expected, which is roughly halfway the top part of the heat exchange section. Therefore, there are four fin units with 5 mm spaced fins and twelve with 3 mm spaced fins (the bottom part of the heat exchange section contains only gases).

The fluid collection zone contains a floating, magnetic 'pill' in combination with a Hall effect sensor to measure the level of the fluid. The pill must withstand 50 bar pressure and 60 ^{o}C as well as float in a mixture of methanol and water. It was found through simulations that PEEK, or polyetheretherketon, performs best when compared to other common plastics.

3.6 Experimental setup description

The experimental setup as it is built is described in more detail in the following section. The position of all the sensors, heaters and solenoid valves are shown schematically in figure 3.14.

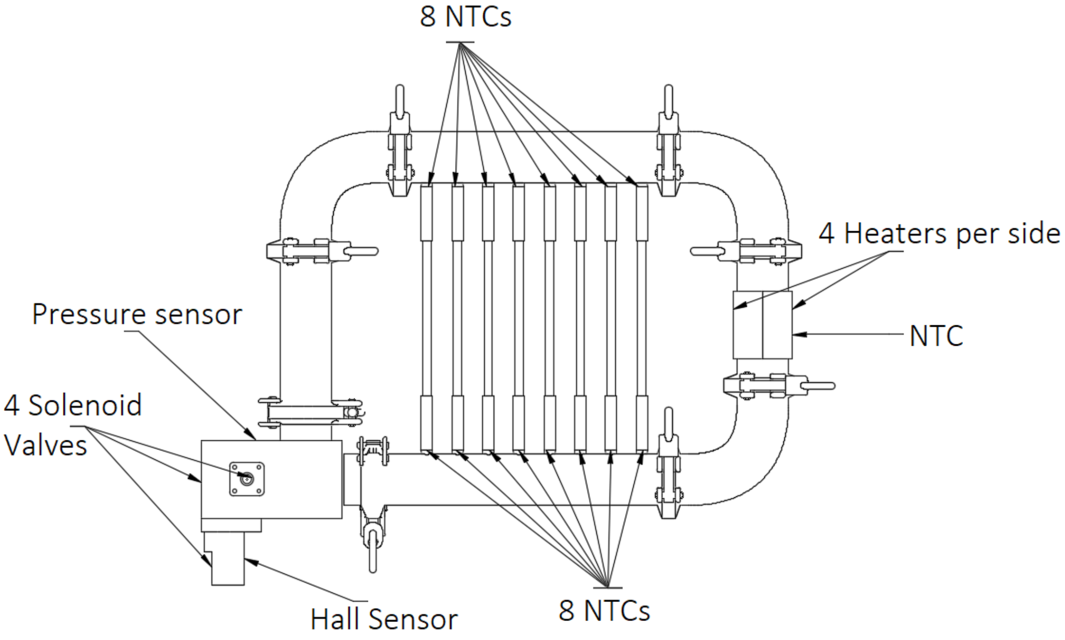

Figure 3.14: Schematic of the positions of all the sensors in the reactor.

3.6.1 Sensors

The experimental setup contains sensors for temperature, pressure and liquid collection level. They are described in the following subsections.

Temperature Sensors

The experimental setup contains 19 NTC temperature sensors (3D printer part, China, 100±1%$k\Omega$, 17 with 100±1%$k\Omega$ resistor, 2 with 5±1%$k\Omega$). 16 of the NTCs are connected to the copper heat pipe supports (100$k\Omega$). One is attached to the heating element at the reactor section (5$k\Omega$), and two are free to be placed where an extra measurement is interesting per experiment, such as the outside of the insulation (1 5$k\Omega$, 1 100 5$k\Omega$). See Appendix C for more information on how the NTCs work and how they are calibrated.

There are two different types of resistors due to the fact that it was found that 5$k\Omega$ resistors allowed for higher NTC accuracy after the 100$k\Omega$ resistors were already soldered to a printed circuit board (PCB). Replacing the resistors brought a risk of damaging the PCB, and was therefore not done.

The NTC which requires the highest accuracy at high temperatures, the NTC which controls the heater duty on the reactor, is the most accurately calibrated and uses a $5k\Omega$ resistor.

Fluid Temperature Sensors

One deviation from the design is related to the temperature sensors. Four temperature sensors were developed to run through Viton gaskets in the corners of the reactor, giving valuable data about the temperature of the fluid inside the reactor. However, these gasket sensors leaked at pressures above 10 bars, and thus can not be used in the setup. By heating the air in the reactor at low pressure, a comparison could be made between the gasket sensors (true fluid temperature) and temperature sensors on the outside, on the copper heat pipe supports. However, the temperature of a copper support is influenced by the presence of a heat pipe in operation, as heat is transferred between the heat pipe and the flow. Therefore, by removing the heat pipe from the support, a temperature is measured which is roughly the same as the temperature of the copper support on the inside of the reactor. The temperatures measured in such a manner were approximately 5^oC off from the corresponding gasket sensor, in the four corners of the reactor, see figure 3.15 for a schematic. It is chosen to operate with 6 heat pipes instead of 8 for the time being, to gather useful fluid temperature data.

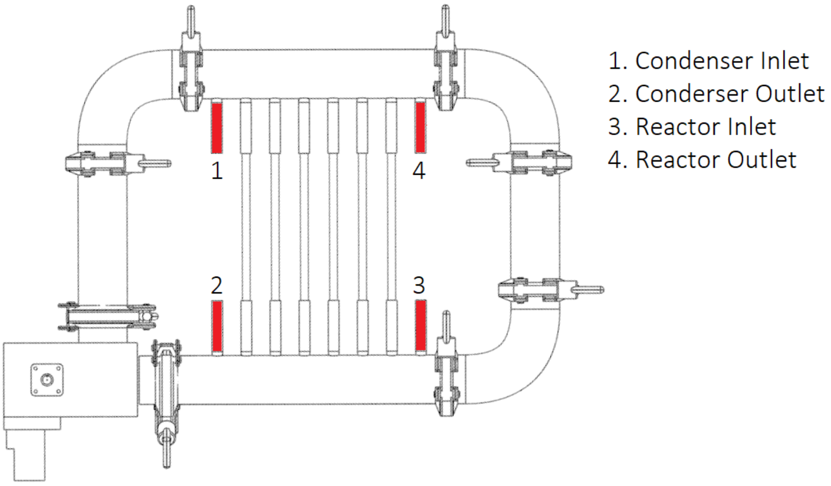

Figure 3.15: Schematic of the reactor with the location of the fluid sensors shaded in red. Note the absence of heat pipes. How they are named is given as these sensors will be referenced often in the results.

Other sensors

A pressure sensor (ADZ-SML-37.0, operating range 0-50 bars, accuracy ± 0.01 bar) is connected to the cornerpiece. The level sensor mentioned in section 3.4 is a linear hall (49E 8168G) effect sensor.

3.6.2 Reactor section

There are two items of note in the reactor section: the heaters and the catalyst. For heating, 8 40W cylindrical heaters (3D printer part, China) are placed in an aluminium block, which is clamped around the reactor, with a copper plate in between the heater block and the reactor to ensure uniform heat distribution. At full power, the heaters apply 320W of heat, powered by a 12V power supply (Adler ADL-500-12). The actual heating is approximately 270W at full power due to a lower voltage, which is necessary for optimal electronics performance, see section 3.6.3.

The catalyst used is a commercial $Cu/ZnO/Al_2O_3$ (>56%/>21%/>8%) catalyst, sourced from China. Like most commercial methanol synthesis catalysts, the height is 4 mm, though the diameter is 6 mm instead of 5 mm. A mesh is placed at the bottom of the reactor section to prevent the catalyst from dropping into the heat exchanger section.

Insulation

The reactor and heat exchanger sections are packed in by multiple layers of glass wool insulation. The insulation is layered in such a way that the sensor and heater cables run through it and are not pressed against the hot reactor walls.

3.6.3 Electronics

The experimental setup leans heavily on electronics, as there are 21 sensors, 8 heaters and the four valves are all operated by computer. The electronics can be split into three main parts: the Arduino and PCB with all the sensors, the solenoid valve control, and the heater control.

Arduino & PCB

All the programming and control is done in Arduino and operated with an Arduino Mega 2560, which is powered by an external 7.5V power supply (Velleman PSEE10). A printed circuit board (PCB) is used to reduce the amount of wiring for the temperature sensors. The sensors are all operated through an analog to digital converter (ADS1115 ADC), which greatly improves the resolution and accuracy of the sensor readings as it converts the signal from an 8-bit value to a 16-bit value. There is a maximum of 4 sensors per ADS, thus 6 ADS are required. To operate 6 ADS simultaneously, a multiplexer is required. The ADS are then in fact not run simultaneously, but rather sequentially, with a fraction of time in between.

Solenoid Valve Control

The solenoid valves (GOGOATC 211BP) are controlled with an H-Bridge (L9110S), a device normally used to control DC motors. They are powered by a 12V power supply (Adler ADL-500-12), which is also used to power the heaters. The H-Bridge is used to send a 12V pulse to open or close a solenoid valve. A 1A fuse is placed in the power line to the H-Bridge, to prevent a hydrogen leak and/or a spark or flame in case of a short circuit. It is found during the commissioning of the reactor that the H-Bridge malfunctions when powered with 12V. A lower voltage of 11.10V provides reliable and steady performance. As the same power supply is used for the H-Bridge as the heaters, this means there will be less voltage and thus less maximum heating power. However, reliable valve control is crucial for safe operation of the system.

Heater Control

The heaters are controlled with a double relay module (2PH63891A). It was noticed that the relay influences the temperature measurements due to spikes in power usage. This is fixed by using a separate 5V power supply (Mean Well RS-25-5) to power the relay. The relay is controlled by a PID controller, which determines which percentage of heating power is required to reach the setpoint temperature without overshoot, reiterating once per second. The PID controller is programmed in Matlab, using steady state heating data to determine the characteristic heating time of the system.

3.6.4 Gaskets

There are many different materials available to use as gaskets, with varying properties. As the Tri-clamp system requires a specific shape of gasket, the options are slightly limited, though the most common gasket materials are available. See table 3.7 for an overview of the properties of the available gasket materials.

Table 3.7: Gasket material properites for materials available for the Tri-Clamp system. Maximum temperatures from [67]. Chemical compatibility from [68]. Prices from various companies.

Material	Maximum Temperature (^{o}C)	Price (€)	Chemical Compatibility	Other Comments
NBR (Nitrile)	125	<1	A-Excellent	
EPDM	150	<1	A-Excellent	
Silicone	205	<1	A-Excellent	
FKM (Viton)	225	<1	C-Fair	Swells in Methanol
PTFE (Teflon)	260	1-2	A-Excellent	Stiff, need heavy clamp
FFKM (Kalrez)	260	50	A-Excellent	

It is evident that the hot side of the reactor should contain PTFE or FFKM gaskets, as these are the only available materials able to withstand the conditions without chemical degradation. PTFE requires heavier clamps, the Tri-Clamp SSH Safety Clamp, designed to operate up to 100 bar. This clamp allows a strong and uniform tightening due to its bolt system. The SH Safety Clamp uses a hinge and wingnut system, which does not provide the necessary compression for PTFE to seal effectively. As FFKM gaskets are much more expensive and could only be sourced from the United States, the PTFE gaskets with SSH Safety Clamps are used throughout the whole system.

3.6.5 Gas bottles

The system is designed to operate with multiple gas bottles, with which the input can be varied. However, for the experiments in the remainder of this thesis, a gas mixture bottle (0.75/0.25 H_2/CO_2) is used. A needle valve keeps the gas bottle and the reactor at a fixed pressure, and all pressure drop due to condensation and liquid removal is immediately replenished. A pure hydrogen bottle is also used during the start-up of the reactor.

3.6.6 Experiment operational procedure

To start up the reactor, several steps are taken:

1. Purge oxygen out of the system with pure hydrogen at low pressure (<10 bar) for roughly 2 minutes at low temperature.
2. Heat up the reactor to steady state reaction temperature (roughly 225-240 ^{o}C), with pure hydrogen at low pressure (<10 bar). This will activate the catalyst, removing the oxides from the catalyst. This will produce water, which is removed from the liquid collection zone. This will take approximately 1.5 hours.
3. Replace the pure hydrogen with 0.75/0.25 H_2/CO_2 gas mixture by purging for 2 minutes at low pressure (<10 bar).
4. Increase pressure to 50 bars, which is kept so by a needle valve on the gas mixture bottle. Pressure drop due to condensing liquids is constantly replenished.

The operation of the reactor is as follows:

1. With another gas composition and pressure, a new steady state will be realized. This takes approximately 30-45 minutes. Therefore, the first removal of liquid is after 45 minutes and is not taken into account for the experimental results.
2. The liquids are removed at certain time intervals, which gives insight in the performance characteristics over time.
3. The reactor is run like this for at least 2 hours.

To end the reactor operation the following steps are followed:

1. Release pressure through the liquid outlet for 10-20 seconds to remove as much liquid as possible.
2. Release the remaining pressure through the pressure release valve.
3. Before reaching ambient pressure, flush the system with pure hydrogen by increasing pressure and releasing it again.
4. At 2 bar, close the reactor off. No oxygen can enter the system; the following experiment will have a quicker start-up and no oxidation will be able to occur.

3.7 Experimental data analysis methods

When commissioning the reactor, it is necessary to find a base case with a steady and repeatable yield from which optimizations can be tested. This is done by trial and error. The reactor conditions for the first run are based on the reactor conditions used by Basarkar [13]. The reactor dimensions, catalyst, and heater orientation have changed. Therefore, iterative adjustments will be made to determine what set of conditions is effective for the current reactor.

The methanol content of the liquid output is determined by running samples through a density analysis machine (Anton Parr DMA 5000). Assuming the liquid is only water and methanol, their respective mass and molar fractions can be determined from the mixture density.

Every time the reactor is operated data is gathered on the performance of the heat exchanger. Heat exchanger performance is evaluated by the achieved temperature profile over the heat exchange section, as well as with an estimate of the amount of heat transferred.

3.7.1 Reaction heat

The methanol synthesis reaction releases heat, which is taken into account in energy balance. The reaction heat is given by the enthalpy of formation:

$$\mathrm{CO_2 + 3\,H_2 \rightleftarrows CH_3OH + H_2O} \qquad \Delta H_{298K} = -49.2kJ/mol \tag{3.6}$$

The enthalpy of formation is lower at higher temperatures:

$$\Delta H_{503K} = \Delta H_{298K} + \int_{298K}^{503K} c_p dT = -42.47kJ/mol \tag{3.7}$$

As the amount of moles formed is known from the yield, the reaction heat can be determined.

3.7.2 Mass flow rate and heat flows

The mass flow in the reactor can be determined with the specific heat equation:

$$Q = \dot{m} c_p \Delta T \tag{3.8}$$

Where Q is the heat input, c_p is the isobaric specific heat coefficient, estimated to be 2994 $Jkg^{-1}K^{-1}$ via Peng-Robinson EOS in COCO, and ΔT is the temperature gradient.

There are two sources of data that can be used to determine a mass flow rate. The heat flows between reactor inlet and outlet (3 and 4 in figure 3.15) are known, and the heat flows in the top section of the heat exchanger (between 4 and 1 in figure 3.15) are found with the correlation given in appendix D.2.

Insulation loss assumption

To take the insulation losses into account, an assumption must be made on how much of the insulation is lost through each reactor section. To do this, the logarithmic mean temperature difference of the sections with the ambient air is calculated. The ratio of this value for the three insulated sections (reactor bed, HEX top, and HEX bottom) is assumed to be equal to the ratio of heat lost through the insulation. The calculations and data used to determine the ratios can be found in appendix E.

For the two sections used to determine the mass balance, the ratio of ΔT_{LMTD} is roughly 0.39.

Mass flow rate equation

The two methods of determining the mass flow are compared in Appendix section E. It is concluded that the mass flow over the reactor is more accurate and will be used throughout the rest of the report. The mass flow is given by equation 3.9.

$$\dot{m} = \frac{Q_{\text{heaters}} + Q_{\text{reaction}} - 0.39 Q_{\text{insulation}}}{c_p (T_{\text{reactor,out}} - T_{\text{reactor,in}})} \tag{3.9}$$

With the mass flow rate, heat flows over various sections can be determined with equation 3.8. This will give insight into the energy balance of the system.

3.7.3 Energy efficiency

The reactor performance is also evaluated with the energy efficiency, given by:

$$\eta_{energy} = \frac{[\text{LHV of Methanol formed}]}{[\text{HHV of Hydrogen used}] + Q_{\text{heaters}}} \tag{3.10}$$

Where the lower heating value (LHV) of methanol is used as it takes into account the latent heat of released water condensing. This is not taken into account in the work of Basarkar [13] and Brilman [33]. To compare the work, the energy efficiency is recalculated with their respective results.

3.7.4 Variable reactor conditions

There are several experimental conditions that can be varied. The three most fundamental reactor conditions are:

1. Pressure: Not varied in this research. The pressure is set at 50 bar, the same as Brilman [33] and Basarkar [13].
2. Temperature: Initially set at 228^{o}C, the optimum of Basarkar's reactor. This optimum is tested for the current reactor.
3. Catalyst loading: Initially set at 40g, the same as Basarkar. As the catalyst bed dimensions are larger, catalyst loading can be increased.

Other conditions which can be varied are:

1. Tilt: One of the main research questions. The reactor will be tilted into three orientations: 0, 10 and 20 degrees.
2. Active cooling: A computer fan can be used to cool the condenser if necessary, which can influence various reactor performance characteristics.

Chapter 4

Experimental reactor design validation

In this chapter, the reactor performance is presented and discussed with an emphasis on the characteristics mentioned in the research questions: heat integration, natural convection, and reactor tilt. Design choices related to these characteristics are evaluated. The following sections relate to the reactor tilt, mass and energy balances, heat exchanger performance and a comparison to previous work.

4.1 Comparing reactor orientations

In this section, a base case is established for the reactor conditions. Reactor performance is compared for three different angles of tilt: 0^o (base case), 10^o and 20^o.

Table 4.1: Experimental liquid removal data for the three reactor orientations. Liquid volume is measured every 30 minutes, and run through a density analysis machine. This is converted to mass and mol fractions. Mass is used to determine the production of methanol, which is converted to space time yield.

Time	V (mL)	ρ (g/mL)	MeOH mass fraction	MeOH mass (g)	MeOH mol fraction	Production (mol)	STY (mmol/gcat/h)
Base Case							
0:30	9	0.8899	0.621	5.0	0.485	0.16	
1:00	9	0.8850	0.643	5.1	0.500	0.16	
1:30	9	0.8890	0.625	5.0	0.489	0.16	
2:00	9	0.8917	0.613	4.9	0.479	0.15	
Total	36			20.0		0.63	2.61
10^o Tilt							
0:30	11	0.8913	0.615	6.0	0.481	0.19	
1:00	11	0.8906	0.618	6.1	0.483	0.19	
1:30	12	0.8888	0.626	6.7	0.489	0.21	
2:00	10.5	0.8885	0.628	5.9	0.490	0.18	
Total	44.5			24.6		0.77	3.21
20^o Tilt							
0:30	14	0.8880	0.630	7.8	0.492	0.24	
1:00	14	0.8870	0.634	7.9	0.496	0.25	
1:30	14	0.8874	0.633	7.9	0.494	0.25	
2:00	14	0.8874	0.633	7.9	0.494	0.25	
Total	56			31.4		0.98	4.10

4.1.1 Base case

To determine a base case, three reactor conditions are varied: temperature, condenser cooling, and catalyst loading. Pressure is fixed at 50 bar for the following experiments as this is the same as Brilman and Basarkar [13, 33]. Other conditions are initially set equal to Basarkar's reactor conditions: a heater temperature of 228^{o}C, a fan is used to cool the condenser and the catalyst loading is 40g.

These starting conditions produce only trace amounts of methanol. The mass flow rate of 0.84 g/s (determined with equation 3.9) is higher than the 0.1 g/s assumed in the design phase and much higher than the mass flow rate of Basarkar: 0.025 g/s. As the catalyst bed diameter is larger than Basarkar, the same loading results in a short catalyst bed (roughly 35mm). Due to the high mass flow rate, the flow does not reach the reaction temperature in the short catalyst bed. As Basarkar had a lower mass flow rate, a longer catalyst bed, and a smaller catalyst bed diameter, he likely did not have this problem.

Therefore, catalyst loading is increased to 120g, filling the entire catalyst bed (100mm). The heater temperature is increased to 242^{o}C. The condenser cooling fan is removed, as cooling the condenser has a cooling effect on the whole reactor due to the high mass flow rate. See appendix F for more information on condenser cooling. With these conditions, a satisfactory, repeatable, production is established for a base case. The space time yield (STY) is roughly 2.6 mmol MeOH/gcat/h. The mass flow rate is 0.78 g/s. See table 4.1 for the experimental data used to determine the STY.

The STY is relatively low (Basarkar: 6.4, Industrial: 20 mmol MeOH/gcat/h), though significant and measurable. The production is most likely near the reactor walls, where the flow heats enough to react. The high mass flow rate is clearly a large limiting factor. As these problems were not present in Basarkar's reactor, his STY was higher.

4.1.2 Tilting of the reactor

With the base case established, the reactor performance is evaluated at 10^o and 20^o tilt. A schematic of the orientations is shown in figure 4.1. Significant results of these experiments are shown in table 4.2.

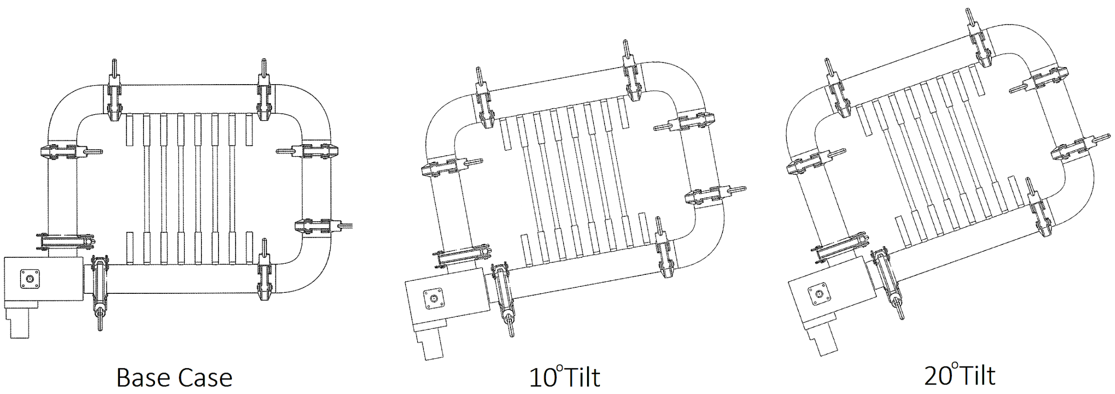

Figure 4.1: Schematic representation of the three tilt orientations.

Table 4.2: Data from the base case (242^{o}C, 120g catalyst, 50 bar) compared with operation at 10^o and 20^o tilt.

	Property		Base Case	10^o Tilt	20^o Tilt
Known:	STY (mmol MeOH/gcat/h)		2.61	3.21	4.10
Known:	Q_{Heaters}	(W)	161	143	125
Known:	$T_{\text{Reactor,out}}$	(^{o}C)	158	184	197
Calculated (eq. 3.10):	η_{energy}	(%)	23.9	29.5	36.5
Calculated (eq. 3.9):	$\dot{m}$	(g/s)	0.78	0.57	0.41

Increasing reactor tilt has a positive effect on various aspects of reactor performance. There is a strong increase in STY and energy efficiency, with a lower heater duty and higher reactor outlet temperature. These four characteristics are all correlated to the mass flow rate, see figures 4.2a-4.2d. From these correlations, it is clear that the high mass flow rate is limiting the reactor performance. Tilting the reactor decreases the mass flow rate due to decreased natural circulation effects, as predicted by Gutierrez [64]. Therefore, tilting the reactor has a positive effect on reactor performance.

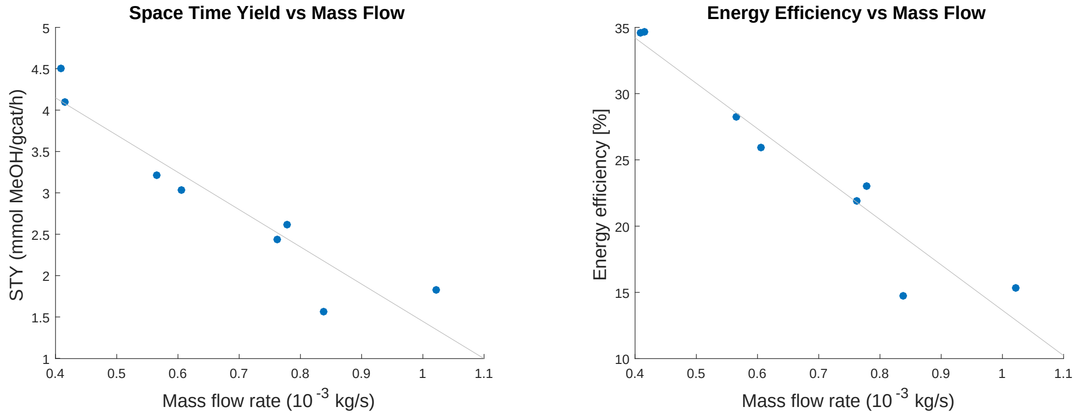

(a) Correlation between mass flow rate and space time yield.

(b) Correlation between mass flow rate and energy efficiency.

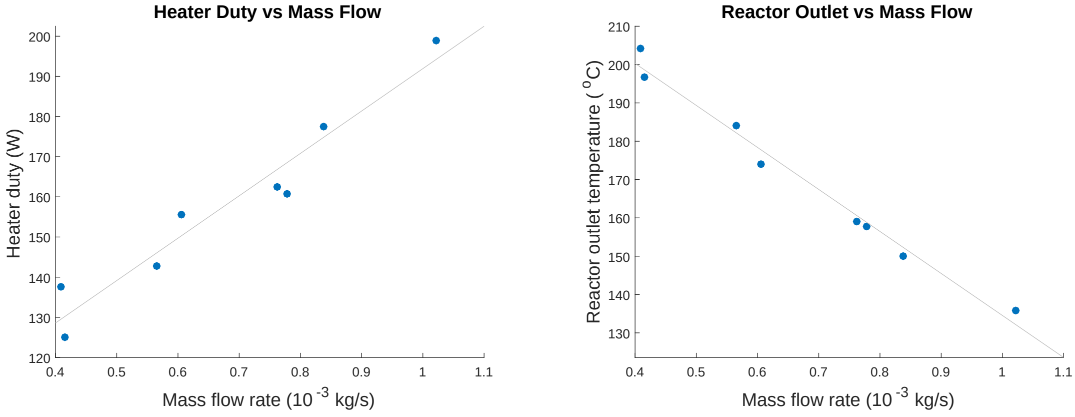

(c) Correlation between mass flow rate and heater duty.

(d) Correlation between mass flow rate and reactor outlet temperature.

Figure 4.2: Correlations between the mass flow rate and the STY (a), energy efficiency (b), heater duty (c) and reactor outlet temperature (d) for multiple experiments.

More subtle anticipated effects of tilting the reactor, such as an improved flow of condensates and improved heat pipe performance are difficult to evaluate as the effect of the change in mass flow rate is dominant. However, in the base case without tilt, there seems to be no problem with condensate flow.

4.1.3 Pressure drop with Ergun's equation

As the mass flow rate can be determined with equation 3.9, the pressure drop over the catalyst bed can be found with Ergun's equation [69]. This was not previously possible, as Basarkar did not have fluid temperature data to calculate a mass flow rate. Ergun's equation is given by:

$$\frac{|\Delta p|}{L} = \frac{150\mu}{\psi^2 D_p^2} \frac{(1-\epsilon)^2}{\epsilon^3} \frac{\dot{m}}{\rho A} + \frac{1.75}{\psi D_p} \frac{(1-\epsilon)}{\epsilon^3} \frac{\dot{m}^2}{\rho A^2} \tag{4.1}$$

Where

- L is the reactor bed length,
- μ is the viscosity of the fluid,
- ρ is the density of the fluid,
- ϵ is the void fraction of the catalyst,
- D_p is the catalyst particle diameter,
- A is the cross-sectional area of the reactor,
- ψ is a correlation factor for the particle shape, as a function of particle volume (V_p), diameter and surface area (S_p), given by

$$\psi = \frac{6V_p}{D_p S_p} \approx 1 \qquad [64] \tag{4.2}$$

The results of applying this equation to the experimental results are shown in table 4.3.

Table 4.3: The results of Ergun's equation for the first reactor run using Basarkar's conditions and the three productive reactor orientations. Note that Ergun's equation only gives the pressure drop over the catalyst bed.

Property	First Run	Base Case	10^o Tilt	20^o Tilt
$\dot{m}$ (g/s)	0.84	0.78	0.57	0.41
Δp catalyst bed (Pa)	18.8	46.8	26.3	15.2

The influence of increasing the catalyst loading from 40 to 120g on the pressure drop can be seen by comparing the first run to the base case. Note that the heater temperature is also higher for the base case than the first run (242 vs 228^{o}C). It is also clear that a lower mass flow rate results in a lower pressure drop over the catalyst bed.

4.2 Mass balances

In this section two mass balances are determined. The first is the total mass balance of the inputs and outputs of the system. This is used to find the conversion rate of CO_2 to methanol. The second is an internal mass balance to determine the conversion rate per pass in the reactor.

4.2.1 Total mass balance and carbon conversion

The total mass balance of the system is determined from the feed gases and the output. As the molar flow rates of methanol and water are known, the hydrogen content of the molecules can be used to determine the amount of hydrogen entering the system. This is exactly three times the amount of CO_2 entering the system, as the feed bottle is pre-mixed. The carbon conversion is then the ratio of methanol leaving the system and CO_2 entering the system. Water absorbs more CO_2 at high pressure than at ambient pressure. Therefore, CO_2 is released from the water when it leaves the system. The volume of gas is measured as the outlet directly enters a syringe and converted to a molar value. The results of the mass balance calculations are shown in table 4.4 and figure 4.3.

Table 4.4: Mass balance of the system in 20^o tilt orientation. CO is not included in the mass balance as it could not be measured at the time. However, the solubility of CO_2 is an order of magnitude higher than CO, and CO is therefore neglected in this analysis.

Gas	Feed (mmol/h) **Derived**	Outlet (mmol/h) **Measured**
CH_3OH	0	492
H_2O	0	502
CO_2	495	3
H_2	1486	0
Carbon conversion		99.39%

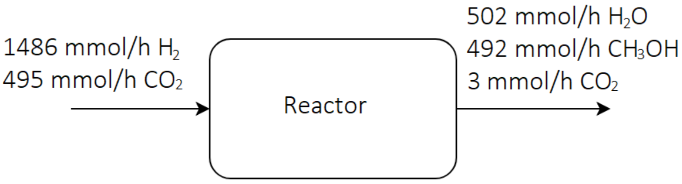

Figure 4.3: Mass balance diagram for the 20^o tilt reactor orientation.

A high carbon conversion is measured, slightly higher than Basarkar [13]. The amount of dissolved CO_2 observed leaving the system matches the mass balance.

4.2.2 Conversion per pass

The conversion per pass is determined with the molar flow rate in the reactor and the molar flow rate of the output. The ratio of the two equals the conversion rate unit of time, which is essentially the same as the conversion per pass. As 4 mols of H_2 and CO_2 react to become 2 mols of methanol and water, a factor of 2 is added to the ratio. The results of this mass balance are shown in table 4.5.

Table 4.5: Molar flow rates in the reactor and the liquid output and the resulting conversion per pass. Reactor molar flow rate based on assumption that the gases in the system are dominantly 0.75/0.25 H_2/CO_2.

Property	Base Case	10^o Tilt	20^o Tilt
Molar flow rate (mmol/s)	62	45	33
Liquid production (mmol/s)	0.18	0.22	0.28
Conversion per pass (%)	0.56	0.96	1.68

The conversion per pass is relatively low, though increasing with decreasing flow rates. A typical industrial methanol synthesis reactor has a conversion per pass of roughly 10%, though higher conversion rates exist [70]. The large difference is likely in part due to kinetics, a longer catalyst bed is required to achieve reaction equilibrium. This is researched further in section 5.2. The conversion per pass is also reduced if a part of the flow does not reach the reaction temperature, this is further analyzed in section 4.5.

4.3 Energy balance

In this section, the energy balance of the system is evaluated with two different methods. Using the mass flow rate, a more thorough energy balance is conducted for four relevant subsections of the system.

4.3.1 Insulation losses by convection

For the system as a whole, the energy balance is relatively straightforward. There is an insulated part (reactor and heat exchanger) and a non-insulated part (condenser with bolts holding up the system). It is assumed that the insulated part only loses heat through convection. By subtracting the convective insulation losses from the heater duty and reaction heat, the heat lost through the condenser zone is approximated. These are not necessarily losses, as they cause the flow to cool down and condense the methanol and water, and part of the heat comes from the latent heat of condensation.

First of all, the heat losses through the insulation are found with:

$$Q = h_c A \Delta T \tag{4.3}$$

Where h_c is the natural convection coefficient of air, A is the surface area of the insulation and ΔT is the temperature difference between the surface of the insulation and the air. As there is a wooden board behind the reactor, the temperature of the back of the board is taken for that part of the insulation. The variables used and the result of the calculation are shown in table 4.6.

Table 4.6: Variables used to calculate the heat losses through the insulation and the resulting losses. The temperatures are determined during steady state operation of the reactor in the base case orientation. The dimensions are labelled as 'estimated', as the actual shape is irregular and not rectangular.

	Property	Value
Estimated:	Dimensions (m)	0.5x0.5x0.1
Estimated:	$A_{\text{insulation}}$ (m^2)	0.45
Estimated:	A_{board} (m^2)	0.25
Known:	$T_{\text{insulation}}$ (^{o}C)	24.9
Known:	T_{board} (^{o}C)	24.2
Known:	T_{air} (^{o}C)	21.6
From [13]:	h_c (W/m^2K)	30
Calculated (eq. 4.3:	$Q_{\text{insulation}}$ (W)	64.05

4.3.2 Comparison to mass flow rate based calculations

With the convective insulation losses, the heat transferred through the condenser is calculated for the three reactor orientations. It is assumed that the insulation losses are approximately the same for each situation. These results are compared to the same values calculated with the mass flow rate and equation 3.8. To correctly calculate the condenser heat transfer, the latent heat of condensing liquids needs to be taken into account. The latent heat is given by the following equation:

$$Q_{\text{latent}} = \lambda \cdot \frac{V\rho}{t} \tag{4.4}$$

Where λ is the latent heat of condensation, V is the total volume of the liquid, ρ is the density of the liquid and t is the total time of the liquid removal. The values used are given in table 4.7.

Table 4.7: Values used to determine the latent heat of condensation with equation 4.4. * Latent heat assumed to be equal.

	Property	Base Case	10^o Tilt	20^o Tilt
Derived from COCO:	λ (J/g)	1498*	1498*	1498*
Known:	V (dm^3)	0.018	0.022	0.028
Known:	ρ (g/dm^3)	0.889	0.890	0.887
Known:	t (s)	3600	3600	3600
Calculated (eq. 4.4):	Q_{latent}(W)	7	8	10

With these values, a comparison can be made between the insulation losses determined from convection and from an internal energy balance based on the mass flow rate and the known heat inputs. The two energy balances are shown in tables 4.8 and 4.9.

Table 4.8: Heat flows determined with the convective insulation losses and an energy balance. *Insulation temperature not measured, assumed insulation losses to be equal to base case.

	Property	Base Case	10^o Tilt	20^o Tilt
Known:	Q_{Heaters} (W)	161	143	125
Known:	Q_{Reaction} (W)	3.69	4.49	5.80
Calculated (eq. 4.3):	$Q_{\text{Insulation}}$ (W)	64	64*	64*
Determined from balance:	$Q_{\text{Condenser}}$ (W)	101	84	67

Table 4.9: Heat flows determined with the mass flow rate, eq. 3.8 and an energy balance. The latent heat is part of the condenser heat transfer..

	Property	Base Case	10^o Tilt	20^o Tilt
Known:	Q_{Heaters} (W)	161	143	125
Known:	Q_{Reaction} (W)	3.69	4.49	5.80
Calculated (eq. 3.9):	$\dot{m}$ (g/s)	0.78	0.57	0.41
Calculated (eq. 4.4):	Q_{Latent} (W)	7	8	10
Calculated (eq. 3.8):	$Q_{\text{Condenser}}$ (W)	100	79	60
Determined from balance:	$Q_{\text{Insulation}}$ (W)	65	68	70

The assumption that insulation losses would be the same for the different reactor orientations is shown to be false. Since the two energy balances are a close match for the base case, the mass flow rate is considered sufficiently accurate to use in further calculations. A more detailed energy balance is possible with the mass flow rate, with internal energy flows.

4.3.3 Total energy balance and discussion

The energy balance for the four main sections of the system is shown in figure 4.4 and in table 4.10. Several interesting results are:

- The mass flow rate has a large influence on the heat flows and the temperature gradients. A high mass flow rate increases the flow of heat everywhere in the system, though the temperature gradients over each part of the system except the condenser are significantly lower.
- Insulation losses increase with decreasing mass flow. This is likely due to the higher temperatures in the system. Also, the heat pipes have higher losses due to the higher temperature. This is further discussed in section 4.4.
- A lower mass flow rate considerably reduces condenser heat loss despite more latent heat generation.
- Insulation losses in the heat exchanger section are responsible for a large part of the difference between heating and cooling duty.

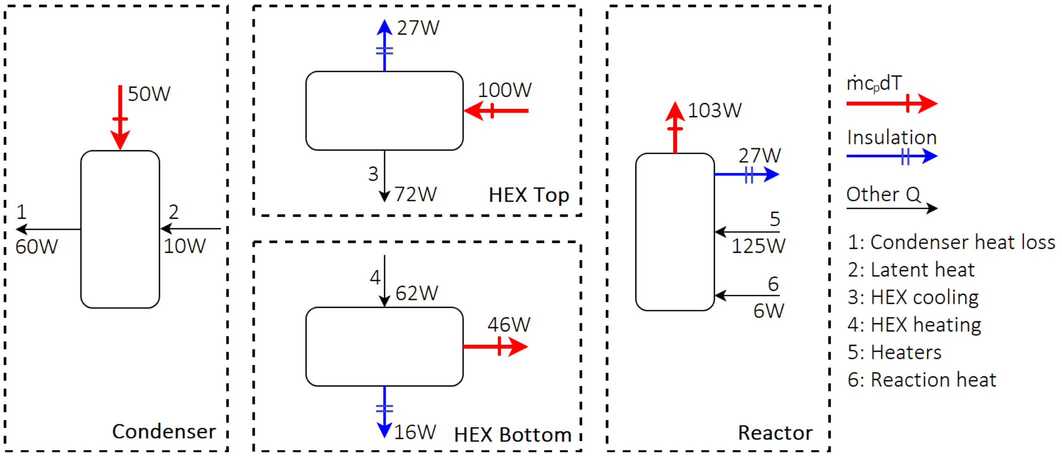
50W
1
60W
2
10W
Condenser
27W
100W
3
72W
HEX Top
4
62W
46W
16W
HEX Bottom
103W
27W
5
125W
6
6W
Reactor
ṁc_pdT
Insulation
Other Q
1: Condenser heat loss
2: Latent heat
3: HEX cooling
4: HEX heating
5: Heaters
6: Reaction heat

Figure 4.4: Energy balance diagram for the 20^o tilt reactor orientation.

Table 4.10: Energy balance data and calculations for the three reactor orientations. The energy flows are shown graphically in figure 4.4. The insulation losses are divided with the ratios of the logarithmic mean temperature difference, found in appendix E. A positive value indicates heat added to the subsystem, a negative value is heat leaving the subsystem.

	Property		Base Case	10^o Tilt	20^o Tilt
Calculated (eq. 3.9):	$\dot{m}$	(g/s)	0.78	0.57	0.41
Reactor Section					
Known:	Q_{Heaters}	(W)	161	143	125
Known:	Q_{Reaction}	(W)	3.69	4.49	5.80
Derived (table 4.9):	$Q_{\text{Insulation}}$	(W)	-25.2	-26.7	-27.4
Known:	ΔT	(^{o}C)	60.0	71.3	83.1
Calculated:	$\dot{m}c_p\Delta T$	(W)	-145	-125	-108
HEX Top					
Derived (table 4.9):	$Q_{\text{Insulation}}$	(W)	-25.2	-26.7	-27.4
Known:	ΔT	(^{o}C)	48.8	65.2	80.6
Calculated:	$\dot{m}c_p\Delta T$	(W)	114	111	100
Determined from balance:	$Q_{\text{HEX, cooling}}$	(W)	-89	-84	-72
HEX Bottom					
Derived (table 4.9):	$Q_{\text{Insulation}}$	(W)	-14.2	-15.1	-15.5
Known:	ΔT	(^{o}C)	29.1	35.7	37.6
Calculated:	$\dot{m}c_p\Delta T$	(W)	-68	-60	-46
Determined from balance:	$Q_{\text{HEX, heating}}$	(W)	82	75	62
Condenser Section					
Calculated (eq. 4.4):	Q_{Latent}	(W)	7	8	10
Known:	ΔT	(^{o}C)	40.0	41.8	40.2
Calculated:	$\dot{m}c_p\Delta T$	(W)	93	71	50
Determined from balance:	$Q_{\text{Condenser}}$	(W)	-104	-81	-63

4.4 Heat exchanger performance

The heat exchanger performance can be analyzed in different ways:

1. The value $Q_{\text{HEX, heating}}$, as can be seen in table 4.10, shows the heating duty of the heat exchanger. This value becomes more comparable between situations when dividing it by the total heat input to determine what fraction of heating is achieved by the heat exchanger.

2. The difference between the heating and cooling duty of the heat exchanger indicates the amount of heat lost in the heat pipes.
3. The temperature gradients over the top and bottom of the heat exchanger show how much the flow is cooled and heated in the heat exchanger. These should be as high as possible.

4.4.1 Relative heat transfer evaluation

The heating duty of the heat pipes is determined with the mass flow rate and the temperature gradient over the bottom of the heat exchanger section, see section 4.3. A useful performance indicator for the heat exchanger performance is the heating of the heat exchanger relative to the total heating of the flow in the heating side of the system. This is given by:

$$\xi_{\text{HEX}} = \frac{Q_{\text{HEX}}}{\sum Q_{\text{in}}} = \frac{Q_{\text{HEX, heating}}}{Q_{\text{HEX, heating}} + Q_{\text{Heaters}} + Q_{\text{Reaction}}} \tag{4.5}$$

Where a higher value of ξ_{HEX} denotes a better heat transfer performance. If autothermal operation is achieved, the heaters will not need to apply heat, and most of the heat will come from the heat exchanger. The heat of reaction is only produced when reaction occurs, and this does not happen if the temperature is not high enough. An ideal (autothermal) value for ξ_{HEX} can be calculated with a few assumptions:

- Reactor temperature of 230^{o}C: this is assumed to be an ideal reaction temperature at 50 bars, will need to be verified.
- ΔT over the heat exchange section of 160^{o}C
- ΔT over the condenser of 20^{o}C: flow enters the condenser at 70^{o}C and leaves at 50^{o}C. This guarantees high condensation rates and high efficiency.
- No losses in the heat exchanger except for the 20^{o}C temperature gradient between the top and bottom of the system.
- 50W losses through the insulation: this is assumed to be possible with better insulation.

These assumptions are also used to design an autothermal reactor in COCO in chapter 5. Assuming these idealized conditions,

$$\xi_{\text{HEX,ideal}} = \frac{\dot{m} c_p \Delta T_{\text{HEX}}}{\dot{m} c_p \Delta T_{\text{total}} + Q_{\text{Insulation}}} \tag{4.6}$$

With these assumption, the value for $\xi_{\text{HEX,ideal}}$ is only dependent on the mass flow rate. Therefore, a different value for $\xi_{\text{HEX,ideal}}$ is used to compare it to the value of ξ_{HEX} for the three reactor orientations. The heat inputs and the resulting values for ξ are found in table 4.11.

Table 4.11: Heater input, HEX heat transfer and a ratio of the two for the three reactor orientations.

	Property		Base Case	10^o Tilt	20^o Tilt
Calculated (eq. 3.9):	$\dot{m}$	(g/s)	0.78	0.57	0.41
Known:	Q_{Heater}	(W)	161	143	125
From table 4.10:	$Q_{\text{HEX, heating}}$	(W)	82	76	62
Known:	Q_{Reaction}	(W)	3.69	4.49	5.80
Calculated (eq. 4.5):	ξ_{HEX}		0.333	0.339	0.323
Calculated (eq. 4.6):	$\xi_{\text{HEX,ideal}}$		0.794	0.764	0.726
Calculated:	$\xi_{\text{HEX}}/\xi_{\text{HEX,ideal}}$	(%)	42	44	44

It is interesting to see that the value for ξ_{HEX} is barely influenced by the different mass flow rates and heat flows. A lower mass flow rate requires less heater input, though it also reduces the heating capacity of the heat exchanger due to the heat pipe performance, which is analyzed in section 4.4.3. These two effects seem to be somewhat balanced.

4.4.2 Heat exchanger heating and cooling

With the energy balance, separate values are determined for the heating and cooling duty of the heat exchanger. See section 4.3 for more information on the energy balance. The difference between the heating and cooling duty shows the amount of heat lost in the heat pipe due to conduction. A portion of the heat is transferred to the heat pipe shell instead of the condenser zone of the heat pipe. The heat is then conducted through the copper, which is very inefficient due to the small cross-sectional area. The heat is primarily lost into the insulation. The difference between the heating and cooling duty of the heat exchanger is the amount of heat lost by this effect. The relevant values are shown in table 4.12.

Table 4.12: Cooling and heating duties of the heat exchanger for the three different reaction orientations and the associated losses, along with the temperature gradients. The heating duty divided by the mass flow rate is given as an extra useful comparison.

	Property		Base Case	10^o Tilt	20^o Tilt
From table 4.10:	$Q_{\text{HEX, cooling}}$	(W)	89	84	72
From table 4.10:	$Q_{\text{HEX, heating}}$	(W)	82	76	62
Calculated:	ΔQ_{HEX}	(W)	7	8	10
Known:	$\Delta T_{\text{HEX, cooling}}$	(^{o}C)	48.8	65.2	80.6
Known:	$\Delta T_{\text{HEX, heating}}$	(^{o}C)	29.1	35.7	37.6
Calculated (eq. 3.9):	$\dot{m}$	(g/s)	0.78	0.57	0.41
Calculated:	$Q_{\text{HEX, heating}}/\dot{m}$	(J/g)	105	134	150

The heat exchanger losses are increasing, despite the heat flows reducing. However, the temperature gradients associated with cooling and heating are increasing significantly. Due to the lower mass flow rates, the flow has more time to exchange heat, there is more heat available per unit of mass. This correlation can be seen in table 4.12 and in figure 4.5.

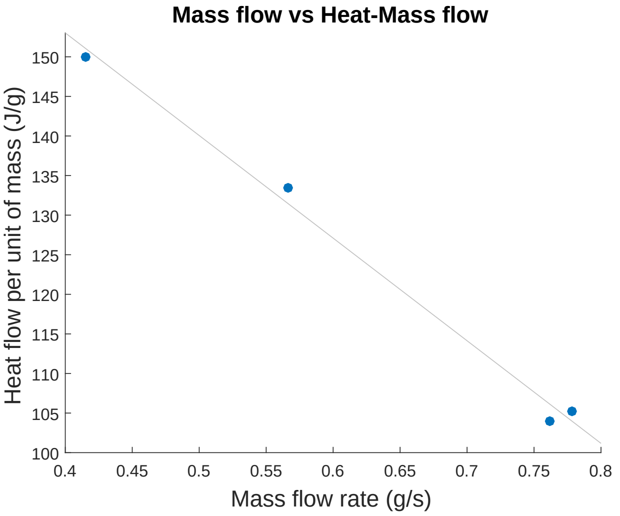

Figure 4.5: Mass flow rate and heat (HEX heating) flow per unit of mass correlated for several experiments.

4.4.3 Heat pipe temperatures and performance

The increasing heat pipe losses and lower heat flow can be explained by the temperatures in the system. The temperatures at the higher tilt orientations are higher, therefore the capillary limit is lower and the losses are larger. Another way to display this behaviour is by comparing the temperature gradient per heat pipe with the top temperature of each heat pipe. This is shown in figure 4.6.

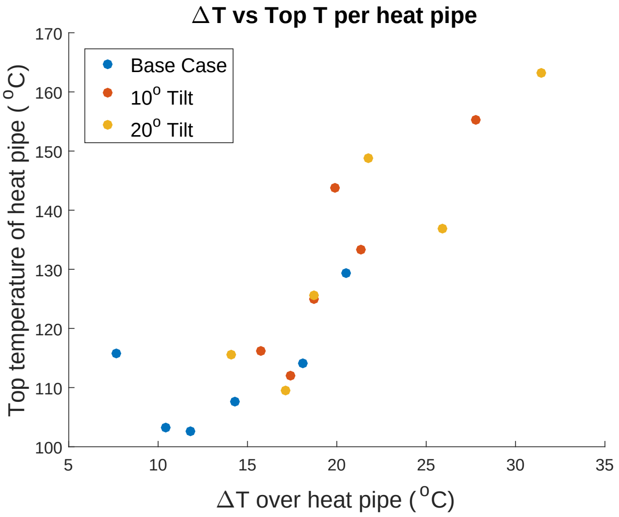

Figure 4.6: Heat pipe performance displayed by the temperature difference per heat pipe and the top temperature per heat pipe for each individual heat pipe for the three reactor orientations.

The figure shows that the heat pipe performance is correlated with the heat pipe operating temperature. This can be interpreted as a result of the capillary limit, which has a stronger effect at higher temperatures. The capillary limit seems to have an effect on heat pipe performance at relatively low temperatures. The porosity of the wick is likely lower than assumed in the calculations in section 3.2.1.

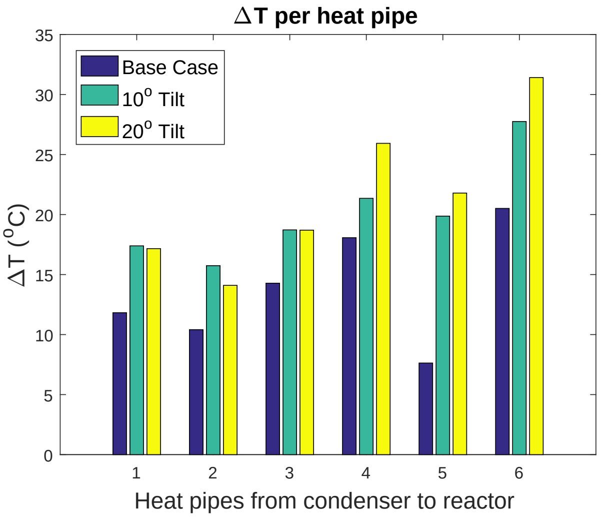

Figure 4.7: Temperature difference per heat pipe with its position in the system for the three different reactor orientations.

The temperature difference over the heat pipes along with their position is shown in figure 4.7. Heat pipes 1-3 have larger fin spacing at the top of the heat exchanger than heat pipes 4-6. This is not reflected in the performance. An interpretation of this observation is that the influence of temperature on the heat pipe capillary limit is more limiting to the heat exchanger performance than the difference in the fin structure surface area.

Another observation is that some heat pipes are operating more effectively than others (most notably heat pipe 2 and 5). This is most likely due to the method of production. As the fins are attached by hand, it is possible that certain fins have better contact with the supports than others. Also, there is thermal paste between the heat pipes and supports, perhaps the paste is more uniformly spread in certain supports. In any case, this result shows that the installation method of the heat components is flawed.

Furthermore, it can be seen that heat pipes 1 and 2 are operating slightly better for the 20^o tilt orientation than the 10^o tilt orientation. This is linked to a lower top temperature, as can be seen in the raw data in table 4.13, and can also be seen in figure 4.6. The temperature is lower due to the lower mass flow rate, which results in a more effective heat exchanger.

Table 4.13: Experimental steady state temperature sensor data for the heat pipes in ^{o}C.

Sensor	Base Case	10^o Tilt	20^o Tilt
Top 1	102.6	111.96	109.61
Top 2	103.21	116.25	115.67
Top 3	107.67	125.06	125.52
Top 4	114.16	133.34	136.84
Top 5	115.78	143.79	148.84
Top 6	129.41	155.29	163.25
Bottom 1	90.78	94.57	92.45
Bottom 2	92.8	100.51	101.57
Bottom 3	93.39	106.34	106.82
Bottom 4	96.09	111.99	110.91
Bottom 5	108.15	123.92	127.05
Bottom 6	108.9	127.54	131.84

4.4.4 Heat exchanger performance discussion

The value of ξ_{HEX} is useful as it gives an indication of the heat exchanger performance in the whole picture of flow heating. Also, it can be compared to the results of Basarkar in section 4.6. However, it gives the misconception that heat exchanger performance is roughly the same for the three reactor orientations, which is not the case when comparing other relevant characteristics.

Another misleading result is the absolute heating and cooling duty of the heat exchanger. This is greatly influenced by the mass flow rate and is therefore higher for the situation with the higher mass flow rate. When dividing this value by the mass flow rate to get the heat flow in J/g, it is clear that more heat is transferred per gram of flow for the lower mass flow rates. This is likely due to the fact that the fin structure was designed for a mass flow rate of 0.1 g/s, and has a too low surface area for the high flow rates measured in the system.

Though a lower mass flow rate improves fin performance, there are more losses in the heat pipes. This is likely related to the capillary limit, which becomes worse at higher temperatures due to lower surface tension in the working fluid of the heat pipe. See section 2.6.2 for more information on the heat pipe limits. The capillary limit seems to develop at lower temperatures than initially expected, likely due to a lower wick porosity than assumed in the calculations. See figure 3.6 for a visual representation of the effect of wick porosity on the capillary limit.

This behaviour is clearly visible by correlating the temperature gradient and the top temperature for each heat pipe, see figure 4.6. A higher temperature gradient implies more losses, and thus the higher top temperatures in the heat exchanger result in more losses.

4.5 Reactor flow homogeneity

A probable explanation for the strong correlation between STY and mass flow rate, shown in figure 4.2a, is that the temperature profile of the flow through the reactor is not homogeneous. A lower mass flow rate would mean more time for the temperature to dissipate through the flow and more flow to reach the reaction temperature.

4.5.1 Modelling of the equivalent reacting flow

A model is built in COCO, based on previous modelling work of Basarkar and Gutierrez [13, 64]. The model contains several points at which experimental data can be entered, such as the temperatures of the in and outlets of the condenser and reactor. There is a flash operation to remove the liquids from the gases. A purge and compressor are added for numerical stability and have a negligible influence on the results. See figure 4.8 for the model flowchart.

The homogeneity of the temperature profile in the reactor is modelled by equating the real temperature profile with a block profile, in which one part of the flow is 230^oC and reacting, whereas the other is not. This is shown graphically in figure 4.9. Simulating the flow with this profile will return the amount of flow reacting equivalent to a reaction at 230^oC. 230^oC is chosen as the equivalent temperature as the resulting reactor characteristics in the simulation are a closer match with experimental data than when simulating a lower temperature.

The bypass in the COCO model represents the flow that does not reach reaction temperature due to the non-homogeneous temperature profile. The model is used as follows:

1. Enter experimental data: methanol/water outlet flow (Methanol Water/Fresh Feed), reactor inlet temperature (HEX Bottom), condenser inlet temperature (HEX Top), condenser outlet temperature (Condenser), heater duty (Bypass & Reacting).

2. Vary: Fraction of flow going to bypass and reactor (Splitter), adjust the corresponding reaction diameter (Reaction).

3. Match with experimental data: Mass flow rate, reactor outlet temperature (Reactor Out).

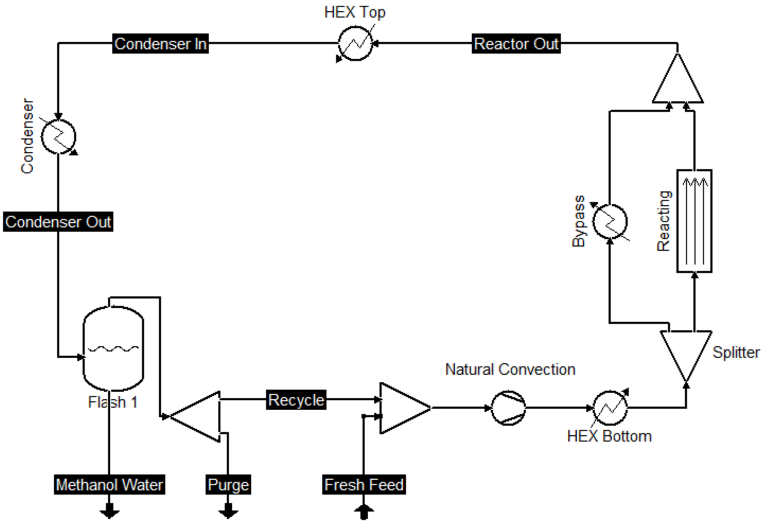

Figure 4.8: Flow chart of the COCO model used for the simulations. Note the splitter at the right side of the model before the reactor.

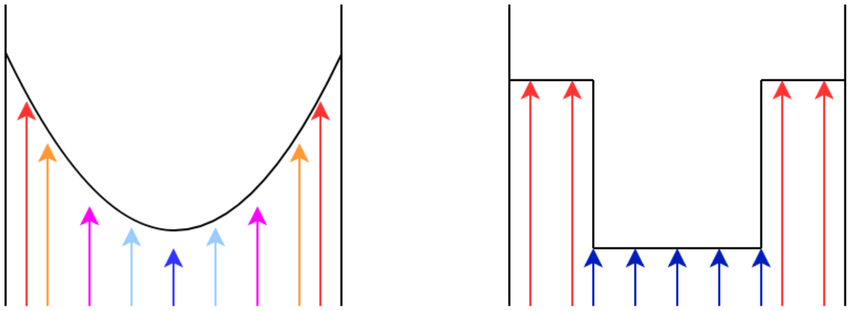

Figure 4.9: Diagram representing a non-homogeneous temperature profile in a flow (left), and the method of splitting this profile into a equivalent reacting flow and a non-reacting flow (right). This approach is used in the COCO simulation.

4.5.2 Center temperature and simulation results

The simulation is done for the three reactor orientations. Alongside the simulations, calculations are made to find the center temperature of the reactor, using a heat transfer resistance model, see figure 4.10. This model takes into account conduction through the copper, stainless steel and the catalyst, as well as convection through the catalyst. The model does not take into account radial mixing, which is assumed to be low due to the high mass flow rate. The effective thermal conductivity is found with experimental data and correlations given by [71] and [72], respectively. The model is solved with equation 4.7. The results of the simulations and calculations are given in table 4.15.

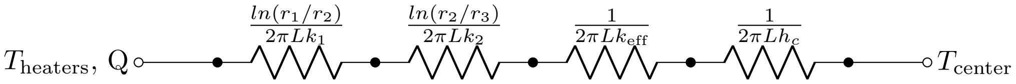
T_{heaters}, Q
$\frac{ln(r_1/r_2)}{2\pi L k_1}$
$\frac{ln(r_2/r_3)}{2\pi L k_2}$
$\frac{1}{2\pi L k_{\text{eff}}}$
$\frac{1}{2\pi L h_c}$
T_{center}

Figure 4.10: Heat transfer resistance model, where r_1, r_2 and r_3 denote the radii of copper tube that the heaters are attached to, and the inner and outer radii of the stainless steel reactor tube, respectively. k_1 and k_2 are the thermal conductivities of copper and stainless steel, k_{eff} is the effective thermal conductivity of the catalyst, determined with [71] and [72]. The values are given in table 4.14.

$$T_{\text{center}} = T_{\text{heaters}} - (Q_{\text{heaters}} - Q_{\text{insulation}})\frac{1}{2\pi L}\left(\frac{ln(r_1/r_2)}{k_1} + \frac{ln(r_2/r_3)}{k_2} + \frac{1}{h_c} + \frac{1}{k_{\text{eff}}}\right) \tag{4.7}$$

Table 4.14: Values used to find the catalyst bed center temperature with equation 4.7.

	Property	Value
Known:	r_1 (mm)	20.9
Known:	r_2 (mm)	19.4
Known:	r_3 (mm)	17.4
From [62]:	k_1 ($\text{Wm}^{-1}\text{K}^{-1}$)	371
From [62]:	k_2 ($\text{Wm}^{-1}\text{K}^{-1}$)	16.3
From [71] and [72]:	k_{eff} ($\text{Wm}^{-1}\text{K}^{-1}$)	221
Calculated (eq. 3.3):	h_c ($\text{Wm}^{-2}\text{K}^{-1}$)	105

The results in table 4.15 show that a only a small equivalent portion of the flow is actually reacting fully (at an equivalent of 230^{o}C), and that decreasing the mass flow rate increases the size of this portion. The calculated center temperature is in line with the simulation findings. An interesting result is the mass flow rate difference with the experimental results. This is likely due to pressure drop in the channels and over the heat exchanger fins, which is not taken into account in COCO.

Table 4.15: Simulation and calculation results for a representation of the fraction of the flow not hot enough to react, visually shown in figure 4.9. The difference with the experimental data is shown in brackets.

Property	Base Case	10^o Tilt	20^o Tilt
Simulation			
230^{o}C equivalent reacting flow (fraction)	0.085	0.145	0.210
$T_{reactor,out}$ (^{o}C)	158 (+1)	187 (+3)	198 (+1)
$\dot{m}$ (g/s)	1.0 (+0.22)	0.73 (+0.16)	0.55 (+0.14)
Methanol production (g/h)	10 (+0)	12.3 (+0)	15.7 (+0)
Calculation			
Center Temperature (^{o}C)	98	121	145

4.6 Performance comparison with previous work

The current reactor performance can be compared to the results of Basarkar [13] and Brilman [33]. Several characteristics are laid side by side in table 4.16.

Table 4.16: Comparison of reactor performance characteristics of Basarkar, Brilman and the current reactor. ^{*1} Catalyst bed outlet temperature. ^{*2} The mass flow rate of Basarkar is an estimate and not experimentally validated. ^{*3} Condenser outlet temperature.

Property	Basarkar [13]	Brilman [33]	Current Reactor (20^o Tilt)
Heater Temperature (^{o}C)	228	210^{*1}	242
Productivity (g MeOH/h)	8.6	15.5	15.7
STY (mmol MeOH/gcat/h)	6.76	6.4	4.10
$\dot{m}$ (g/s)	0.025^{*2}	-	0.41
η_{energy} (%)	37.5	20.0	36.5
ξ_{HEX}	0.140	0	0.323
Active condenser cooling (fan)	Yes	Yes	No
Condenser Temperature (^{o}C)	65	85	76^{*3}
Carbon Conversion (%)	99.22	99.5	99.39
Methanol Purity (mol%)	-	47.5±0.6	49±1

There are some distinct differences in reactor performance. Although absolute productivity is higher, the space time yield of the current reactor is currently lower than the others. However, it has increased by 58% in two increments of tilt, and from the correlation in figure 4.2a it is expected that STY can be further improved by reducing the mass flow rate.

There is a significant difference in reactor temperatures, though they are measured differently. First of all, Brilman mentions only the outlet temperature of the catalyst bed. In the current reactor, there is a large difference in catalyst bed outlet temperature and heater temperature due to the high mass flow rate. That is also why it requires a relatively high heater temperature as compared to Basarkar, who has a relatively low mass flow rate. Therefore, the ”heater temperature” is difficult to compare.

The energy efficiency is lower than that of Basarkar, whereas the heat exchanger is working over 230% more effectively, despite having an over 1600% higher mass flow rate. This is illustrated by the fact that Basarkar required a fan to cool his condenser, which is not taken into account in the energy efficiency calculation. Brilman had no heat exchanger and thus has a low energy efficiency and also required a fan. It is expected that the energy efficiency of the current reactor can be improved relatively easily by reducing the mass flow rate (see the correlation in figure 4.2b) and increasing the heat exchanger capacity (for example with more heat pipes and heat transfer surface area).

The carbon conversion of the three reactors is closely matched and is related to the condenser temperature. A lower temperature allows more CO_2 to dissolve into the water, which is released after removing the liquids. This agrees with the measured carbon conversion and condenser temperatures of the three reactors.

Chapter 5

Design of an optimal reactor

The results from the reactor paint a clear picture of what is happening in the reactor right now. All aspects of reactor performance are currently limited by the mass flow rate. This chapter contains simulations and calculations based on assumptions that the mass flow rate is not limiting the performance of other systems such as the heat exchanger. This allows for a more hypothetical, though nonetheless useful analysis of possible future performance and investment limitations.

5.1 Autothermal calculations based on an industrial space time yield

Though the reactor is far from autothermal, it is possible to theorize a scenario in which autothermal operation is achieved. With the same assumptions as used in section 4.4 to determine $\xi_{\mathrm{HEX,ideal}}$ and an extra assumption that the STY will approach the industrial values of around 20 mmol/gcat/h, three scenarios are laid out for three different mass flow rates. These scenarios are shown in table 5.1.

Table 5.1: Three highly optimized scenarios for autothermal operation with different mass flow rates. The assumptions are: no losses in the heat exchanger, 160^{o}C temperature drop over the heat exchanger, 20^{o}C temperature drop over the condenser, 50W insulation losses and STY of 20 mmol MeOH/gcat/h.

Property		Scenario 1	Scenario 2	Scenario 3
$\dot{m}$	(g/s)	1	0.5	0.1
$Q_{\mathrm{insulation}}$	(W)	50	50	50
Q_{HEX}	(W)	480	240	48
Q_{Reaction}	(W)	110	80	56
STY	(mmol MeOH/gcat/h)	20	20	20
Catalyst loading	(g)	465	338	237
Methanol productivity	(g/h)	298	217	152
ZEF systems productivity equivalent		11.9	8.7	6.1

What is interesting to note is that the (required) reaction heat becomes larger compared to the heat exchanger duty with decreasing the mass flow rate. This is due to the large temperature gradient over the heat exchanger. A higher mass flow rate increases heat exchanger requirements more than reaction heat requirements. The productivity relative to the heat exchanger duty therefore increases. The productivity for the 1 g/s scenario is less than 2 times higher than the 0.1 g/s scenario, while the heat exchanger duty (and size) is 10 times higher. This means that a 1 g/s system requires over 5 times more heat exchanger capacity than a 0.1 g/s system for the same productivity. This is a factor to take into account when optimizing the system for capital expenditure, though that is out of the scope of this project.

5.2 Reaction kinetics and catalyst bed length simulation

An important characteristic of the reactor performance is the reactor kinetics as a function of the catalyst bed length. This cannot be observed in the experimental setup, though it can be simulated. There are many factors that can influence the results of these simulations. Therefore, a set of conditions is chosen as a starting point, from which variations are made for comparison. The simulations contain a perfect heat exchanger, which means flow enters the reactor (homogeneously) at 230^{o}C, and leaves the condenser at 50^{o}C. The reactor bed is initially the same diameter as in the experimental setup.

For the first simulation, methanol productivity is equal to the productivity of the experimental 20^o tilt results: roughly 25 g/h of methanol/water mixture. The productivity is increased in such a manner that the mass flow rate in the system is 0.5 g/s. The simulations are then repeated for a larger catalyst bed diameter.

The first two simulations show that the reaction kinetics require a long catalyst bed to achieve steady state, see figure 5.1. This means more passes are required to convert the gases into methanol when using a shorter catalyst bed. This lowers the energy efficiency of the system, as each pass goes through cooling and heating. The results of these simulations demonstrate why there is such a low conversion per pass, as found in section 4.2.2.

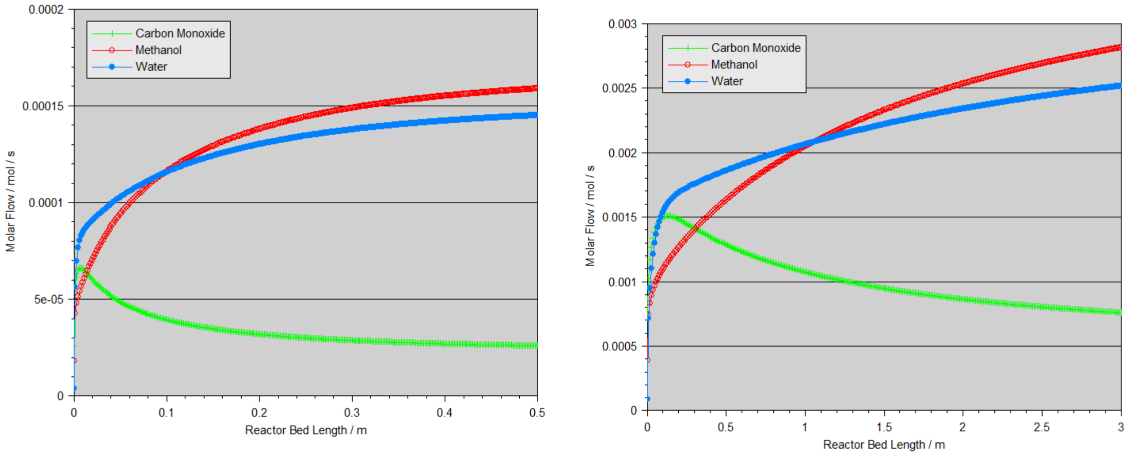

(a) Productivity: 25 g/h (Experimental), $\dot{m}$: 0.022 g/s.

(b) Productivity: 440 g/h, $\dot{m}$: 0.5 g/s.

Figure 5.1: Reactor kinetics vs. catalyst bed length simulations for approximate experimental values of productivity and mass flow rate, respectively.

One possible solution to this kinetic limitation is to increase the catalyst bed diameter. The simulations from figures 5.1a and 5.1b are repeated, but with a catalyst bed diameter of 70 mm instead of 35 mm. The resulting reaction kinetics as a function of the bed length are shown in figures 5.2a and 5.2b.

The mass flow rate is the same, whereas the catalyst bed length required to reach steady state reaction kinetics has been reduced by a factor of 4-5. From these results it can be concluded that to optimally use a short catalyst bed, a larger diameter is required. As a consequence, heating must be applied by convection, as conduction becomes less effective.

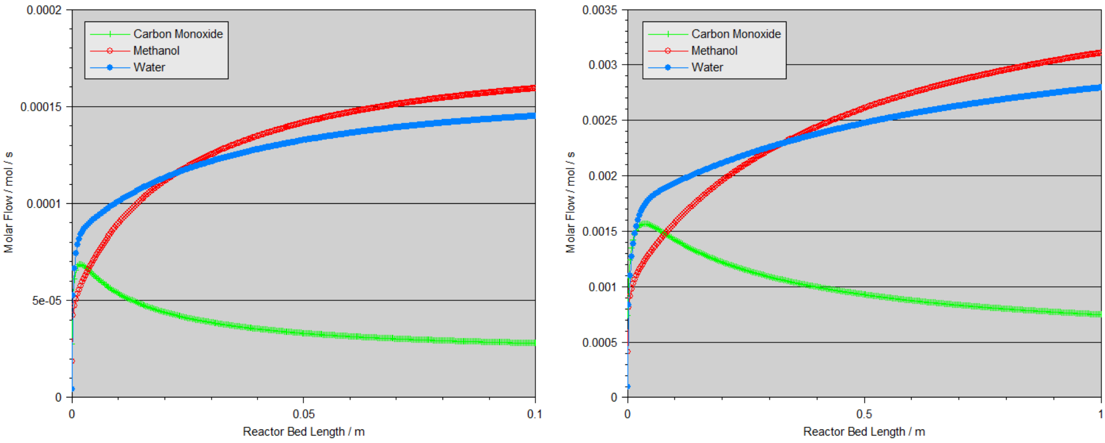

(a) Productivity: 25 g/h (Experimental), $\dot{m}$: 0.022 g/s, Catalyst bed diameter: 70 mm.

(b) Productivity: 490 g/h, $\dot{m}$: 0.5 g/s, Catalyst bed diameter: 70 mm.

Figure 5.2: Reactor kinetics vs. catalyst bed length simulations for approximate experimental values of productivity and mass flow rate, respectively. The catalyst bed diameter is increased from 35 to 70 mm.

5.3 Idealized autothermal reactor design

The current reactor is far from autothermal. The heat exchanger network is not working optimally and the productivity is too low to produce significant reaction heat. In this section, a simulation is executed to find the necessary parameters to reach autothermal operation.

5.3.1 Assumptions and boundary conditions

To start, a set of boundary conditions and assumptions is determined:

- There is a temperature gradient over the heat exchanger (top to bottom) of 20^{o}C.
- The reactor bed cannot be longer than 0.2m, due to reactor sizing and heat pipe length limitations.
- There is 50W of heat lost through the insulation.
- There is a homogeneous temperature and flow profile (plug flow).
- The system is operating at 50 bar, the reactor is operating at 230^{o}C, the condenser at 50^{o}C.
- Though the flow enters the reactor at 210^{o}C, the whole reactor is simulated as equivalent to isothermal at 230^{o}C. The reaction heat compensates for the required heating and insulation losses.
- The insulation losses can be fully compensated by the reaction heat (in terms of location of heat generation/loss). This essentially means that the insulation losses do not influence the heat exchanger duty/performance.
- The limit for $d_t/d_p = 20$, recommended by literature (see section 2.6.1). Therefore the maximum catalyst bed diameter is 0.12m.

5.3.2 Autothermal operation point

With this set of assumptions finding an optimum, autothermal operation point is relatively straightforward. The catalyst bed diameter and length should be maximized for optimal reaction kinetics, higher catalyst loading, and decreased mass flow rate.

The reaction heat is a function of productivity, which is adjusted in the simulation by the mass balance of changing the feed flow rate. The feed flow rate is adjusted until the reaction heat derived from the productivity is equal to insulation losses plus the required flow heating in the reactor. At this point, autothermal operation is achieved.

Parameters that give such an optimal, autothermal operation are given in table 5.2. The reactor kinetics as a function of the bed length is given in figure 5.3.

Table 5.2: Parameters and results of a simulation of a highly idealized autothermal reactor.

Parameter	Value
Methanol productivity (g/h)	205
$\dot{m}$ (g/s)	0.34
Bed diameter (m)	0.12
Bed length (m)	0.2
Catalyst loading (g)	2882
Results	
Q_{Reaction} (W)	76
$Q_{\text{Insulation}} + Q_{\text{Heating}}$ (W)	-76
Conversion per pass (%)	19
Q_{HEX} (W)	210
STY (mmol MeOH/gcat/h)	2.22
Δp (eq. 4.1) (Pa)	0.7

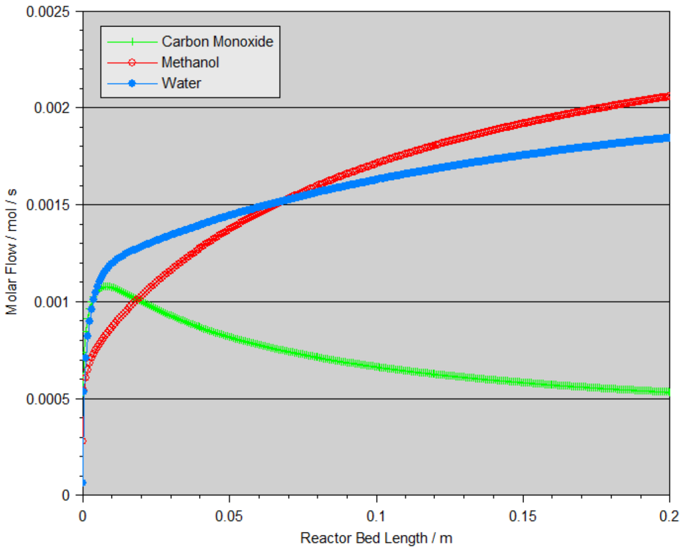

Figure 5.3: Reactor kinetics vs. catalyst bed length for an autothermal reactor simulation defined by the parameters in table 5.2.

5.3.3 Discussion

Though this simulation depends on several highly idealized assumptions, it does provide interesting insights.

First of all, this simulation demonstrates that a relatively low space time yield is beneficial for autothermal operation. This is due to the fact that the methanol conversion is slower when reaction kinetics are in steady state, which is necessary to achieve a high conversion per pass. To reach the steady state reaction kinetics, the residence time in the catalyst bed needs to be extended. This is achieved by increasing the catalyst diameter, resulting in a lower velocity at the same mass flow rate.

In reality, the STY is not a parameter that can be adjusted as in the simulation, but rather the residence time through the mass flow rate and the catalyst bed dimensions. This result also demonstrates that the assumptions made in the calculations of section 5.1 are false: a high space time yield is not possible with a high energy efficiency.

A crucial factor to achieve the autothermal operation point is the catalyst bed dimensioning. The simulation demonstrates the desirable effects of increasing the reactor bed diameter and length. A representation of the chosen catalyst bed dimensions, with the current channel dimensions and a high heat pipe density, is shown in figure 5.4.

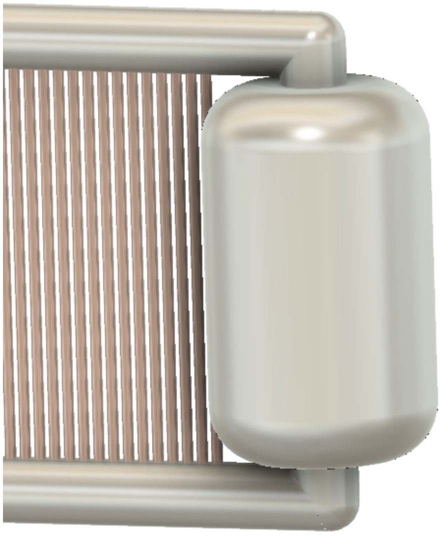

Figure 5.4: Visual representation of how the chosen catalyst bed dimensions could look like in practice.

The amount of heat pipes required to transfer 210W efficiently depends on the results of further research on heat pipe dimensions and porosity, though it undoubtedly a significantly higher amount than the current amount of six heat pipes.

The mass flow rate found in the simulation is slightly lower than in experimental work. Though there are some major differences in operation (such as the reactor bed dimensions), this result agrees with the finding that the experimental mass flow rate is too high. Due to the large catalyst bed diameter, the pressure drop over the catalyst bed is reduced to almost nothing. However, there will be pressure drop effects associated with expansion and reduction of diameter at the beginning and end of the catalyst bed, these are not taken into account now.

Chapter 6

Conclusions & Recommendations

At the start of this thesis, a set of research questions was formulated. To answer the questions, a reactor had to be designed and built. After a broad development phase, experimental work could validate design concepts and answer the research questions. This chapter contains the final conclusions and the following recommendations of this work.

6.1 Conclusions

In this section, the research questions are addressed with conclusions from experimental and simulation work.

1) How close can optimized heat integration and insulation bring the methanol synthesis reactor to autothermal operation?

There are four main factors that play a role in achieving or nearing autothermal operation: insulation losses, heat exchanger performance, mass flow rate, and reaction heat. The insulation losses have to be balanced by the reaction heat, as well as the required heating of the flow in the catalyst bed. This last value is minimized with an efficiently operating heat exchanger and by lowering the mass flow rate. A lower mass flow rate also reduces the difficulty of creating such an efficient heat exchanger.

As mentioned in section 4.4, the heat exchanger is currently operating at roughly 44% of the required relative duty to reach autothermal operation. This is calculated assuming the heat exchanger is operating without losses, the temperature drop over the condenser is 20^oC, and the insulation losses are 50W. However, there is much more reaction heat required to reach autothermal operation. Also, the heat exchanger is far from reaching the conditions used in the assumptions for autothermal operation conditions.

Simulations show that autothermal operation is hypothetically possible, though several idealized assumptions are necessary. The simulations do illustrate the requirements to approach autothermal operation. The conversion per pass needs to be high, which can be achieved by increasing the catalyst bed dimensions, in diameter and length.

Another interesting conclusion of the simulations is that the space time yield should be relatively low. This is a result of a high conversion per pass: when reaction kinetics are in steady state the conversion is slower. As the space time yield includes a time element, it decreases as reaction kinetics stabilize. This finding is a reminder that maximizing space time yield does not necessarily go hand in hand with maximizing energy efficiency.

The experimental mass flow rate is slightly higher than the simulation mass flow rate. This is an extra confirmation of the experimental conclusion that decreasing the mass flow rate is beneficial for energy efficiency.

1a) How much can the heat integration be improved as compared to the first ZEF prototype by using heat pipes?

Though the energy efficiency is slightly lower than the previous reactor (36.5% vs. 37.5%), the heat exchanger performance is much higher. The fraction of heat exchanger duty of the total heating duty has increased from 14% to 32%, an improvement of over 230%. The absolute heat exchanger heating duty has increased from 11.2W to 62W. It is expected from experimental correlations that the energy efficiency can be further increased by reducing the mass flow rate.

However, the heat pipes are operating above the determined capillary limit, and the flow is entering the reactor at just over 110^{o}C. If the heat load per heat pipe were to be lowered to a value well under the capillary limit, the network should work much more effectively. This can be achieved by adding more heat pipes and/or lowering the mass flow rate.

1b) What are the main sources of heat loss and how can these be minimized?

The main sources of heat loss are the insulation, the low conversion per pass and the heat exchanger performance. In the reactor orientation with the lowest mass flow rate, the insulation losses became the largest source of losses. The insulation losses are approximately two times those of Basarkar [13]. Basarkar measured an outside temperature of 28^{o}C, this was reduced to roughly 25^{o}C. However, the current insulation surface area is larger, and Basarkar measured a higher ambient temperature, and therefore calculated lower insulation losses. Insulation losses can be reduced by adding more insulation to the system or reducing the size of the system.

The temperature drop over the condenser is currently roughly 40^{o}C. With a better heat exchanger, this temperature drop could be reduced. The temperature of the fluid entering the condenser would be lower and require less cooling for condensation. Also, simulations indicate that an equivalent of 79% of the flow in the reactor is not reaching the reaction temperature. This results in a low conversion per pass, causing heat losses. If a more homogeneous temperature profile is achieved in the reactor, a higher conversion per pass can be realized, reducing these losses. Also, more reaction heat is produced per unit of mass, lowering heater requirements. The conversion per pass can also be improved with a larger catalyst bed diameter and length and a lower mass flow rate.

A less obvious source of heat losses is from the heat exchanger. This is because they are not necessarily losses but rather potential for improvement. To illustrate the potential, the experimental results are compared to a highly optimized situation. With an idealized heat exchanger, such as hypothesized in chapter 5, the flow enters the reactor at 210^{o}C. It would require the current 20^o tilt reactor roughly 120W of more heat exchange to achieve the same condition. There is thus a major potential for heat integration, by adding more heat pipes and/or reducing the mass flow. See table 5.1 for the influence of the mass flow rate on the required heat transfer for an ideal heat exchanger.

2) How can the natural circulation in the reactor be improved?

Perhaps the most significant difference between the current reactor and the previous ZEF reactor is the mass flow rate, with natural circulation as the driving force. It is clear that increasing the reactor dimensions greatly increases the effects of natural circulation. Other factors that influence natural circulation are the temperature gradient between reactor and condenser and the pressure drop over the catalyst bed. The temperature gradient between the reactor and the condenser is roughly the same as Basarkar, though the pressure drop over the reactor was not measured. It is reasonable to assume that there was a relatively high pressure drop due to the smaller channel dimensions. With the increased dimensions, the pressure drop is low and the natural circulation is more effective, causing higher flow rates.

3) What is the influence of tilting the reactor?

Tilting the reactor has a large influence on reactor performance. A 20^o tilt led to an increase in productivity of over 58% as compared to no tilt. This is correlated with the 46% decrease in mass flow rate, which is a limiting factor for productivity, primarily due to a non-homogeneous temperature distribution in the reactor.

It was anticipated that tilt would improve condensate flow. However, the case with no tilt seemed to have no problems with condensate reaching the outlet. Therefore it can be concluded that tilt is not necessary to improve condensate flow.

Tilting the reactor is naturally beneficial for heat pipe performance, as there is a smaller effect of gravity working against the capillary forces. However, this was not measurable as the effect of tilting on the mass flow has a much stronger effect on heat pipe performance. A lower mass flow rate allows the flow to transfer more heat to the heat pipes and vice versa.

4) What is the influence of increasing the catalyst amount on absolute productivity and on the space time yield?

The first experiments with 40g catalyst gave only trace amounts of methanol, whereas significant productivity was achieved with 120g catalyst. Again, this is correlated with the mass flow rate. The catalyst acts as a conductor of heat from the heaters to the flow. If the mass flow rate is too high, the flow will pass through the catalyst without reaching the required temperature for reaction to occur. Therefore, increasing the catalyst has a major influence on productivity in the current situation.

In idealized autothermal simulations, a high catalyst loading is required to achieve a high conversion per pass. Though the absolute productivity is relatively high, the space time yield is low. This is due to the effect of reaching steady state reaction kinetics on reaction speed. Therefore, a high conversion per pass will result in a slower reaction and thus relatively low space time yield. This could eventually result in a financial analysis of catalyst costs versus energy costs related to the energy efficiency of the reactor.

6.2 Recommendations

In this section, recommendations for reactor optimizations and future work are given in three main categories: heat integration, mass flow rate, and catalyst bed temperature distribution.

Heat integration

The heat exchanger should be redesigned with the current knowledge of the flow rates and other characteristics. The most important aspect is the amount of heat pipes. These should operate well under the capillary limit. For the current mass flow rate, roughly 200W of heat exchange is required for an ideal heat integration. This would require a large heat exchange section with many heat pipes and a more area effective design for the heat pipe placement. Placing heat pipes in pairs or even groups of four could provide better heat transfer performance, though this should be tested.

However, to find a more accurate indication of the capillary limit, more knowledge is required on the porosity of the wick. The porosity has a strong influence on the capillary limit, and the value differs in literature. It may be necessary to source higher quality heat pipes from a different supplier. In any case, it is clear that the heat pipe capillary limit is a major obstacle in reaching autothermal operation, and more in depth heat pipe research for the required conditions is necessary to make sensible decisions on further heat exchanger design.

Another way to significantly improve heat pipe performance is by shortening the heat pipes, which will raise the capillary limitations. The limiting factor in the current situation is the height of the system, which is primarily influenced by the large 90° Tri-Clamp bends. The reactor could be much shorter if the whole hot side, with bends and reactor bed, were shortened and ideally made from one piece. How this could look is shown in figure 6.1.

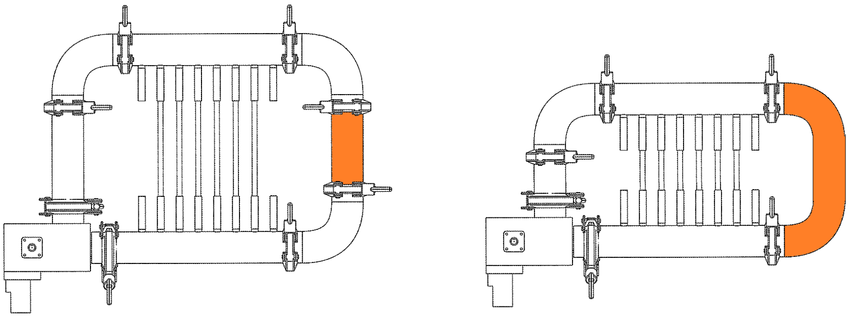

Figure 6.1: Representation of how the reactor height can be decreased by making the hot side from one piece. Left is the current reactor, right is a shortened reactor concept. The catalyst bed is highlighted, it does not have to decrease in size by the shortening. Note that the heaters are omitted, the shortened reactor concept would require a new heater design.

This could also prove to be an interesting study in the effects of reactor and condenser height on natural convection. Other expected effects are a smaller system size and less mass, resulting in less insulation losses and a quicker start-up time.

A different reactor design is presented in section 5.3.2. It is based on a simulation of an autothermal reactor. To reach autothermal operation, a high conversion per pass is essential. To achieve a high conversion per pass, the residence time of the flow in the catalyst bed should be increased to reach steady state reaction kinetics. To achieve this, the catalyst bed diameter should be increased, as well as the length. A lower mass flow rate would also be beneficial. The simulation work which demonstrates this effect should be tested in practice.

Mass flow rate

The mass flow rate is a reactor characteristic which is highly correlated with practically every other characteristic. A high mass flow rate has potential for high productivity, but it comes at a cost. A larger heat exchanger is required for a higher mass flow rate, and a long catalyst bed is needed to achieve homogeneous temperatures in the reactor. At the moment, reducing the mass flow increases productivity, reaction heat and heat exchanger performance. It would be interesting to continue reducing mass flow to find the optimum productivity and heat exchanger performance for the current setup. Simulations show that a hypothetical autothermal reactor could have a mass flow rate of 0.34 g/s, slightly lower than the current mass flow rate.

The author believes that if mass flow rate can be reduced while independently improving another characteristic its application should be tested. Three examples are:

1. Higher surface area structure in the non-condensing part of the heat exchanger. This will slightly slow the flow while reducing the amount of length needed per heat exchanger unit. This could be done with smaller fin spacing or a totally different structure such as a copper mesh.
2. Internal structure in the condenser. A higher surface area in the condenser will allow more fluids to condense while slowing down the flow. Also, this will prevent methanol and water to re-enter the reactor, therefore reducing heat loss. Such a structure could be designed similar to the 5mm spacing fin structures, adapted for the condenser length.
3. Increasing the catalyst bed dimensions. This is a key result of the autothermal reactor simulations. The increased catalyst volume will slow down the flow while improving conversion

rates. The space time yield will likely decrease. This is shown graphically in figure 5.4.

Catalyst bed temperature distribution

It is clear that much can be won with a homogeneous temperature in the catalyst bed. It would be very interesting to able to measure the temperature distribution in the catalyst bed and correlate it to the mass flow and the catalyst bed length. Along with simulation work, this would provide valuable insight into a reactor characteristic which is currently limiting the productivity and reaction heat.

A possible solution for the non-homogeneous flow temperature in the catalyst bed is to heat by convection instead of conduction. A heater setup could be designed to be connected to an internal heat exchange structure. Apart from the major advantages of a homogeneous temperature in the catalyst bed, less heat is lost by conduction through the steel tubes. How such a heater setup could look like is shown in figure 6.2.

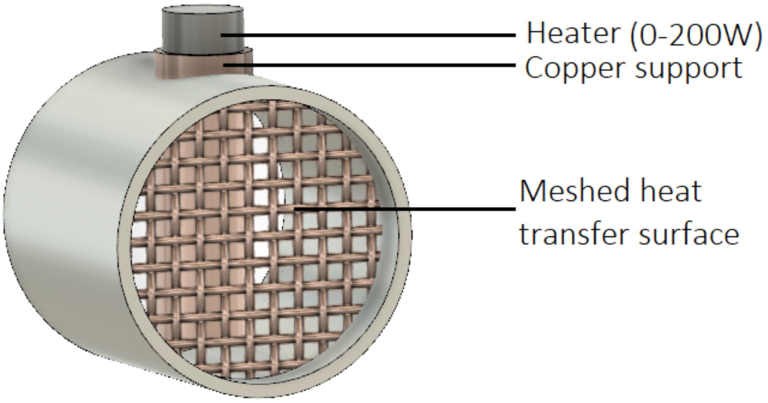

Figure 6.2: Visualization of how a convective heater with a meshed heat transfer surface could look like.

Appendix A

Heat pipe limitation constants

Table A.1: Constants used in the heat pipe limitation calculations in section 3.2.1.

Constant	Value	Unit	Definition
A_w	5.50e-6	m^2	Wick cross sectional area
d	63e-6	m	Copper powder diameter [56]
ϵ	0.45	-	Porosity [56]
g	9.81	ms^{-2}	Gravitational constant
k_{eff}	180	$Wm^{-1}K^{-1}$	Effective conductivity of vessel and wick
k_l	0.6	$Wm^{-1}K^{-1}$	Conductivity of the working fluid
k_w	400	$Wm^{-1}K^{-1}$	Conductivity of the wick material
λ	2.26e6	Jkg^{-1}	Latent heat of vaporization
l_{eff}	0.2652	m	Effective heat pipe length
l_t	0.3	m	Total heat pipe length
μ_l	1.15e-4	$kgm^{-1}s^{-1}$	Dynamic viscosity of the liquid
μ_v	1.15e-4	$kgm^{-1}s^{-1}$	Dynamic viscosity of the vapour
Ψ	75	deg	Angle of the heat pipe vs. the horizontal
r_{eff}	10e-6	m	Effective pore radius (Data sheet)
$r_{h,s}$	5e-6	m	Hydraulic radius
r_i	0.002	m	Vessel inner wall radius
r_n	10e-6	m	Nucleation radius [41]
r_v	0.001	m	Vapour core radius
ρ_l	1000	kgm^{-3}	Density of the liquid
ρ_v	0.44	kgm^{-3}	Density of the vapour (232 ^{o}C)
σ	0.0264	Nm^{-1}	Surface tension of the liquid (250 ^{o}C)
T_v	505.15	K	Temperature of the vapour
θ	37	deg	Contact angle of the liquid in the wick

Appendix B

Reactor parts and sizing

B.1 Main reactor parts

Part no.	Size	Description	Tri-Clamp Figure	Tri-Clamp Sizing
1	L = 100	Reactor pipe	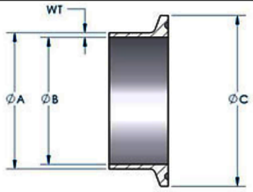	A = 38.1 B = 34.8 C = 50.5 WT = 1.73
2	L = 120	Condensate pipe		
3	L = 220	Cold HEX pipe		
4	L = 200	Hot HEX pipe	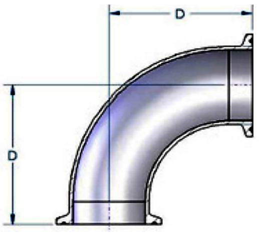	D = 69.9
5	See figure	Elbowpieces		
6	55x105x58	Cornerpiece		
7	$\varnothing$30x50	Fluid chamber		
8	See figure	SH Safety Clamp®	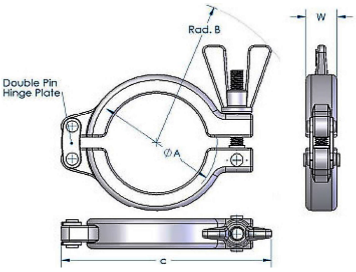	A = 50.5 B = 77 C = 102 W = 17
9	$\varnothing$6x200	Heat pipe		
10	$\varnothing$4-8.4x75	Heat pipe support		
11	50x50x60	Heater block		

Table B.1: Sizing of the reactor parts given in figure B.1. All sizes are in mm.

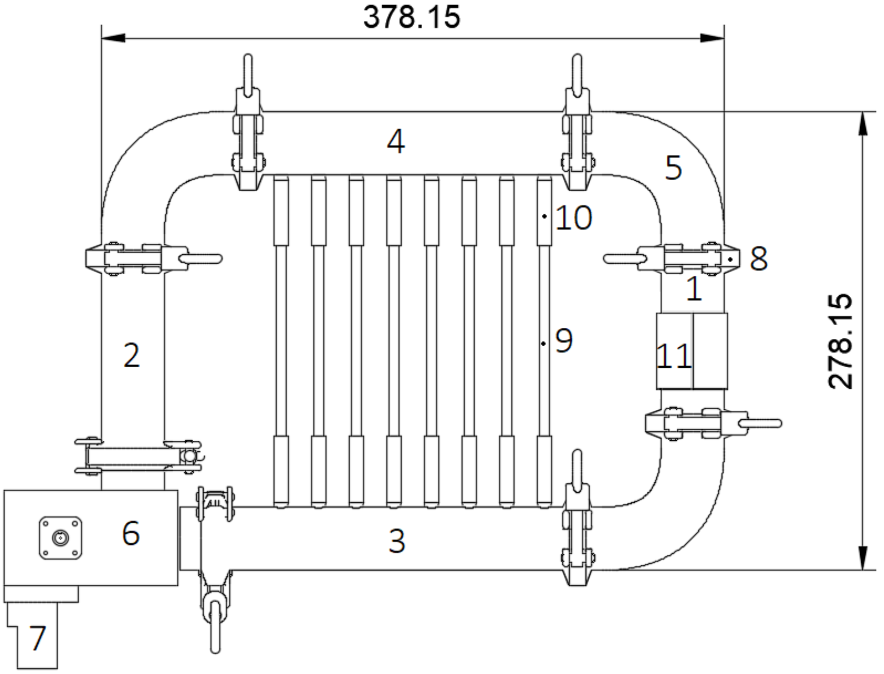
378.15
278.15
1
2
3
4
5
6
7
8
9
10
11

Figure B.1: Schematic of the reactor, the sizing of individual parts are given in table B.1.

B.2 Heat pipe support with fins

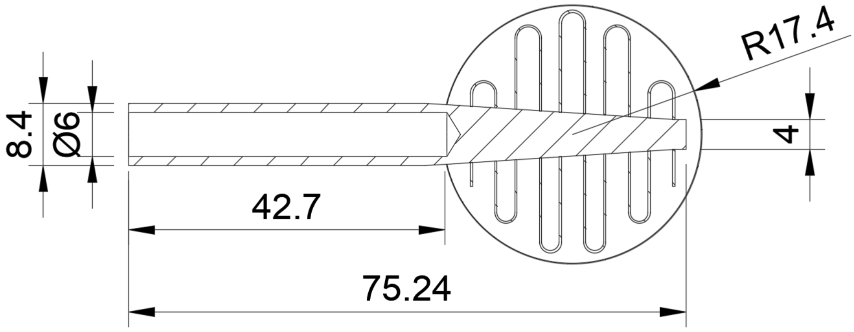
8.4
Ø6
R17.4
4
42.7
75.24

Figure B.2: Sizing of the conical heat pipe support, with fin structure.

B.3 Cornerpiece

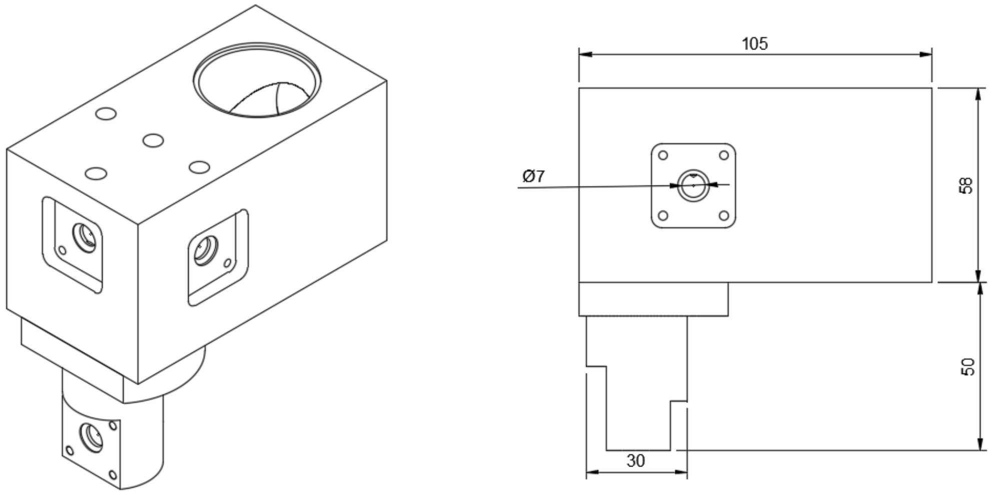

Figure B.3: Cornerpiece schematic, complete with liquid collection section, without solenoid valves or connection tubes. Several dimensions are given in mm. The width of the cornerpiece is 55 mm.

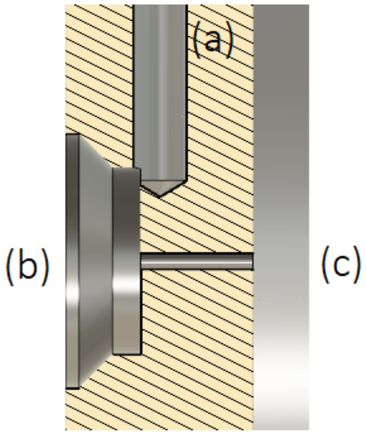

Figure B.4: Inlet design for a solenoid valve, where (a) is the inlet of 2 mm, (b) is the position of the solenoid valve and (c) is the inside of the reactor, connected by a 0.6 mm hole. The inlet valves are submitted to 50 bar pressure on both sides of the valve.

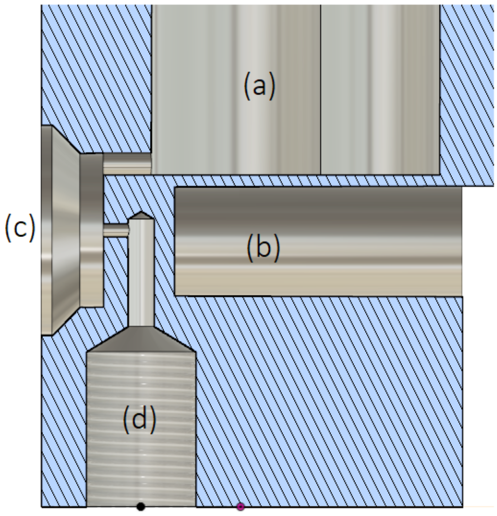

Figure B.5: Outlet design for a solenoid valve, in this case at the liquid outlet. (a) is the liquid collection chamber, which also contains a floating magnetic 'pill'. Its magnetic field is detected by a hall effect sensor located at (b). The solenoid valve is located at (c), with a 0.6 mm hole leading towared the outlet at (d), which is designed for a luer-lock outlet, a system which allows different kinds of syringes to be attached.

Appendix C

NTC Calibration

The temperature sensors used in the system are NTCs, or *Negative Temperature Coefficient* sensors. An NTC is essentially a resistor, whose resistance value is dependant on the temperature. The 'Negative' in NTC indicates that the resistance decreases with increasing temperature. The NTC is coupled with another, ordinary, resistor which functions as a voltage divider. For this system, a high resistance NTC of $100{\pm}1\% k\Omega$ was chosen, as this allows a larger temperature range to be measured, without the resistance becoming so low that a significant current will flow through the NTC. The '100 $k\Omega$' value of the NTC indicates the resistance of the NTC at 25^oC.

Calibration was initially attempted using the commonly used Steinhart-Hart Equation. The set of equations requires three temperature and corresponding resistance values, with which it will give a resistance-temperature correlation which can be used to measure other temperatures. Individual NTCs were calibrated in ice water, boiling water and at room temperature, accurately measured with a calibrated F252 High Precision Thermometer. However, temperature measurements proved to be extremely unreliable once the temperature was above 100^oC. Therefore, it was necessary to find a different calibration method.

The solution was to directly measure the voltage readings through Arduino, which is directly related to the NTC resistance through the following formula:

$$\text{NTC Voltage} = \frac{\text{Resistor Resistance}}{\text{NTC Resistance} + \text{Resistor Resistance}} \cdot \text{Arduino Voltage (5V)} \tag{C.1}$$

By measuring the temperature with the F252 High Precision Thermometer and the NTC voltage, a curve is plotted over a range of 20-240^oC. By applying a polynomial curve fit, an equation is found which gives a reliable and accurate temperature reading, within approximately 1-2% of the real temperature, as this is the accuracy of the individual NTCs and resistors. See figure C.1 for the plot, along with the most accurate fit of the Steinhart-Hart equation (the fit for the calibration with 0, 20 and 100^oC is much worse for higher temperatures than 100^oC).

It was initially chosen to use 100 $k\Omega$ resistors with the NTCs, as a high resistance ensures little current going through the NTCs. However, this means that the NTC voltage is 2.5 V at 25^oC, thus a large range of voltages are 'unused'. Therefore, high temperatures are on a steep slope on the voltage-temperature curve, which amplifies possible inaccuracies. By using a lower resistance resistor, this effect will be mitigated, though more current will run through the NTCs. It is found that the NTC resistance at 240^oC is approximately 500Ω. Coupled with a $5{\pm}1\% k\Omega$ resistor, the current through the NTC will be under 1 mA, which is an acceptable value. Therefore, the calibration was repeated with a 5 $k\Omega$ resistor. As expected, the curve is much less steep and occupies a broader voltage range, making it more accurate. The resulting curve and fit can be seen in figure C.2.

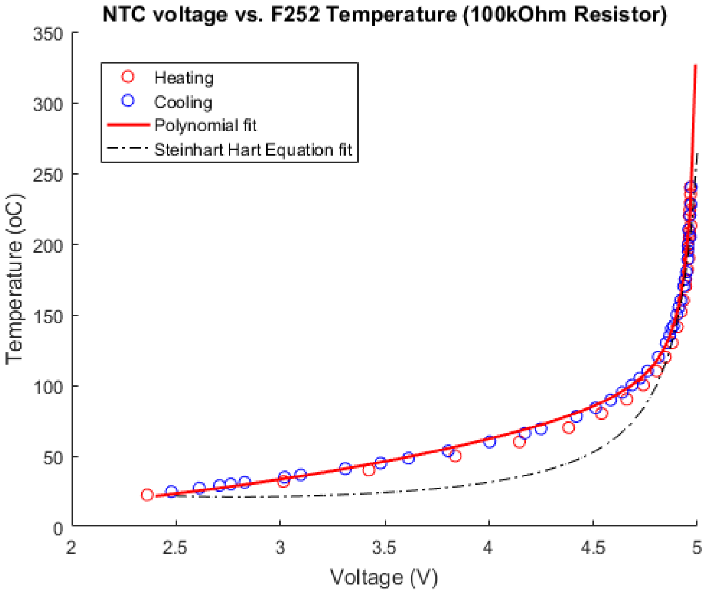

Figure C.1: 100 $k\Omega$ NTC voltage with 100 $k\Omega$ resistor plotted against the temperature reading of an F252 High Precision Thermometer. Heating and cooling are shown separately, as this indicates the possible measurement error. A rational polynomial function is used to fit the curve. The most accurate Steinhart-Hart Equation fit is also shown.

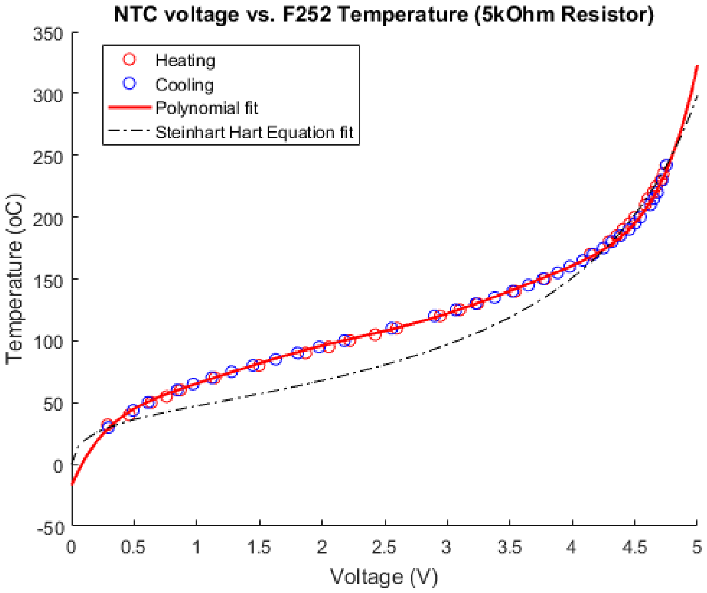

Figure C.2: 100 $k\Omega$ NTC voltage with 5 $k\Omega$ resistor plotted against the temperature reading of a F252 High Precision Thermometer. Heating and cooling are shown separately, as this indicates the possible measurement error. A polynomial function is used to fit the curve. The most accurate Steinhart-Hart Equation fit is also shown.

Appendix D

Heat pipe heat transfer correlation

To experimentally determine the flow of heat through the heat pipes an experimental setup is used to determine the correlation between the temperature difference over a heat pipe at a fixed supply of heat. The heat pipe is oriented vertically, with the condenser zone below the evaporator. The condenser is placed in a heat pipe support with fin structure, in the same way that the heat pipe is oriented in the reactor. The evaporator is placed in a tube similar to the heat pipe supports in the reactor, but with an extra hole for a heater element, of the same type as used in the reactor. The setup is shown in figure D.1

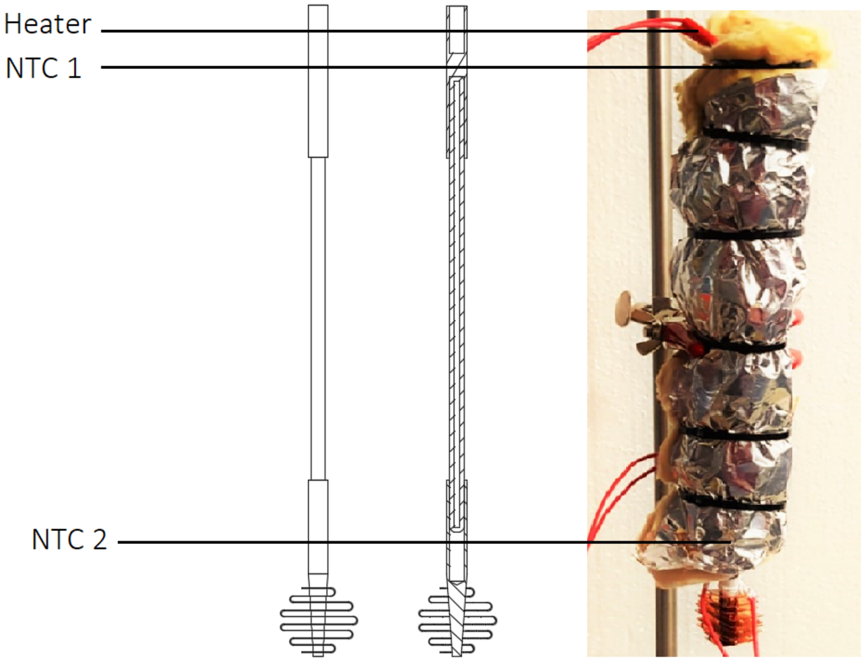

Figure D.1: Drawings and photograph of the test setup used to determine the heat pipe heat transfer correlation. The location of temperature sensors and heater are shown.

The results of the experiment are seen in figure D.2. A correlation is found in the form of $y = ax^b + c$. The formula is used to determine the heat transfer through the heat pipes in the reactor.

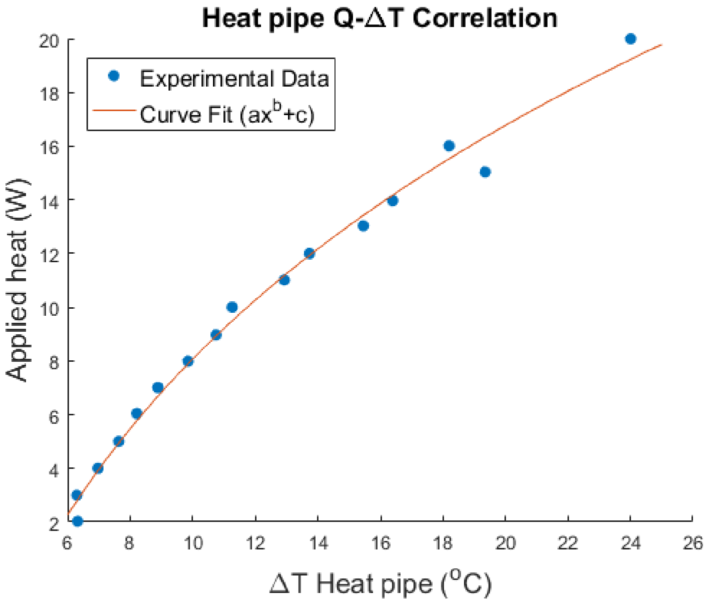

Figure D.2: Experimentally determined correlation between the temperature difference over a heat pipe and a fixed supply of heat. The heat pipe is oriented vertically, with the condenser below the evaporator.

Appendix E

Mass flow rate determination comparison

The mass flow rate can be calculated with two methods. One uses the accurately determined heat flows in the reactor section, the other uses the less accurate heat transfer correlation for the heat pipes, shown in figure D.2. To make an assumption of the insulation losses per section, the logarithmic mean temperature equation is used. The logarithmic mean temperature difference is given by:

$$\Delta T_{\text{LMTD}} = \frac{\Delta T_A - \Delta T_B}{\ln(\Delta T_A) - \ln(\Delta T_B)} \tag{E.1}$$

Where A and B are the temperatures of the in- and outlets of the section, and the Δ denotes the difference with the ambient temperature. The results of this equation and the found ratios are shown in table E.1.

Table E.1: Logarithmic mean temperature difference data and calculations over the three insulated sections, with temperature difference between the in- and outlets of the sections with the ambient temperature, measured to be 21.6^{o}C. The numbering of the temperature is from figure 3.15. The numbering of the experiments is explained in table E.2.

Property	Experiment 1	Experiment 2	Experiment 3	Experiment 4	Experiment 5
T_1	108.93	108.73	118.89	116.11	114.09
T_2	68.86	70.90	77.06	75.95	76.57
T_3	97.94	98.57	112.79	113.58	113.98
T_4	157.69	159.01	184.11	196.72	204.07
ΔT_{LMTD}					
Reactor	103.35	104.29	123.43	129.12	132.35
HEX Top	109.91	110.37	127.12	130.70	132.42
HEX Bot	60.64	62.11	71.85	71.52	72.06
$\Delta T_{\text{LMTD}}/\sum \Delta T_{\text{LMTD}}$					
Reactor	0.38	0.38	0.38	0.39	0.39
HEX Top	0.40	0.40	0.39	0.39	0.39
HEX Bot	0.22	0.22	0.22	0.22	0.21

The ratios are relatively close together for different experimental conditions. In following calculations it is assumed that 39% of the insulation losses is found each in the reactor and the top of the heat exchanger, and 22% leaves the bottom of the heat exchanger.

The mass flow rates are found with equations E.2 and E.3.

$$\dot{m}_{\text{reactor}} = \frac{Q_{\text{heaters}} + Q_{\text{reaction}} - 0.39Q_{\text{insulation}}}{c_p(T_{\text{reactor,out}} - T_{\text{reactor,in}})} \tag{E.2}$$

$$\dot{m}_{\text{HEX}} = \frac{Q_{\text{HEX}} + 0.39Q_{\text{insulation}}}{c_p(T_{\text{reactor,out}} - T_{\text{condenser,in}})} \tag{E.3}$$

The results of the two methods for several experimental runs are shown in table E.2.

Table E.2: Experimental values and results for two methods of determining the mass flow rate. One uses the heat inputs in the reactor, the other uses the heat transfer through the heat exchanger, determined with the correlation from figure D.2. The insulation losses are taken into account and are assumed to be 60W.

Experiment	Q_{heaters} (W)	Q_{reaction} (W)	Q_{HEX} (W)	$T_{\text{reactor,out}}$ (^{o}C)	$T_{\text{condenser,in}}$ (^{o}C)	$\dot{m}_{\text{reactor}}$ (g/s)	$\dot{m}_{\text{HEX}}$ (g/s)
1	160.7	3.69	68.5	157.7	108.9	0.78	0.64
2	162.5	3.45	73.0	159.0	108.7	0.76	0.67
3	142.8	4.48	100.1	184.1	118.9	0.57	0.65
4	125.0	5.80	104.1	196.7	116.1	0.41	0.55
5	137.0	6.38	103.3	204.1	114.1	0.41	0.51
Experimental conditions							
1	Base Case: 0^o tilt, 241^{o}C						
2	Base Case: 0^o tilt, 241^{o}C						
3	10^o tilt, 241^{o}C						
4	20^o tilt, 241^{o}C						
5	20^o tilt, 247^{o}C						

The mass flow rates found with equation E.2 follow a more logical trend than the mass flow rates found with equation E.3. Since the values used in the calculations are also more accurate, it is assumed that $\dot{m}_{\text{reactor}}$ is the more accurate value for the mass flow rate in the system.

E.1 HEX heat transfer determination method comparison

The heat transfer obtained from the heat pipe correlation is compared with the heat flow determined with the value for $\dot{m}_{\text{reactor}}$ in table E.3.

Table E.3: Heat exchanger cooling duty determined with the correlation from appendix D and with the mass flow rate over the reactor.

Experiment	Q_{HEX} (From correlation)	Q_{HEX} (From $\dot{m}_{\text{reactor}} c_p \Delta T$)
1	68.5	88.7
2	73.0	86.2
3	100.1	83.9
4	104.1	72.6
5	103.3	76.1

There is a large gap in most cases. As the value for m_{reactor} is assumed to be more accurate, it is concluded that the correlation found in section D is insufficiently accurate. This is likely due to the different conditions, such as the c_p of the fluid, which is roughly 100 times lower for ambient air than for the gas flow in the reactor. Also, the insulation is thicker is in the reactor than in the heat pipe test setup. The method for determining the heat pipe correlation should be more adjusted to the reactor conditions for it to gain accuracy.

Appendix F

Additional experimental results

F.1 Convective fluid heating

To attempt to heat the flow more effectively a heater was inserted into the empty heat pipe support before the reactor inlet (which was being used to measure fluid temperature, see section 3.6.1). This resulted in an increase in reactor outlet fluid temperature, though also a higher condenser temperature. The space time yield and energy efficiency were slightly lower than the base case, see table F.1. As this method of heating renders one of the fluid temperature sensors useless, this heating method is dismissed for now. This method of heating is likely more effective if more heat can be applied (now it was only 1 of the 8 heaters). Convective heating could eventually help create a more homogeneous fluid temperature through the reactor.

Table F.1: Data from the base case (242^{o}C, 120g catalyst, 50 bar) compared to the base case with one heater directly heating the flow through a heat pipe support with fins.

Property	Base Case	With Fluid Heater
STY (mmol MeOH/gcat/h)	2.61	2.46
Energy Efficiency (%)	23.9	22.7
Reactor Outlet Temperature (^{o}C)	159	167
Condenser Inlet Temperature (^{o}C)	109	118

F.2 Active condenser cooling

As the condenser temperature is higher than targeted, application of active condenser cooling with a computer fan operating at approximately 0.6W is tested. Condenser temperature is lowered 10-25^{o}C, depending on how close the fan is placed to the condenser. Due to the high mass flow rate, the reactor outlet fluid temperature also decreases by the same amount. STY and efficiency decrease as well. This shows that the reactor fluid temperature is more limiting to STY than condenser temperature at this time. Relevant measurements are shown in table F.2.

Table F.2: Data from the base case (242^{o}C, 120g catalyst, 50 bar) compared to the base case with a 0.6W in front of the condenser.

Property	Base Case	Base Case With Fan
STY (mmol MeOH/gcat/h)	2.61	1.83
Energy Efficiency (%)	23.9	15.7
Reactor Outlet Temperature (^{o}C)	159	136
Condenser Inlet Temperature (^{o}C)	109	88
Condenser Outlet Temperature (^{o}C)	69	46

F.3 Heater temperature increase

The heater temperature is set at 242^{o}C for the base case and the following experiments. With the 20^o tilt orientation, a heater temperature of 247^{o}C is tested. The results can be seen in table F.3.

Table F.3: Data from the 20^o tilt experiment (242^{o}C, 120g catalyst, 50 bar) compared to the same case but with 247^{o}C heater temperature.

Property	20^o Tilt + 242^{o}C	20^o Tilt + 247^{o}C
STY (mmol MeOH/gcat/h)	4.10	4.51
Energy Efficiency (%)	36.5	36.5
Heater Duty (W)	125	138
ξ_{HEX}	0.323	0.310
Mass Flow Rate (10^{-3} kg/s)	0.41	0.41
Reactor Outlet Temperature (^{o}C)	197	204
Condenser Inlet Temperature (^{o}C)	116	114
ΔT Top Heat Exchanger (^{o}C)	81	100
ΔT Bottom Heat Exchanger (^{o}C)	37.6	37.4

Increasing the temperature shows an increase in STY, though no increase in energy efficiency. The heat transfer performance indicator ξ_{HEX} decreases. This case is dismissed for now as it is close to the operating limit of PTFE, which is used in the seals, and also as electrical insulation on the temperature sensors. During the following reactor run, it was found that the heater control NTC was damaged, causing the reactor to overheat and melt the seals above and below the heaters. Therefore, 247^{o}C should not be used as operational temperature with the current setup.

Appendix G

Previous work extra calculations

Table G.1: Values used to calculate η_{energy} and ξ_{HEX} for the reactors of Basarkar, Brilman and the current reactor. *Characteristics indirectly calculated from Brilman's results.

Property	Basarkar [13]	Brilman [33]	Current Reactor
STY (mmol MeOH/gcat/h)	6.76	6.4	4.10
Catalyst loading (g)	40	76*	120
Heat content of methanol (LHV) (W)	54.4	86.9	87.9
Heat content of hydrogen (HHV) (W)	71.6	114.3	115.7
Q_{Heaters} (W)	64.84	320	125
η_{energy} (%)	37.5	20.0	36.5
Q_{HEX} (W)	11.1	0	62
Q_{Reaction} (W)	3.59	5.73*	5.80
ξ_{HEX}	0.140	0	0.323

The catalyst loading of Brilman's reactor is calculated using:

$$Loading = \frac{320[W] \cdot 3600[s]}{74 \cdot 10^{6} \frac{[J]}{[kg]} \cdot 32 \cdot 10^{-6} \frac{[kg]}{[mmol]} \cdot 6.4 \frac{[mmol]}{[gcat][h]}} = 76g \tag{G.1}$$

Where 74 MJ/kg is the energy input given in the report [33]. The reaction heat of Brilman's reactor is calculated using:

$$Q_{\text{Reaction}} = \frac{6.4 \frac{[mmol]}{[gcat][h]} \cdot 76[gcat] \cdot 42.47 \frac{[J]}{[mmol]}}{3600[s]} = 5.73W \tag{G.2}$$

Bibliography

[1] *Global land-ocean temperature index.* URL: `https://climate.nasa.gov/vital-signs/global-temperature/` (visited on Sept. 2018).

[2] *Atmospheric Carbon Dioxide Dry Air Mole Fractions from quasi-continuous measurements at Barrow, Alaska; Mauna Loa, Hawaii; American Samoa; and South Pole, 1973-2016.* URL: `https://www.esrl.noaa.gov/gmd/dv/data/` (visited on Sept. 2018).

[3] C. MacFarling Meure et al. "Law Dome CO_2, CH_4 and N_2O ice core records extended to 2000 years BP". In: *Geophysical Research Letters* 33.14 (2006).

[4] D. Lüthi et al. "High-resolution carbon dioxide concentration record 650,000–800,000 years before present". In: *Nature* 453.7193 (2008), p. 379.

[5] *Key World Energy Statistics 2017.* URL: `https://www.iea.org/publications/freepublications/publication/KeyWorld2017.pdf` (visited on Sept. 2018).

[6] *Renewables 2018: Global Status Report.* URL: `http://www.ren21.net/gsr-2018` (visited on Sept. 2018).

[7] F. Lafond et al. "How well do experience curves predict technological progress? A method for making distributional forecasts". In: *Technological Forecasting and Social Change* 128 (2018), pp. 104–117.

[8] *Weekly PV Spot Price.* URL: `ttps://pv.energytrend.com/pricequotes.html` (visited on Sept. 2018).

[9] H. Chen et al. "The controversial fuel methanol strategy in China and its evaluation". In: *Energy Strategy Reviews* 4 (2014), pp. 28–33.

[10] G. Bozzano and F. Manenti. "Efficient methanol synthesis: perspectives, technologies and optimization strategies". In: *Progress in Energy and Combustion Science* 56 (2016), pp. 71–105.

[11] P. Tian et al. "Methanol to olefins (MTO): from fundamentals to commercialization". In: *Acs Catalysis* 5.3 (2015), pp. 1922–1938.

[12] J. R. Davis. *Corrosion of aluminum and aluminum alloys.* Asm International, 1999.

[13] P. Basarkar. "Experimental Characterization of a Novel Small Scale Natural Circulation Loop Methanol Synthesis Reactor". In: (2018).

[14] BASF. *Synthetic manufacture of methanol.* D.R. Patents 415, 686; 441, 433 and 462, 837. 1923.

[15] D. Sheldon. "Methanol Production-A Technical History". In: *Johnson Matthey Technology Review* 61.3 (2017), pp. 172–182.

[16] W. Blasiak. Polish Patent PRL34000. 1947.

[17] J.-P. Lange. "Methanol synthesis: a short review of technology improvements". In: *Catalysis Today* 64.1-2 (2001), pp. 3–8.

[18] S. Lee. *Methanol synthesis technology.* CRC Press, 1989.

[19] G. A. Olah. "Beyond oil and gas: the methanol economy". In: *Angewandte Chemie International Edition* 44.18 (2005), pp. 2636–2639.

[20] *World's largest CO_2 methanol plant.* URL: `http://carbonrecycling.is/george-olah/` (visited on Oct. 2018).

[21] H. Arakawa. "Research and development on new synthetic routes for basic chemicals by catalytic hydrogenation of CO2". In: *Studies in surface science and catalysis.* Vol. 114. Elsevier, 1998, pp. 19–30.

[22] M. Saito et al. "Development of copper/zinc oxide-based multicomponent catalysts for methanol synthesis from carbon dioxide and hydrogen". In: *Applied Catalysis A: General* 138.2 (1996), pp. 311–318.

[23] A. Zachopoulos and E. Heracleous. "Overcoming the equilibrium barriers of CO_2 hydrogenation to methanol via water sorption: A thermodynamic analysis". In: *Journal of CO_2 Utilization* 21 (2017), pp. 360–367.

[24] M. Spencer. "The role of zinc oxide in Cu/ZnO catalysts for methanol synthesis and the water–gas shift reaction". In: *Topics in Catalysis* 8.3-4 (1999), p. 259.

[25] T. Fujitani and J. Nakamura. "The effect of ZnO in methanol synthesis catalysts on Cu dispersion and the specific activity". In: *Catalysis Letters* 56.2-3 (1998), pp. 119–124.

[26] H.-J. Wernicke, L. Plass, and F. Schmidt. "Methanol generation". In: *Methanol: the basic chemical and energy feedstock of the future.* Springer, 2014, pp. 51–301.

[27] M. Spencer. "Stable and metastable metal surfaces in heterogeneous catalysis". In: *Nature* 323.6090 (1986), p. 685.

[28] J. Toyir et al. "Sustainable process for the production of methanol from CO_2 and H_2 using Cu/ZnO-based multicomponent catalyst". In: *Physics Procedia* 2.3 (2009), pp. 1075–1079.

[29] J. Wu et al. "Optimization of preparation conditions and improvement of stability of Cu/ZnO-based multicomponent catalysts for methanol synthesis from CO_2 and H_2". In: *Catalysis Today* 45.1-4 (1998), pp. 215–220.

[30] D. Rotman. "Lurgi unveils route to methanol from carbon dioxide at ACS meeting." In: *Chemical Week* 154.11 (1994), pp. 14–14.

[31] S. Park et al. "CAMERE process for methanol synthesis from CO_2 hydrogenation". In: *Studies in Surface Science and Catalysis* 153 (2004), pp. 67–72.

[32] O.-S. Joo et al. "Carbon dioxide hydrogenation to form methanol via a reverse-water-gas-shift reaction (the CAMERE process)". In: *Industrial & engineering chemistry research* 38.5 (1999), pp. 1808–1812.

[33] M. J. Bos and D. W. F. Brilman. "A novel condensation reactor for efficient CO_2 to methanol conversion for storage of renewable electric energy". In: *Chemical engineering journal* 278 (2015), pp. 527–532.

[34] L. Chen et al. “Optimization of methanol yield from a Lurgi reactor”. In: *Chemical engineering & technology* 34.5 (2011), pp. 817–822.

[35] P. Harriott. *Chemical reactor design.* CRC Press, 2002.

[36] A. G. Dixon and D. L. Cresswell. “Theoretical prediction of effective heat transfer parameters in packed beds”. In: *AIChE Journal* 25.4 (1979), pp. 663–676.

[37] C. E. Schwartz and J. Smith. “Flow distribution in packed beds”. In: *Industrial & Engineering Chemistry* 45.6 (1953), pp. 1209–1218.

[38] A. Montebelli et al. “Optimization of compact multitubular fixed-bed reactors for the methanol synthesis loaded with highly conductive structured catalysts”. In: *Chemical Engineering Journal* 255 (2014), pp. 257–265.

[39] B. Zohuri. *Heat pipe design and technology.* Springer, 2011.

[40] J. Ku. *Introduction to heat pipes.* 2015. URL: `https://ntrs.nasa.gov/search.jsp?R=20150018080` (visited on Oct. 2018).

[41] D. Reay, R. McGlen, and P. Kew. *Heat pipes: theory, design and applications.* Butterworth-Heinemann, 2013.

[42] C. Savage. *Heatpipes and vapour chambers for satellite thermal balance.* Tech. rep. Royal aircraft establishment Farnborough, 1969.

[43] D. Bugby et al. “Satellite Modular and Reconfigurable Thermal System (SMARTS)”. In: (2008).

[44] P.-F. Gou, L. E. Fennern, and C. D. Sawyer. *Nuclear reactor heat pipe.* US Patent 5,684,848. 1997.

[45] V. E. Hampel. *Underground nuclear power station using self-regulating heat-pipe controlled reactors.* US Patent 4,851,183. 1989.

[46] E. Greenspan. *Solid Core Heat-Pipe Nuclear Batterly Type Reactor.* Tech. rep. University of California, 2008.

[47] E. Azad, F. Bahar, and F. Moztarzadeh. “Solar water heater using gravity-assisted heat pipe”. In: *Heat Recovery Systems and CHP* 7.4 (1987), pp. 343–350.

[48] A. Caruso et al. “Heat pipe heat storage performance”. In: *Heat Recovery Systems and CHP* 9.5 (1989), pp. 407–410.

[49] E. Waters. *Permafrost structural support with heat pipe stabilization.* US Patent 3,788,389. 1974.

[50] M. Zhang et al. “Numerical study on cooling characteristics of two-phase closed thermosyphon embankment in permafrost regions”. In: *Cold Regions Science and Technology* 65.2 (2011), pp. 203–210.

[51] V. Ayel et al. “Theoretical study and review on the operational limitations due to vapour flow in heat pipes”. In: *Frontiers in Heat Pipes* 3.2 (2012).

[52] P. Nemec, A. Čaja, and M. Malcho. “Mathematical model for heat transfer limitations of heat pipe”. In: *Mathematical and Computer Modelling* 57.1-2 (2013), pp. 126–136.

[53] C. Busse. “Pressure drop in the vapor phase of long heat pipes”. In: *Thermionic Conversion Specialist Conference, Palo Alto, CA*. 1967.

[54] C. Tien and K. Chung. “Entrainment limits in heat pipes”. In: *Aiaa Journal* 17.6 (1979), pp. 643–646.

[55] M. R. Shirazy and L. G. Fréchette. “Capillary and wetting properties of copper metal foams in the presence of evaporation and sintered walls”. In: *International Journal of Heat and Mass Transfer* 58.1-2 (2013), pp. 282–291.

[56] K. Leong, C. Liu, and G. Lu. “Characterization of sintered copper wicks used in heat pipes”. In: *Journal of Porous Materials* 4.4 (1997), pp. 303–308.

[57] C. Ferrandi et al. “Lumped parameter model of sintered heat pipe: Transient numerical analysis and validation”. In: *Applied Thermal Engineering* 50.1 (2013), pp. 1280–1290.

[58] H. H. Uhlig et al. “Corrosion handbook”. In: (1948).

[59] L. Shreir, R. Jarman, and G. Burstein. “Corrosion, vol. 1”. In: *Butterworth-Heinemann, Ltd. Great Britain* 2 (1994), p. 35.

[60] C. Vargel. *Corrosion of aluminium*. Elsevier, 2004.

[61] Z. Szklarska-Smialowska and J. Mankowski. “The pitting of stainless steel in water-containing methanol”. In: *Corrosion Science* 22.12 (1982), pp. 1105–1112.

[62] A. F. Mills and A. Mills. *Basic heat and mass transfer*. Vol. 2. Prentice hall Upper Saddle River, 1999.

[63] V. Kadambi and R. Drake. “Free convection heat transfer from horizontal surfaces for perscribed variations in surface temperature and mass flow though the surface”. In: *Technical Report, Mech. Eng. HT-1* (1960).

[64] G. Gutierrez-Neri. “Modeling of natural circulation flow reactor for methanol synthesis from renewable sources”. In: (2018).

[65] C. K. Batchelor and G. Batchelor. *An introduction to fluid dynamics*. Cambridge university press, 1967.

[66] G. Vazquez, E. Alvarez, and J. M. Navaza. “Surface tension of alcohol water+ water from 20 to 50. degree. C”. In: *Journal of chemical and engineering data* 40.3 (1995), pp. 611–614.

[67] *Tri-Clamp Gaskets*. URL: `https://www.marcorubber.com/tri-clamp-sanitary-gasket.htm` (visited on Jan. 2019).

[68] *Rubber Chemical Resistance Chart*. URL: `http://mykin.com/rubber-chemical-resistance-chart` (visited on Jan. 2019).

[69] S. Ergun. “Fluid flow through packed columns”. In: *Chem. Eng. Prog.* 48 (1952), pp. 89–94.

[70] P. Tijm, F. Waller, and D. Brown. “Methanol technology developments for the new millennium”. In: *Applied Catalysis A: General* 221.1-2 (2001), pp. 275–282.

[71] S. Dimov et al. “Thermal conductivity of composite catalysts containing metallic copper as a reinforcing component”. In: *Theoretical Foundations of Chemical Engineering* 41.2 (2007), pp. 184–192.

[72] G. Dul’Nev and Z. Sigalova. “Effective thermal conductivity of granular materials”. In: *Journal of Engineering Physics and Thermophysics* 13.5 (1967), pp. 355–364.